Universitat Politècnica de Catalunya

BACHELOR'S THESIS

Numerical study of the Navier-Stokes equations using the Fractional Step Method. Application to the laminar flow around a square cylinder

---

Escola Superior d'Enginyeries Industrial, Aeroespacial i Audiovisual de Terrassa (ESEIAAT)

Degree: Aerospace Technologies engineering

Date of submission: 10^{th} June 2019

Author: Luque Barcons, Jordi

Director: Pérez-Segarra, Carlos-David

Abstract

The numerical resolution of the incompressible Navier-Stokes equations with the Fractional Step Method, based on the Helmholtz-Hodge theorem, is studied. Basic benchmark problems are solved previously, such as a generic transient 2D heat conduction problem, potential flow around a rotating and non-rotating cylinder and a generic convection-diffusion equation; with excellent agreement with the results obtained and the ones on the literature. The code for the incompressible Navier-Stokes equation is verified using the benchmark results of the Lid-driven cavity problem with really good agreement as well. Finally, laminar flow around a confined square cylinder is studied and compared with the results from Breuer et. al. The drag coefficient and Strouhal number are computed finding good agreement for Reynolds numbers lower than 100 but important discrepancies for higher Reynolds.

Contents

List of Figures **3**

List of Tables **8**

1 Introduction **9**
1.1 Aim of the thesis 9
1.2 Background and Justification 9
1.3 Scope 10
1.4 Requirements 11

2 Previous study **12**
2.1 Introduction 12
2.2 Navier-Stokes equations: Mathematical formulation 12
2.3 Finite Volume Method (FVM) or Finite Difference Method (FDM) 13
2.4 Iterative solvers 15
2.5 Properties of a numerical scheme 15
2.6 Conclusions 16

3 Diffusion equations - Heat transfer problem **17**
3.1 Introduction 17
3.2 Mathematical formulation 17
3.3 2D wall with 4 different materials 21
3.3.1 Discretization of the geometry and equations 22
3.4 Results of the transient 2D heat conduction problem 28
3.5 Conclusions 32

4 Potential flow **33**
4.1 Introduction 33
4.2 Mathematical formulation: Stream function 33

4.3 Incompressible potential flow around a cylinder (rotating and non-rotating) . . . 37
4.4 Non-rotating cylinder results . . . 39
4.5 Rotating cylinder results . . . 43
4.6 Mesh discretization study . . . 46
4.7 Conclusions . . . 47

5 Convection-diffusion equation 48
5.1 Introduction . . . 48
5.2 Mathematical formulation . . . 48
5.3 Unidimensional flow with an unidimensional variation of the variable solved in the same direction of the flow . . . 59
5.4 Unidimensional flow with an unidimensional variation of the variable solved in the perpendicular direction of the flow . . . 63
5.5 Diagonal Flow . . . 65
5.6 Solenoidal Flow . . . 69
5.7 Conclusions . . . 72

6 Incompressible Navier-Stokes equations: Fractional step method approach 74
6.1 Introduction . . . 74
6.2 Mathematical background: The Helmholtz-Hodge theorem . . . 74
6.3 Mathematical formulation . . . 77
6.4 The checkerboard problem . . . 79
6.5 Staggered meshes approach . . . 79
6.6 Equations discretization . . . 81
6.7 Boundary conditions . . . 83
6.8 Lid-driven cavity problem . . . 86
6.9 Flow between flat plates: Poiseuille Flow . . . 95
6.10 Laminar flow around a square cylinder . . . 99
6.11 Conclusions . . . 116

7 Budget of the study 117

8 Environmental impact 119

9 Task planning 120

10 Conclusions and future work 122

11 Bibliography 124

List of Figures

2.1 Nomenclature used at each control volume 14

3.1 Integral calculated explicitly 19
3.2 Integral calculated implicitly 19
3.3 Integral calculated using Crank-Nicolson 20
3.4 2D wall with 4 different materials [1] 21
3.5 Boundary conditions of the top nodes of the 2D wall 22
3.6 Boundary conditions of the left nodes of the 2D wall 23
3.7 Boundary conditions of the top left node of the 2D wall . . . 24
3.8 Boundary conditions of the central nodes of the 2D wall . . . 25
3.9 Proposed algorithm for the 2D heat conduction problem . . . 27
3.10 Temperature at $t = 300s$ (left) and at $t = 1100s$ (right) . . . 28
3.11 Temperature at $t = 3000s$ (left) and at $t = 3600s$ (right) . . . 28
3.12 Temperature at $t = 5000s$ (left) and at $t = 10000s$ (right) . . 29
3.13 Evolution of temperature of points [0,74, 0,72] and [0,65, 0,56] with respect to time 29
3.14 Variation of temperature at [0,74, 0,72] at t=10000s and computation time as a function of the number of nodes 30
3.15 Temperature at [0,65, 0,56] at t=10000s and computation time as a function of the number of time-steps 31
3.16 Temperature at [0,65, 0,56] at t=10000s as a function of the convergence criterion 31

4.1 Positive velocities and circulation direction 34
4.2 Velocity evaluation at interface between solid and fluid CVs . 36
4.3 Schematization of the problem 37
4.4 Algorithm for potential flow 39
4.5 Mesh around the cylinder 40
4.6 Stream Function values and Streamlines 41

4.7 V_x (right) and V_y (left) in m/s 42
4.8 Velocity modulus around the cylinder and comparison with analytical solution 42
4.9 Cp around the cylinder and comparison with analytical solution 43
4.10 |V| and Cp for a rotating cylinder generating a circulation of $\Gamma = 40m^2/s$ 44
4.11 Cp for a rotating cylinder generating a circulation of $\Gamma = 40m^2/s$ and comparison with analytical solution 45
4.12 |V| and Cp for a cylinder generating a circulation of $\Gamma = 170m^2/s$ 46
4.13 Absolute error of Cp for a rotating cylinder generating a circulation of $\Gamma = 40m^2/s$ with respect to cell size around the cylinder 47

5.1 Upwind difference scheme 52
5.2 Central difference scheme 53
5.3 D, C and U nodes to normalise variables 54
5.4 Second Order Upwind linear extrapolation Scheme 55
5.5 QUICK Scheme 55
5.6 Algorithm for the convection-diffusion problem 58
5.7 Unidimensional flow with an unidimensional variation of the variable solved in the same direction of the flow 59
5.8 Unidimensional flow with an unidimensional variation of the variable solved in the same direction of the flow with 5x5 mesh and $Pe = 4$ 60
5.9 Unidimensional flow with an unidimensional variation of the variable solved in the same direction of the flow with 5x5 mesh and $Pe = 10, 25$ 60
5.10 Unidimensional flow with an unidimensional variation of the variable solved in the same direction of the flow with 5x5 mesh and $Pe = 20$ 61
5.11 Unidimensional flow with an unidimensional variation of the variable solved in the same direction of the flow with 100x100 mesh and different Péclet numbers 62
5.12 $log_{10}(\Delta_x)$ vs $log_{10}(Absolute\ error)$ for different convective schemes 63
5.13 Unidimensional flow with an unidimensional variation of the variable solved in the perpendicular direction of the flow . . . 64

5.14 Unidimensional flow with an unidimensional variation of the variable solved in the perpendicular direction of the flow for ϕ_L=10, 70 & 200 and 100x100 mesh (UDS) 65
5.15 Diagonal flow 65
5.16 Diagonal flow for Pe=10 (top left), Pe=100 (top right), Pe=10000 (bottom left), Pe=1e30 (bottom right) 66
5.17 Diagonal flow results for different Péclet numbers with UDS and 100x100 mesh 67
5.18 Diagonal flow results for a 100x100 mesh and Pe=1e30 using UDS, SUDS and QUICK 68
5.19 Diagonal flow results for Pe=1e30 (UDS) for different mesh sizes 69
5.20 Solenoidal flow (Smith-Hutton problem) 70
5.21 Diagonal flow (Smith-Hutton results for 200x200 mesh and UDS) 71
5.22 Solenoidal flow (Smith-Hutton results for $\rho/\Gamma = 10$) 71
5.23 Solenoidal flow (Smith-Hutton results forfor $\rho/\Gamma = 10^3$) . . . 72
5.24 Solenoidal flow (Smith-Hutton results for for $\rho/\Gamma = 10^6$) . . . 72

6.1 Helmholtz-Hodge theorem 76
6.2 Checkerboard problem 79
6.3 Staggered meshes approach to solve the checkerboard problem 80
6.4 Mass flow for the mesh staggered in x direction 80
6.5 Mass flow for the mesh staggered in y direction 81
6.6 Velocity calculation (u (left) and v (right)) from pressure field [2] 83
6.7 Pressure boundary condition at the wall 84
6.8 Prescribed velocity boundary condition 84
6.9 Algorithm for the incompressible Navier-Stokes equations using the Fractional Step method 85
6.10 Lid-driven cavity problem 86
6.11 Lid-driven cavity horizontal velocity in the vertical centerline of the cavity for $Re = 100$ (left) and $Re = 400$ (right), compared with benchmark solutions. 87
6.12 Lid-driven cavity horizontal velocity in the vertical centerline of the cavity for $Re = 1000$ (left) and $Re = 3200$ (right), compared with benchmark solutions 88
6.13 Lid-driven cavity horizontal velocity in the vertical centerline of the cavity for $Re = 5000$, compared with benchmark solution 88

6.14 Lid-driven cavity vertical velocity in the horizontal centerline of the cavity for $Re = 100$ (left) and $Re = 400$ (right), compared with benchmark solutions. 89
6.15 Lid-driven cavity vertical velocity in the horizontal centerline of the cavity for $Re = 1000$ (left) and $Re = 3200$ (right), compared with benchmark solutions 90
6.16 Lid-driven cavity vertical velocity in the horizontal centerline of the cavity for $Re = 5000$ compared with benchmark solution 90
6.17 Absolute error and computation time as a function of the Reynolds number for the UDS and SMART convective schemes 91
6.18 Lid-driven cavity velocity modulus and isolines of the velocity for $Re = 100$ 92
6.19 Lid-driven cavity velocity modulus and isolines of the velocity for $Re = 400$ 92
6.20 Lid-driven cavity velocity modulus and isolines of the velocity for $Re = 1000$ 93
6.21 Lid-driven cavity velocity modulus and isolines of the velocity for $Re = 3200$ 93
6.22 Lid-driven cavity velocity modulus and isolines of the velocity for $Re = 5000$ 94
6.23 Pressure distribution at $Re = 3200$ 94
6.24 Small vortex generated on the top left corner (left) and pressure build-up on the top right corner (right) 95
6.25 Poiseuille flow between flat plates 96
6.26 Velocity across the channel 97
6.27 Velocity profile at different sections of the channel 97
6.28 Pressure loss across the channel 98
6.29 Pressure distribution across the channel 98
6.30 Pressure distribution at the inlet of the channel 99
6.31 Flow around a square cylinder: geometry of the problem . . . 99
6.32 Mesh used for the square cylinder problem 100
6.33 Close-up of the mesh around the square cylinder 100
6.34 Streamlines around the square cylinder for $Re = 1,\ 30,$ and 45 102
6.35 Streamlines around the square cylinder for $Re = 100,$ and 200 103
6.36 Close-up of the streamlines for $Re = 30$ (left) and $Re = 45$ (right) 103
6.37 Close-up of the streamlines for $Re = 100$ (left) and $Re = 200$ (right) 104
6.38 Recirculation length at $Re = 30$ 104

6.39 Recirculation length as a function of the Reynolds number and comparison with results from [3] 105
6.40 Streamwise (U) and cross-stream (V) velocities along the centerline (y=0) for $Re = 1$ 105
6.41 Streamwise (U) and cross-stream (V) velocities at different positions (centre of the cylinder ($x = 0$), near-wake ($x = 4$) and far-wake ($x = 8$) for $Re = 1$ 106
6.42 Streamwise (U) and cross-stream (V) velocities along the centerline (y=0) for $Re = 30$ 106
6.43 Streamwise (U) and cross-stream (V) velocities at different positions (centre of the cylinder ($x = 0$), near-wake ($x = 4$) and far-wake ($x = 8$) for $Re = 30$ 107
6.44 Streamwise (U) velocity along the centerline ($y = 0$) for $Re = 100$ and comparison with results from [3] 108
6.45 Cross-stream (V) velocity at along the centerline ($y = 0$) for $Re = 100$ and comparison with results from [3] 108
6.46 Streamwise (U) velocity at different positions (centre of the cylinder ($x = 0$), near-wake ($x = 4$) and far-wake ($x = 8$) for $Re = 100$ and comparison with results from [3] 109
6.47 Cross-streamwise (V) velocity at different positions (centre of the cylinder ($x = 0$), near-wake ($x = 4$) and far-wake ($x = 8$) for $Re = 100$ and comparison with results from [3] 109
6.48 Velocity modulus at $Re = 1$ 110
6.49 Velocity modulus at $Re = 30$, $Re = 100$ and $Re = 200$ 111
6.50 Cd as a function of the Reynolds number in steady conditions and comparison with results from [3] 112
6.51 Variation of Cd with time for $Re = 100$ (left) and $Re = 150$ (right) 113
6.52 Variation of Cd with time for $Re = 200$ (left) and $Re = 250$ (right) 113
6.53 Time-averaged Cd as a function of the Reynolds number . . . 114
6.54 Variation of the Strouhal number with the Reynolds number 115

9.1 Gantt chart 121

List of Tables

3.1 Geometrical properties of the 2D wall (coordinates) 21
3.2 Physical properties of each material of the 2D wall 21
3.3 Boundary conditions of the 2D wall 22

5.1 Convective term, diffusion term and source term of the Navier-Stokes equations. Extracted from [4] 49
5.2 Benchmark results for the Smith-Hutton problem. Extracted from [4] 70

6.1 Lid-driven cavity benchmark results. u in the vertical center line. Extracted from [2] 87
6.2 Lid-driven cavity benchmark results. v in the horizontal center line. Extracted from [2] 89
6.3 Geometry details of the problem: flow around a square cylinder 100
6.4 Boundary conditions 101

7.1 Software budget 118
7.2 Hardware budget 118
7.3 Salary 118
7.4 Total budget 118

Chapter 1

Introduction

1.1 Aim of the thesis

The main objective of this thesis is the elaboration, validation and verification of self-developed C++ codes in order to solve the incompressible Navier-Stokes equations, being the final objective the study of the vortex shedding phenomenon behind a square cylinder.

1.2 Background and Justification

The importance of numerical methods in engineering is widely known in the industry, as the vast majority of problems can be modelled using differential equations. As those equations can hardly ever be solved analytically, the use of high order numerical schemes becomes vital to get precise results.

Computational Fluid Dynamics (CFD) is an example of numerical methods used in engineering. CFD is the branch of fluid mechanics that uses numerical techniques to study the properties and characteristics of fluid flows by means of a computer-based simulation. CFD is applied in many different fields: aerodynamics, weather simulation, study of combustion phenomena, biological fluid flows... [5]. The availability of high performance computing and algorithms in the recent years has increased the usage of CFD in the industry, leading to the creation of many different software with user-friendly interfaces. The advantages of Computational Fluid Dynamics over experiment-based techniques are clear [6]:

- Possibility to test many different configurations and reach an optimum

one through optimization algorithms without having to create different prototypes, which would lead to a high increase in the expenses of the study

- Ability to study systems in hazardous conditions in which real life testing would not be possible or very expensive
- Ability to change the flow parameters without having to make another experiment

Nevertheless, the main drawbacks of numerical simulations are also really important and should be taken into account. As the equations are not solved analytically, different errors are being accumulated in the solution process [7]:

- Discretization errors: local truncation errors, global truncation error, aliasing error...
- Residual of the solver and round-off errors.

Moreover, in order to get highly accurate results, the used mesh needs to be extremely fine, specially with turbulent flows. With available codes in the market, computation cost grows with Re^3 [8], which increases dramatically the computation time needed, specially for higher Reynolds simulations of an aircraft, for example. To solve this problem, turbulence models are used, decreasing computation time but also precision in the results.

1.3 Scope

In order to reach the final goal of the thesis, different benchmark problems are previously solved to set up the basis. First of all, a 2D heat conduction problem is solved in order to study a typical diffusion equation.This is followed by the study of potential flow around a rotating and non-rotating cylinder using the stream function approach. The code is verified using results from literature.

Then, a general convection-diffusion equation is solved as the previous step before solving the Navier-Stokes equations. Different numerical convective schemes are studied, focusing in order of accuracy of each of them and stability. The code is verified with different benchmark problems such

as diagonal flow and Smith-Hutton problem.

Finally, the Navier-Stokes equations are solved using the Fractional Step Method and the code is verified with the well-known results of the Lid-Driven cavity problem. The same code is finally used to study the laminar flow inside a channel (Poiseuille flow) and the vortex shedding phenomenon behind a square cylinder.

1.4 Requirements

The necessary requirements of this thesis are the presentation of the self-developed codes in C++ to solve all the benchmark problems mentioned previously. All the figures shown made during the post-process of each study are done using "Paraview" software, and the plots are done with "Matlab" software, which are also mandatory in order to prove the proper functioning of the developed codes.

Chapter 2

Previous study

2.1 Introduction

In this chapter, the basis of computational fluid dynamics are set. The mathematical formulation of the Navier-Stokes equations is presented and the differences between the finite volume method and finite difference method are explained. Finally, different iterative solvers are briefly described in conjunction with the most important properties of a numerical scheme.

2.2 Navier-Stokes equations: Mathematical formulation

The Navier-Stokes equations are a set of coupled non-linear partial differential equations that describe the motion of a fluid. In general, it does not exist an analytical solution for these equations, except for some concrete flow and boundary conditions. In fact, they are an extension of the Euler equations but considering the viscous effects [9].

The Navier-Stokes equations consist of one time-dependent conservation of mass equation, three time-dependent conservation of momentum equations (one for each velocity component ($u,\ v,\ ,w$), and another time-dependent conservation of energy equation. There are 4 independent variables, the three spatial coordinates ($x,\ y,$ and z) (in cartesian coordinates), plus the time (t). However, there are 6 dependent variables (the three velocity components, pressure, density and temperature), which means that another equation such as an equation of state needs to be used in order to

solve the system [10].

The Navier-Stokes equations are now presented:

$$\frac{\partial \rho}{\partial t} + \frac{\partial(\rho u)}{\partial x} + \frac{\partial(\rho v)}{\partial y} + \frac{\partial(\rho w)}{\partial z} = 0 \tag{2.2.1}$$

$$\frac{\partial(\rho u)}{\partial t} + \frac{\partial(\rho uu)}{\partial x} + \frac{\partial(\rho vu)}{\partial y} + \frac{\partial(\rho wu)}{\partial z} = -\frac{\partial P}{\partial x} + \frac{\partial \tau_{xx}}{\partial x} + \frac{\partial \tau_{yx}}{\partial y} + \frac{\partial \tau_{zx}}{\partial z} + \rho g_x + f_x^e \tag{2.2.2}$$

$$\frac{\partial(\rho v)}{\partial t} + \frac{\partial(\rho uv)}{\partial x} + \frac{\partial(\rho vv)}{\partial y} + \frac{\partial(\rho wv)}{\partial z} = -\frac{\partial P}{\partial y} + \frac{\partial \tau_{xy}}{\partial x} + \frac{\partial \tau_{yy}}{\partial y} + \frac{\partial \tau_{zy}}{\partial z} + \rho g_y + f_y^e \tag{2.2.3}$$

$$\frac{\partial(\rho w)}{\partial t} + \frac{\partial(\rho uw)}{\partial x} + \frac{\partial(\rho vw)}{\partial y} + \frac{\partial(\rho ww)}{\partial z} = -\frac{\partial P}{\partial z} + \frac{\partial \tau_{xz}}{\partial x} + \frac{\partial \tau_{yz}}{\partial y} + \frac{\partial \tau_{zz}}{\partial z} + \rho g_z + f_z^e \tag{2.2.4}$$

$$\begin{aligned} \frac{\partial(\rho e)}{\partial t} + \frac{\partial(\rho ue)}{\partial x} + \frac{\partial(\rho ve)}{\partial y} + \frac{\partial(\rho we)}{\partial z} &= -\left(\frac{\partial \dot{q}_x}{\partial x} + \frac{\partial \dot{q}_y}{\partial y} + \frac{\partial \dot{q}_z}{\partial z}\right) \\ -\left(\frac{\partial(Pu)}{\partial x} + \frac{\partial(Pv)}{\partial y} + \frac{\partial(Pw)}{\partial z}\right) + \frac{\partial}{\partial x}(u\tau_{xx} + v\tau_{xy} + w\tau_{xz}) + \\ \frac{\partial}{\partial y}(u\tau_{yx} + v\tau_{yy} + w\tau_{yz}) + \frac{\partial}{\partial z}(u\tau_{zx} + v\tau_{zy} + w\tau_{zz}) + \\ \rho(g_x u + g_x v + g_z w) \end{aligned} \tag{2.2.5}$$

Where, equation (2.2.1) is the mass conservation equation, equations (2.2.2, 2.2.3 and 2.2.4) are the momentum conservation equations in x, y and z, where, (f_x^e, f_y^e and f_z^e) are external forces in each of the three directions; and equation (2.2.5) is the energy conservation equation.

2.3 Finite Volume Method (FVM) or Finite Difference Method (FDM)

There are two main methods used to discretize the equations: The finite volume method and the finite difference method. The finite difference method is based on the approximation of the partial derivatives of each equation

by a Taylor expansion series with the desired order of accuracy. As it is obvious, the higher the order of accuracy, the better the results. However, complexity increases and computation time as well.

On the other hand, the Finite Volume method is also based on calculating the values at a concrete place in a discretized geometry (mesh). However, instead of using the differential form of the equations, the integral form of the governing equations is used, and all the volume integrals at each control volume are converted into surface integrals using the divergence theorem. As a result, theses terms are computed as fluxes of a certain value through the cell face. As the flux entering a surface is the same as the flux leaving the surface of the adjacent control volume, if conservation is ensured at each control volume it is also ensured in all the domain. This, and the fact that it can be easily implemented with non-structured meshes, makes it really popular for CFD.

In this thesis the Finite Volume Method is used to solve all the problems, and the nomenclature used to discretize the geometry is the following:

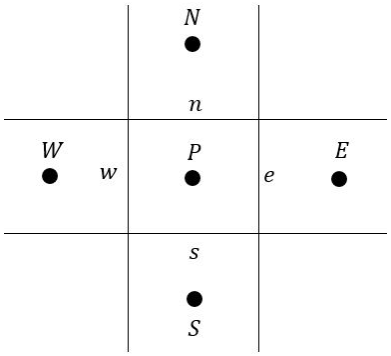

Figure 2.1: Nomenclature used at each control volume

Where the letters in capitals N, E, S and W refer to the northern, eastern, southern and western nodes respectively, while the lower case letters n, e, s and w refer to the northern, eastern, southern and western cell faces respectively. The same letters are used in the equations to refer to the same properties of the control volume.

2.4 Iterative solvers

As the solution of the desired property at each control volume depends on the values at the adjacent ones (equations are coupled), an iterative method to solve the equations is necessary. Iterative methods such as the Gauss-Seidel Method [11] or the Jacobi method make use of an initial approximation value and start iterating, comparing the result of one iteration with their initial guess. After each iteration, the calculated value becomes the initial guess and this is done successively until the difference between the calculated value and the predicted one is smaller than a certain convergence criterion set by the user. These iterative methods might not converge for non-diagonally dominant matrices.

Another popular algorithm is the TDMA (Tridiagonal matrix) [12]. However, as this solver only works for tridiagonal matrices, a more advanced technique such as the Line-by-line can be used, which consists in solving each line first, and them each column with the TDMA algorithm and then compare the results obtained. If the values are not the same, an iterative process starts until a certain convergence criterion is reached.

2.5 Properties of a numerical scheme

In order to evaluate if a numerical scheme is good enough or not, it must verify some crucial properties [13]:

- **Consistency:** A numerical scheme is consistent if by reducing the size of the mesh and the time-step, the truncation error of the approximation vanishes, which means that the solution of the approximation tends to the exact solution.
- **Stability:** A numerical scheme is considered stable if the errors decay as the simulation proceeds, which means that the errors (round-off, truncation...) are not magnified during the simulation.
- **Conservation:** Conservation of properties should be respected at each discrete level.
- **Boundness:** Properties should remain within certain values without experiencing sudden overshoot or undershoots. For example, properties such as density or concentrations should remain positive.

- **Convergence:** The numerical solution should get closer to the exact solution as the mesh is refined.

2.6 Conclusions

With everything mentioned above, the basis of computational fluid dynamics are set. The difficulty of the Navier-Stokes equations is clear, specially due to its non-linearity caused by the convective term (which is treated in detail in future chapters). The differences between the finite volume method and the finite difference method are also clear, and it has been seen that the fact that the finite volume method ensures conservation in the whole domain, makes it really suitable for CFD. Finally, the main properties of a numerical scheme, in which attention should be paid in the following analysis, have been described.

Chapter 3

Diffusion equations - Heat transfer problem

3.1 Introduction

The objective of this chapter is to study a generic diffusion problem, in particular, a 2D heat transfer problem. The mathematical formulation and discretization of equation is presented in the next section and a brief study of the spatial and temporary discreitzation is done.

3.2 Mathematical formulation

In order to develop the equations that model any heat transfer problem, the first principle of thermodynamics is applied:

$$\frac{\partial}{\partial t} \oint_V \rho u \, dV = - \oint_S \dot{\mathbf{q}} \cdot \mathbf{n} \, dS \tag{3.2.1}$$

Where it has been considered that there is no work applied to the system and the variation of kinetic and potential energy is zero. (Note that in this notation u stands for internal energy rather than velocity in x direction).

An average internal energy per unit of mass and volume can be defined as:

$$\bar{u} = \frac{1}{Vp} \oint_V u \, dV \tag{3.2.2}$$

Assuming constant physical properties, density is considered a constant and comes out of the integral (3.2.1). Combining (3.2.1) with (3.2.2) it can be easily proved that:

$$\rho V p \frac{\partial \bar{u}}{\partial t} = \sum \dot{Q} \tag{3.2.3}$$

In equation (3.2.3) the integral of heat fluxes has been replaced by a summation of the net heat fluxes entering the control volume.

Integrating both sides of the previous equation:

$$\int_{t^n}^{t^{n+1}} \rho V p \frac{\partial \bar{u}}{\partial t} dt = \int_{t^n}^{t^{n+1}} \sum \dot{Q} dt \tag{3.2.4}$$

Considering that the internal energy is a state function and thus, it only depends on its initial and final values, and, assuming a second order approach for the integral on the left-hand side, the previous equation can be rewritten as:

$$\rho V_p ({u_p}^{n+1} - {u_p}^n) = \int_{t^n}^{t^{n+1}} \sum \dot{Q} dt \tag{3.2.5}$$

The integral of the right-hand side of (3.2.5) can be approximated using an explicit, implicit or crank-Nicolson approach:

- **Explicit form**:

  The finite differences are taken at the beginning of the time-step, which means that the integral is calculated using known values of the previous iteration. As a consequence, there is no need to solve a system of equations at each time step. It is less demanding in terms of computation time, but the main drawback is that it does not always converge. It is a first order approximation:

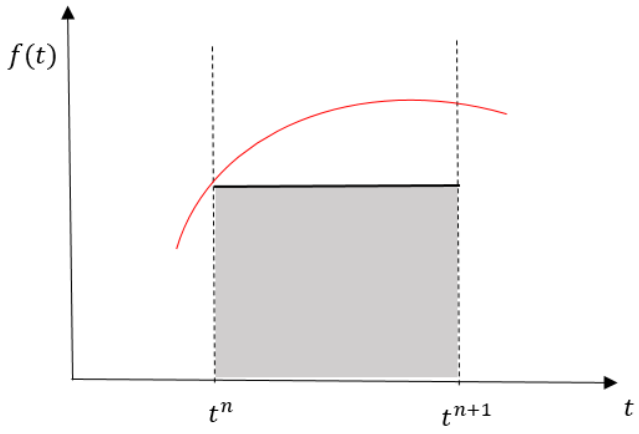

Figure 3.1: Integral calculated explicitly

- **Implicit form**:

  The finite differences are taken at the end of the time-step, which means that the integral needs to be calculated by solving a system of equations by iteration. As a consequence, the computation time increases. However, this method is unconditionally stable but it is also a first order approximation:

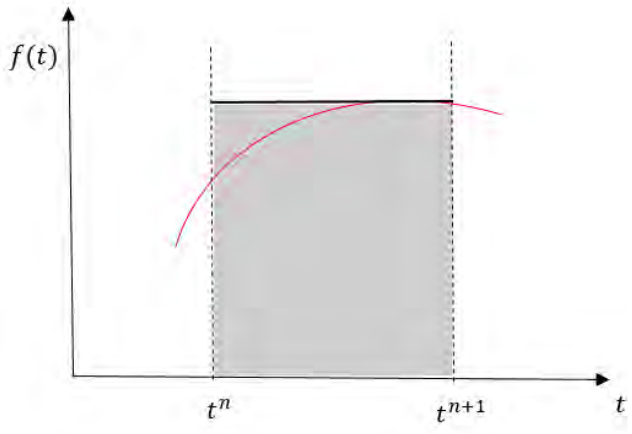

Figure 3.2: Integral calculated implicitly

- **Crank-Nicolson form**:

  This is a second order approximation for the integral and it is also unconditionally stable. However it also requires solving a system of equation by iteration, as it uses the values at the previous and new time steps.

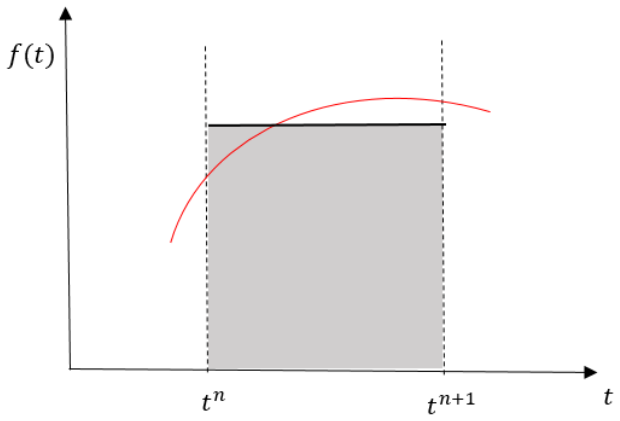

Figure 3.3: Integral calculated using Crank-Nicolson

And finally, a general form to express the integral can be written as:

$$\int_{t^n}^{t^{n+1}} \sum \dot{Q} dt \approx \left[\beta \sum_{i=1}^{i} \dot{Q}_{pi}^{n+1} + (1-\beta) \sum_{i=1}^{i} \dot{Q}_{pi}^{n} \right] \Delta t \tag{3.2.6}$$

If $\beta = 0$ the integral is calculated explicitly, if $\beta = 1$, it is calculated implicitly and if $\beta = 1/2$, the integral is calculated by Crank-Nicolson.

Applying this integral approximation to equation (3.2.5), the overall equation becomes:

$$\rho V_p ({u_p}^{n+1} - {u_p}^{n}) = \left[\beta \sum_{i=1}^{i} \dot{Q}_{pi}^{n+1} + (1-\beta) \sum_{i=1}^{i} \dot{Q}_{pi}^{n} \right] \Delta t \tag{3.2.7}$$

3.3 2D wall with 4 different materials

The benchmark problem to study consists of a 2D wall made out of 4 different materials, as it is shown in the figure below:

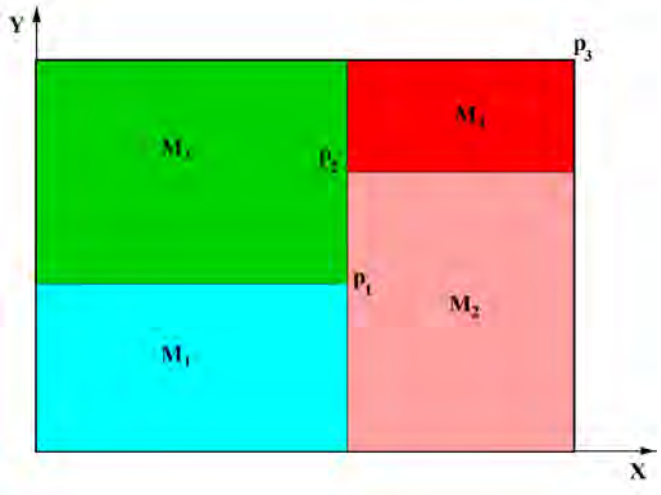

Figure 3.4: 2D wall with 4 different materials [1]

The coordinates of point p_1, p_2 and p_3 and the physical properties of each of the 4 materials are described below:

Point	$\boldsymbol{X[m]}$	$\boldsymbol{Y[m]}$
p_1	0,5	0,4
p_2	0,5	0,7
p_3	1,1	0,8

Table 3.1: Geometrical properties of the 2D wall (coordinates)

Material	$\boldsymbol{\rho\ [kg/m^3]}$	$\boldsymbol{C_p\ [J/kgK]}$	$\boldsymbol{K\ [W/mK]}$
M1	1500	750	170
M2	1600	770	140
M3	1900	810	200
M4	2500	930	140

Table 3.2: Physical properties of each material of the 2D wall

The physical properties of Table 3.3 are considered constant with temperature variation.

The boundary conditions of the problem are described in the table below:

Wall	Boundary conditions
Bottom	Isotherm at $T = 23°C$
Top	$\dot{Q}_flow = 60W/m$
Left	In contact with a fluid at $T_g = 33°C$ and $\alpha = 9W/mK$
Right	Uniform temperature $T = 8 + 0,005t°C$ (t=time in seconds)

Table 3.3: Boundary conditions of the 2D wall

The initial temperature of the wall is $8°C$

3.3.1 Discretization of the geometry and equations

In order to solve the problem, a central node discretization is used. This is an adequate discretization because if an harmonic mean is applied to calculate the coefficients of thermal conductivity at the faces, there is no need to differentiate the central nodes of the wall from the ones of the boundaries.

As nodes from the boundaries have also different boundary conditions, their discretization equations are also different and need to be considered separately:

- **Top row nodes**

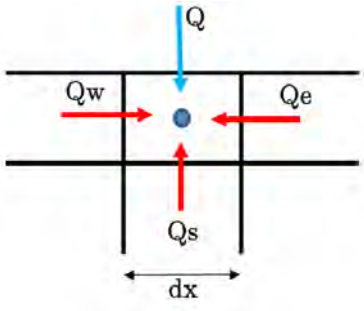

Figure 3.5: Boundary conditions of the top nodes of the 2D wall

$$\frac{\rho_P V_p C_p}{\Delta t}(T_P^{n+1} - T_P^n) = \left(-\lambda_w \frac{T_P - T_W}{d_{PW}} S_w - \lambda_s \frac{T_P - T_S}{d_{PS}} S_s + \lambda_e \frac{T_E - T_P}{d_{PE}} S_e + \dot{Q} \cdot dx\right)^{n+1} \tag{3.3.1}$$

Rearranging terms the overall equation can be written as:

$$a_P T_p^{n+1} = (a_E T_E + a_W T_W + a_S T_S + a_N T_N + bp)^{n+1} \tag{3.3.2}$$

Where:

$$a_E = \frac{\lambda_e S_e}{d_{PE}} \qquad a_S = \frac{\lambda_s S_s}{d_{PS}} \qquad a_N = 0 \qquad a_W = \frac{\lambda_w S_w}{d_{PW}}$$

$$bp = \frac{\rho_P V_p C_P T_p^n}{\Delta t} + \dot{Q} dx \qquad a_P = \frac{\rho_P V_p C_p}{\Delta t} + a_E + a_W + a_N + a_s$$

- **Left column nodes**

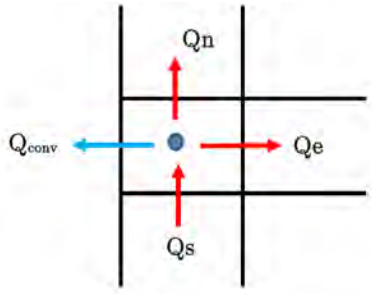

Figure 3.6: Boundary conditions of the left nodes of the 2D wall

$$\frac{\rho_P V_p C_p}{\Delta t}(T_P^{n+1} - T_P^n) = \left(-\lambda_s \frac{T_P - T_S}{d_{PS}} S_s + \lambda_e \frac{T_E - T_P}{d_{PE}} S_e + \lambda_n \frac{T_N - T_P}{d_{PN}} S_n - \alpha_g (T_P - T_g) dy\right)^{n+1} \tag{3.3.3}$$

Rearranging terms the overall equation can be written as:

$$a_P T_p^{n+1} = (a_E T_E + a_W T_W + a_S T_S + a_N T_N + bp)^{n+1} \tag{3.3.4}$$

Where:

$$a_E = \frac{\lambda_e S_e}{d_{PE}} \qquad a_S = \frac{\lambda_s S_s}{d_{PS}} \qquad a_W = 0 \qquad a_N = \frac{\lambda_n S_n}{d_{PN}}$$

$$bp = \frac{\rho_P V_p C_P T_p^n}{\Delta t} + \alpha_g T_g dy \qquad a_P = \frac{\rho_P V_p C_p}{\Delta t} + a_E + a_W + a_N + a_s + \alpha_g dy$$

- **Top Left node**

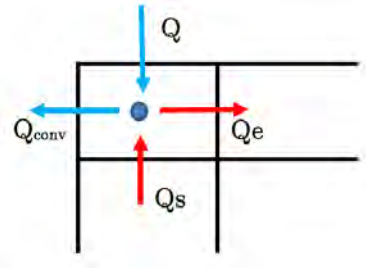

Figure 3.7: Boundary conditions of the top left node of the 2D wall

$$\frac{\rho_P V_p C_p}{\Delta t}(T_P^{n+1} - T_P^n) = \left(-\lambda_s \frac{T_P - T_S}{d_{PS}} S_s + \lambda_e \frac{T_E - T_P}{d_{PE}} S_e - \alpha_g (T_P - T_g) dy + \dot{Q} dx\right)^{n+1} \tag{3.3.5}$$

Rearranging terms the overall equation can be written as:

$$a_P T_p^{n+1} = (a_E T_E + a_W T_W + a_S T_S + a_N T_N + bp)^{n+1} \tag{3.3.6}$$

Where:

$$a_E = \frac{\lambda_e S_e}{d_{PE}} \qquad a_S = \frac{\lambda_s S_s}{d_{PS}} \qquad a_N = 0 \qquad a_W = 0$$

$$bp = \frac{\rho_P V_p C_P T_p^n}{\Delta t} + \alpha_g T_g dy + \dot{Q} dx$$

$$a_P = \frac{\rho_P V_p C_p}{\Delta t} + a_E + a_W + a_N + a_s + \alpha_g dy$$

- **Central nodes**

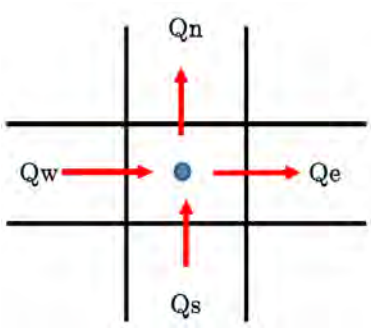

Figure 3.8: Boundary conditions of the central nodes of the 2D wall

$$\frac{\rho_P V_p C_p}{\Delta t}(T_P^{n+1} - T_P^n) = \left(-\lambda_s \frac{T_P - T_S}{d_{PS}} S_s + \lambda_e \frac{T_E - T_P}{d_{PE}} S_e + \lambda_n \frac{T_N - T_P}{d_{PN}} S_n - \lambda_w \frac{T_P - T_W}{d_{PW}} S_w\right)^{n+1} \tag{3.3.7}$$

Rearranging terms the overall equation can be written as:

$$a_P T_p^{n+1} = (a_E T_E + a_W T_W + a_S T_S + a_N T_N + bp)^{n+1} \tag{3.3.8}$$

Where:

$$a_E = \frac{\lambda_e S_e}{d_{PE}} \qquad a_S = \frac{\lambda_s S_s}{d_{PS}} \qquad a_N = \frac{\lambda_n S_n}{d_{PN}} \qquad a_W = \frac{\lambda_w S_w}{d_{PW}}$$

$$b_p = \frac{\rho_p V_P C_P T_P^n}{\Delta t} \qquad a_P = \frac{\rho_P V_P C_P}{\Delta t} + a_E + a_W + a_N + a_S$$

- **Bottom row nodes** As the temperature is prescribed, the temperature of the nodes of the bottom row can be directly imposed ($T = 23^\circ$)
- **Right column nodes** As it happens with the nodes of the bottom row, the temperature can be directly imposed ($T = 8 + 0,005t^\circ C$)

Finally and, before presenting the final algorithm, it is important to mention that, in order to calculate the thermal conductivity coefficients at the volume faces, the harmonic mean is applied. With this approach, if there are two adjacent nodes with the same thermal conductivity coefficient, the harmonic mean gives the same value at the face. However, if the two nodes have different thermal conductivity coefficients, the coefficient at the face is averaged depending on the size of each cell:

$$\lambda_e = \frac{d_{PE}}{\frac{d_{Pe}}{\lambda_P} + \frac{d_{eE}}{\lambda_E}} \tag{3.3.9}$$

$$\lambda_n = \frac{d_{PN}}{\frac{d_{Pn}}{\lambda_P} + \frac{d_{nN}}{\lambda_N}} \tag{3.3.10}$$

$$\lambda_s = \frac{d_{PS}}{\frac{d_{Ps}}{\lambda_P} + \frac{d_{sS}}{\lambda_S}} \tag{3.3.11}$$

$$\lambda_w = \frac{d_{PW}}{\frac{d_{Pw}}{\lambda_P} + \frac{d_{wW}}{\lambda_W}} \tag{3.3.12}$$

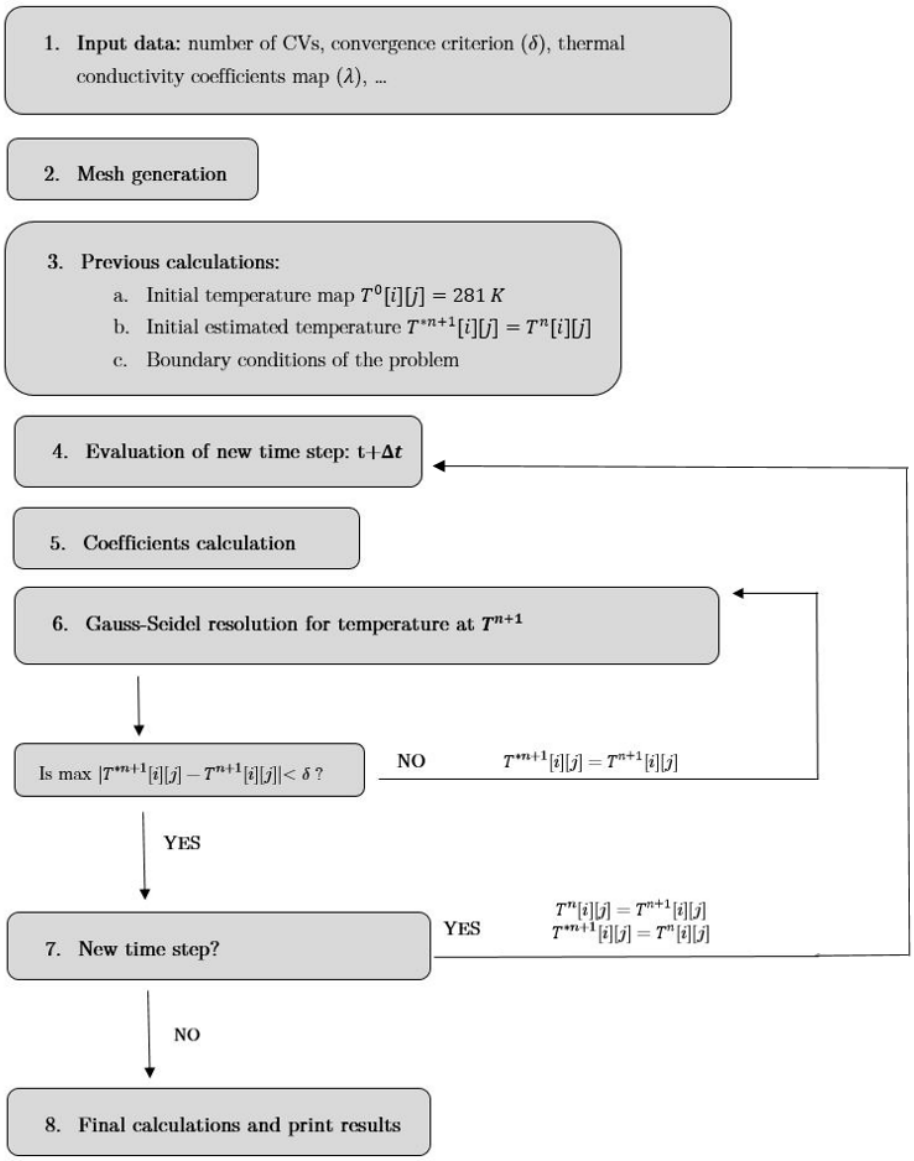

Figure 3.9: Proposed algorithm for the 2D heat conduction problem

3.4 Results of the transient 2D heat conduction problem

First of all and, as it is a transient heat conduction problem, different surface colour maps of the temperature are presented at different times of the simulation.

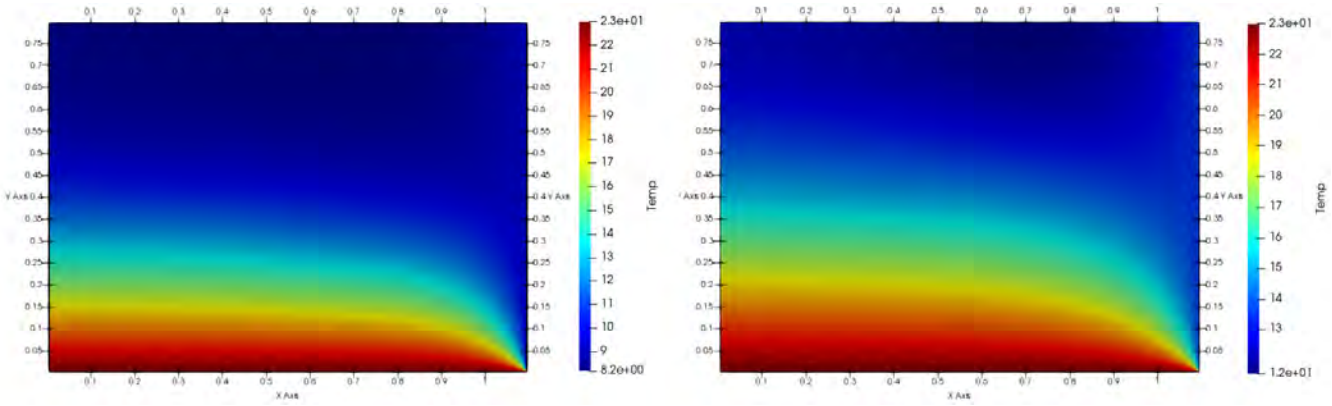

Figure 3.10: Temperature at $t = 300s$ (left) and at $t = 1100s$ (right)

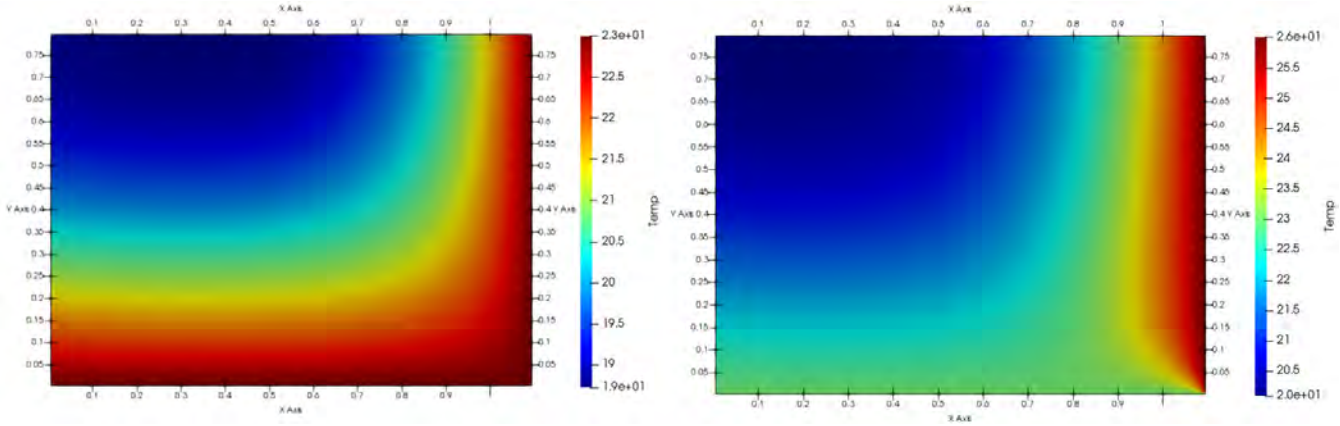

Figure 3.11: Temperature at $t = 3000s$ (left) and at $t = 3600s$ (right)

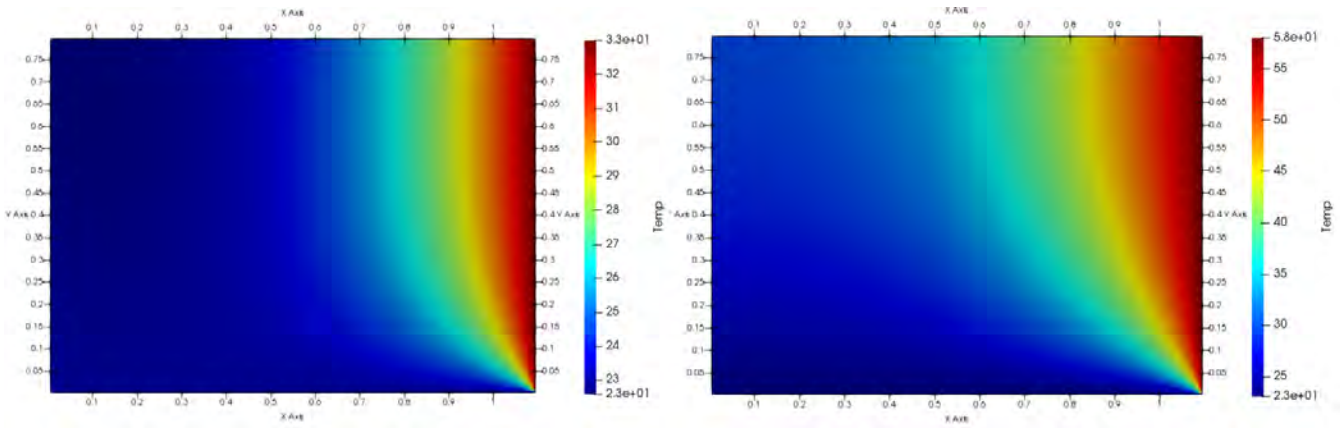

Figure 3.12: Temperature at $t = 5000s$ (left) and at $t = 10000s$ (right)

As it can be depicted in the figures above, the wall is initially at 8°, while the lower part of the wall is kept all the time at 23°, which means that it is the part of the wall at a higher temperature. As the time increases, the temperature of the right part of the wall increases, which leads to a heat transfer from right to left.

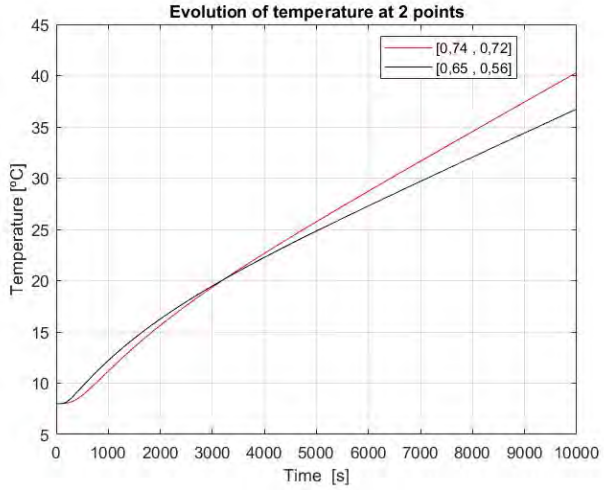

Figure 3.13: Evolution of temperature of points [0,74, 0,72] and [0,65, 0,56] with respect to time

Figure 3.13 shows the evolution of the temperature of two concrete points on the wall with respect to time. The results where compared with the ones provided by the CTTC to check that they were correct.

As the problem is discretized in space and time, it is important to analyse the results depending on the spatial and temporary discretization.

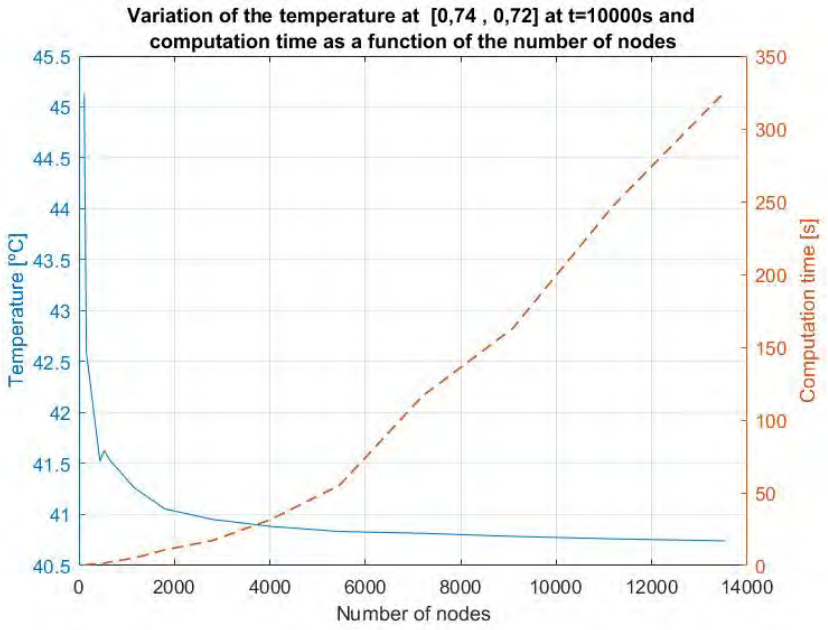

Figure 3.14: Variation of temperature at [0,74, 0,72] at t=10000s and computation time as a function of the number of nodes

It is clear that as the number of nodes increases the solution improves and tends to the exact one. There is a point where the improvement in accuracy of the results is not worth the increase in computation time. For instance, between 9090 nodes and 11200, the difference in temperature is only of $0,03°C$. However, the increase in computation time is of 84,5 s.

As the problem is transient, the selected time-step is also important and should be carefully chosen. Figure 3.15 shows that from 200 time-steps, the improvement in the results is not worth the increase in computation time. However, fewer time-steps should not be used as the error increases rapidly. It is also important to notice that the running time does not grow linearly

with the number of time-steps used.

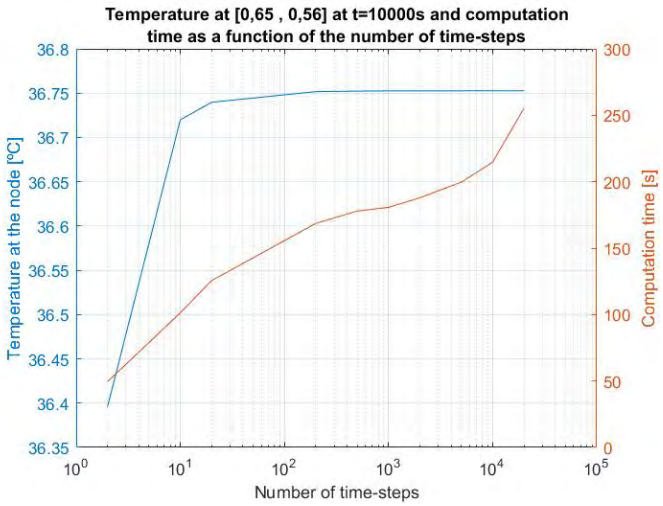

Figure 3.15: Temperature at [0,65, 0,56] at t=10000s and computation time as a function of the number of time-steps

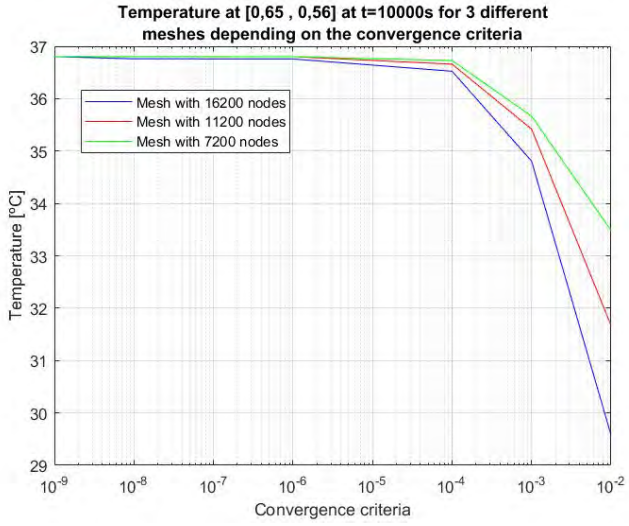

Figure 3.16: Temperature at [0,65, 0,56] at t=10000s as a function of the convergence criterion

Finally, the convergence criterion (differnce between the result of one iteration and the previous one to consider that the simulation has converged) was also studied. As the mesh gets refined, a too high convergence criterion can lead to important errors. It can be seen in figure 3.16, that even though the mesh might be better, if the convergence criterion is not accurate enough, errors can be higher. For instance, with a mesh of 16200 nodes and a convergence criterion of 0.001, the error in the temperature at $[0,65, 0,56]$ is of $5,4\%$, while a coarser mesh of only 11200 nodes, for the same convergence criterion, the error reduces up to a $3,75\%$.

3.5 Conclusions

In general, a very good agreement has been observed between the results obtained and the ones provided by the "Centre Tecnològic de Transferència de Calor" (CTTC). The advantages of the harmonic mean to calculate the thermal conductivity coefficients at the cell faces are clear in order to be able to treat all the nodes in the same way without differentiating them. The obtained results show that from 9000 nodes approximately, the improvement in the results is not worth the increase in computation time. Regarding the number of time-steps used, 200 time-steps are enough to get good results. Finally, it has been observed that, as the mesh gets refined, a lower convergence criterion needs to be used. However, it is not advisable to use convergence criteria higher than $1 \cdot 10^{-6}$, as important errors start to appear.

Chapter 4

Potential flow

4.1 Introduction

This chapter of the thesis describes the process to solve generic potential flow problems. The main characteristic of potential flow is that the curl of the velocity is zero, and thus, the velocity can be expressed as the gradient of a scalar field (i.e velocity potential). However, in this chapter, the stream function approach is used, as it is described in the next sections.

4.2 Mathematical formulation: Stream function

The mathematical formulation is based on the stream function definition. The main advantage of this approach is that the stream function definition can be used for non-irrotational flows. However, the main drawback is that the theory is only valid for steady 2D flows.

The definition of the stream function in steady and 2D flow is:

$$v_x = \frac{\rho_0}{\rho}\frac{\partial \Psi}{\partial y} \qquad v_y = -\frac{\rho_0}{\rho}\frac{\partial \Psi}{\partial x} \tag{4.2.1}$$

Where ρ_0 is the density at reference conditions (P_0, T_0). It can be proved that the stream function verifies the mass conservation equation:

$$\nabla \cdot \left(\frac{\rho_0}{\rho}\frac{\partial \Psi}{\partial y}, -\frac{\rho_0}{\rho}\frac{\partial \Psi}{\partial x} \right) = 0 \tag{4.2.2}$$

The curl of the velocity can also be calculated as follows:

$$\nabla \wedge \left(\frac{\rho_0}{\rho} \frac{\partial \Psi}{\partial y}, -\frac{\rho_0}{\rho} \frac{\partial \Psi}{\partial x} \right) = -\frac{\partial}{\partial x} \left(\frac{\rho_0}{\rho} \frac{\partial \Psi}{\partial x} \right) - \frac{\partial}{\partial y} \left(\frac{\rho_0}{\rho} \frac{\partial \Psi}{\partial y} \right) \tag{4.2.3}$$

The concept of circulation can be used, transforming a surface integral of the flux of the curl of the velocity through a surface, into a line integral of the velocity along the curve enclosed by the surface:

$$\int \nabla \wedge \mathbf{v} \; dS = \oint_C \mathbf{v} \cdot \mathbf{dl} = \Gamma \tag{4.2.4}$$

A positive circulation is measured in the counterclockwise direction.

Considering a main control volume and its adjacent ones, the circulation around the boundaries of the main control volume can be calculated as follows:

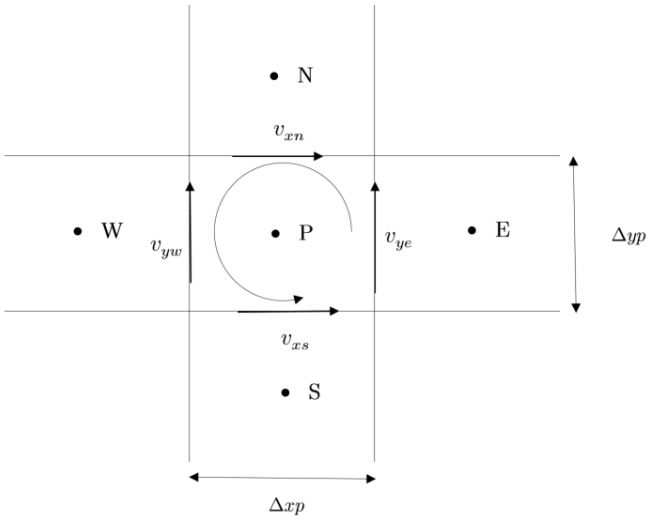

Figure 4.1: Positive velocities and circulation direction

$$\Gamma = v_{ye}\Delta y_p - v_{xn}\Delta x_p - v_{yw}\Delta y_p + v_{xs}\Delta x_p \tag{4.2.5}$$

Introducing (4.2.1) into (4.2.5):

$$\Gamma = -\frac{\rho_0}{\rho_e}\left.\frac{\partial \Psi}{\partial x}\right|_e \Delta y_p - \frac{\rho_0}{\rho_n}\left.\frac{\partial \Psi}{\partial y}\right|_n \Delta x_p + \frac{\rho_0}{\rho_w}\left.\frac{\partial \Psi}{\partial x}\right|_w \Delta y_p + \frac{\rho_0}{\rho_s}\left.\frac{\partial \Psi}{\partial y}\right|_s \Delta x_p \quad (4.2.6)$$

Using a second order approximation for the partial derivatives, equation (4.2.6) can be expressed with adjacent control volume values of Ψ:

$$\begin{aligned}\Gamma = -\frac{\rho_0}{\rho_e}\frac{\Psi_E - \Psi_P}{d_{PE}}\Delta y_p - \frac{\rho_0}{\rho_n}\frac{\Psi_N - \Psi_P}{d_{PN}}\Delta x_p + \frac{\rho_0}{\rho_w}\frac{\Psi_P - \Psi_W}{d_{PW}}\Delta y_p + \\ + \frac{\rho_0}{\rho_s}\frac{\Psi_P - \Psi_S}{d_{PS}}\Delta x_p = 0\end{aligned} \quad (4.2.7)$$

Equation (4.2.7) is equal to 0 if the curl of the velocity is 0 (i.e irrotational flow). Finally, the above equation can be expressed with coefficients as usual:

$$a_P \Psi_P = a_E \Psi_E + a_W \Psi_W + a_N \Psi_N + a_S \Psi_S \quad (4.2.8)$$

Where:

$$a_E = \frac{\rho_0}{\rho_e}\frac{\Delta y_P}{d_{PE}} \qquad a_W = \frac{\rho_0}{\rho_w}\frac{\Delta y_P}{d_{PW}} \qquad a_N = \frac{\rho_0}{\rho_n}\frac{\Delta x_P}{d_{PN}} \qquad a_S = \frac{\rho_0}{\rho_s}\frac{\Delta x_P}{d_{PS}}$$

$$a_P = a_E + a_N + a_S + a_W \qquad b_P = 0$$

When the domain involves regions of fluid and solid, the blocking-off method needs to be used. To apply this technique, the centroids of each control volume are evaluated. If the centroid lays inside the solid region, the whole control volume is considered as solid. However, if the centroid lays inside the fluid region, it is considered as a fluid control volume.

In case of a solid-fluid interface, the continuity of the velocity must be satisfied. To ensure this condition, the harmonic mean to evaluate the densities on the control volume faces needs to be used, as it is demonstrated now:

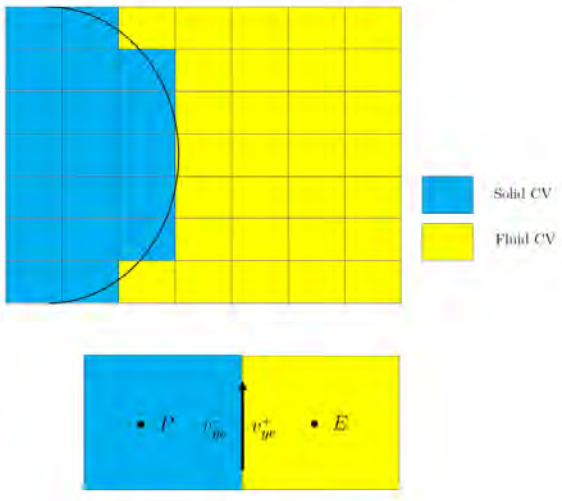

Figure 4.2: Velocity evaluation at interface between solid and fluid CVs

$$v_{ye} = -\frac{\rho_0}{\rho_e^-}\frac{\partial \Psi}{\partial x}\Big]_e^- = -\frac{\rho_0}{\rho_e^+}\frac{\partial \Psi}{\partial x}\Big]_e^+ \tag{4.2.9}$$

Discretizing the previous equation:

$$v_{ye} = -\frac{\rho_0}{\rho_P}\frac{\Psi_e - \Psi_P}{d_{Pe}} = -\frac{\rho_0}{\rho_E}\frac{\Psi_E - \Psi_e}{d_{Ee}} \tag{4.2.10}$$

From equation (4.2.10) it can be easily obtained:

$$v_{ye} = -\frac{\rho_0}{\rho_e}\frac{\Psi_E - \Psi_P}{d_{PE}} \tag{4.2.11}$$

Where ρ_0/ρ_e is calculated as a harmonic mean of the nodal values:

$$\frac{\rho_0}{\rho_e} = \frac{d_{PE}}{\frac{d_{Pe}}{\rho_0/\rho_P} + \frac{d_{Ee}}{\rho_0/\rho_E}} \tag{4.2.12}$$

4.3 Incompressible potential flow around a cylinder (rotating and non-rotating)

The benchmark problem is shown in the figure below:

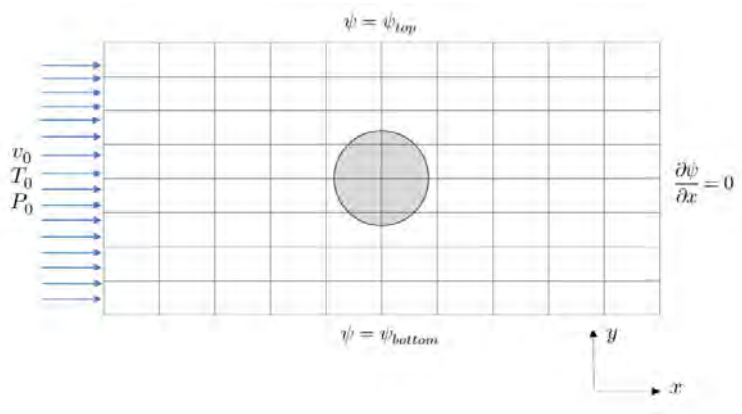

Figure 4.3: Schematization of the problem

A rotating and non-rotating cylinder is studied in free flow conditions.

The boundary conditions are now summarised:

- Inlet:$\Psi = \Psi_{known}$
- Top:$\Psi = \Psi_{top}$
- Bottom:$\Psi = \Psi_{bottom}$
- Outlet: If parallel flow is considered (i.e, outlet is far enough from the cylinder), then $\frac{\partial \Psi}{\partial x} = 0$

Before presenting the final algorithm, it is important to notice one thing. If the cylinder is not rotating, the value of the stream function around the cylinder is known. However, for the rotating cylinder, this value is not known and needs to be calculated by iteration. To find the value of the stream function around the cylinder, the bisection method is used. An interval of possible stream function values is set, and this interval is bisected until the value of the circulation around the cylinder is the correct one (for

a rotating cylinder the circulation is $\Gamma = -2\pi R(V_\theta + 2V_\infty)$, where V_θ stand for the tangential velocity on the top of the cylinder [14]). This process is outlined in the following algorithm:

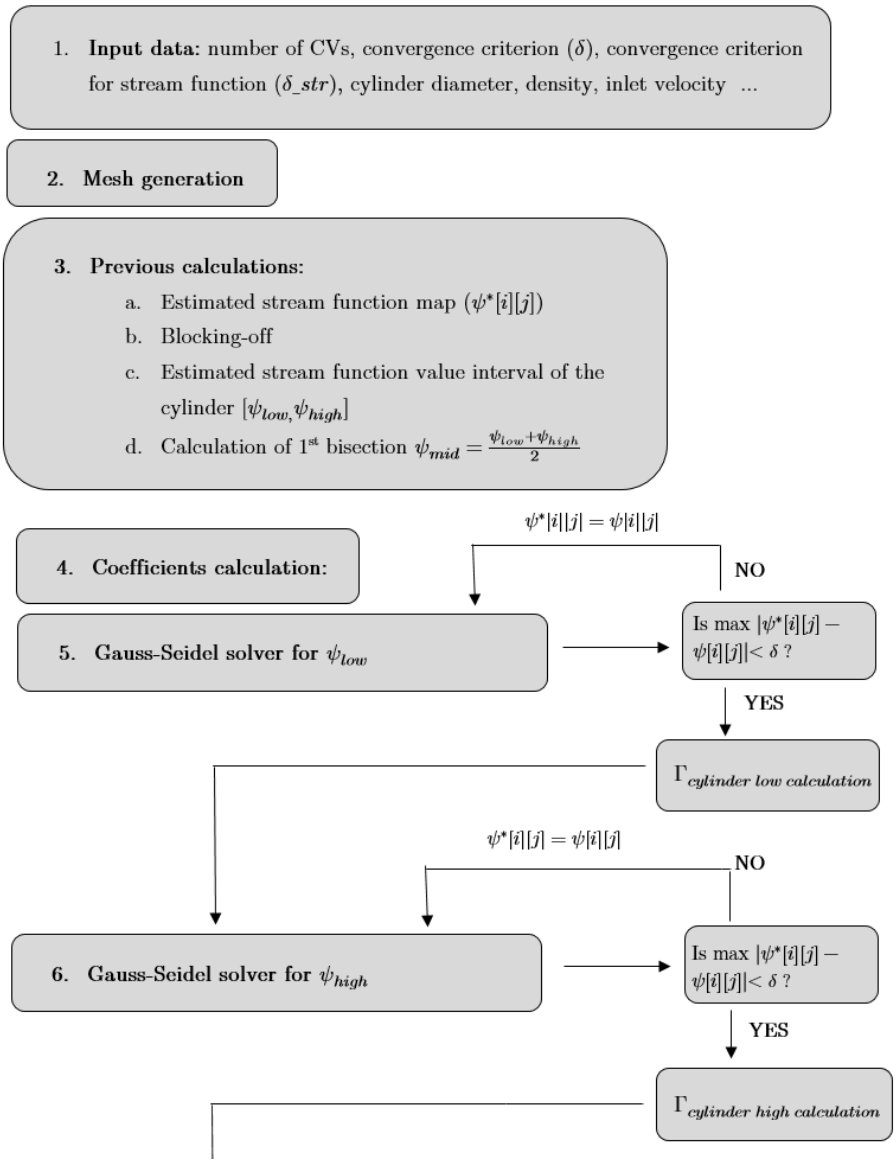

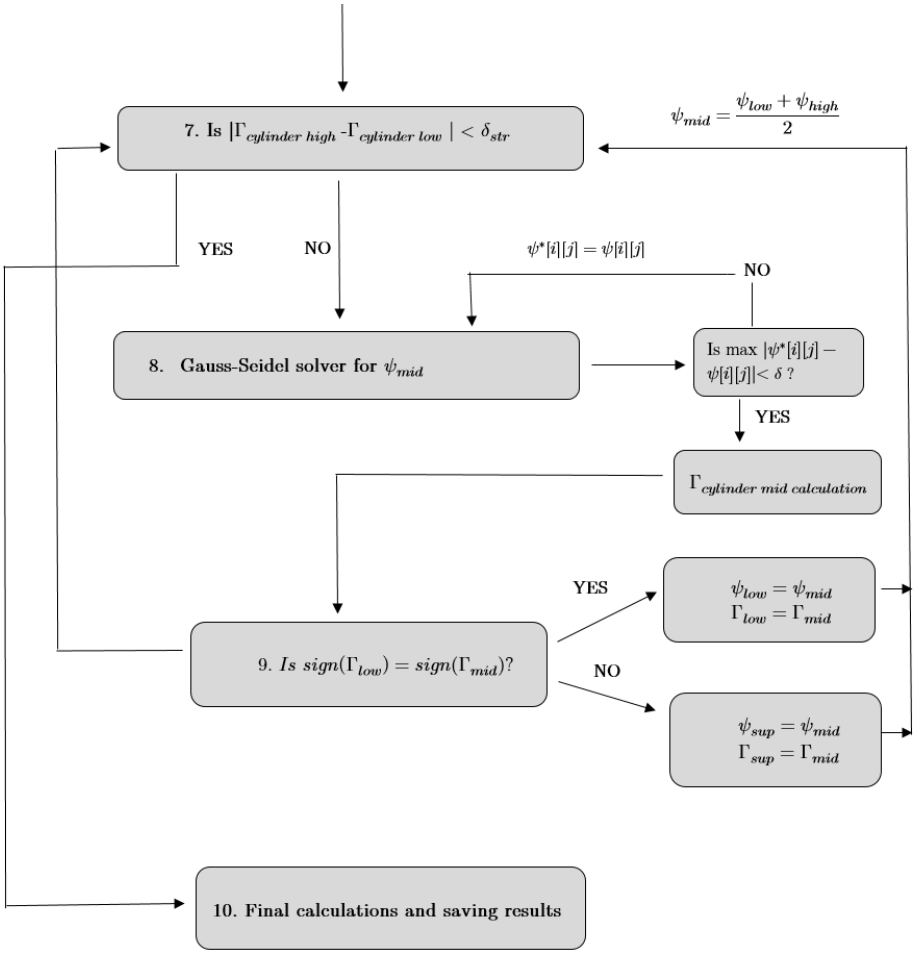

Figure 4.4: Algorithm for potential flow

4.4 Non-rotating cylinder results

The first case that is solved is the incompressible flow around a non-rotating cylinder for a free stream velocity of $V_\infty = 10\ m/s$. The results are compared with the analytical solution extracted from [14].

The mesh was refined around the cylinder in order to capture correctly the velocity variation around the geometry. However, near the inlet and

the outlet zones, velocity gradients are less pronounced, which means that a coarser mesh can be used, as it can be seen in figure 4.5.

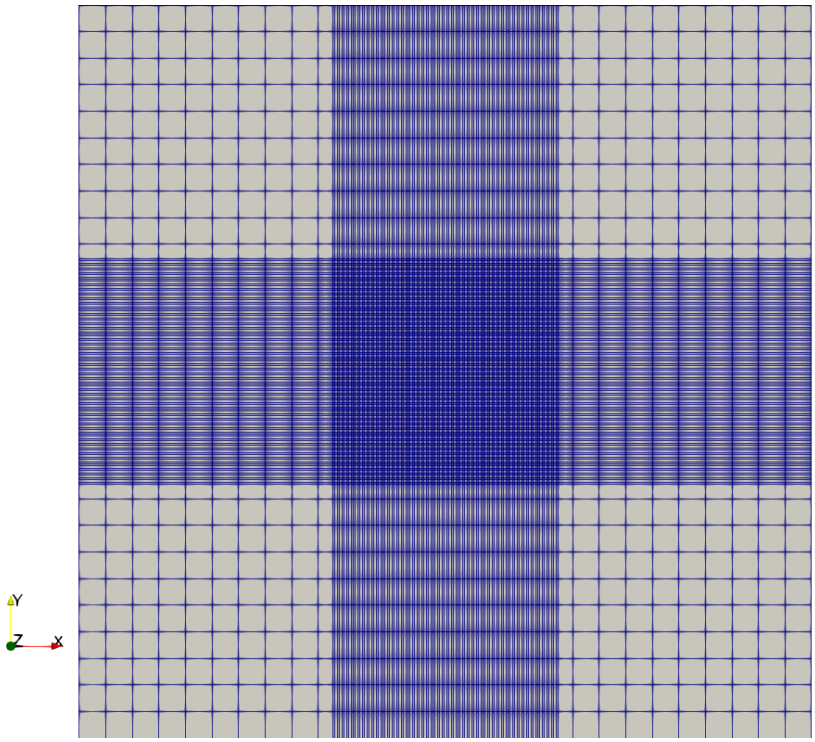

Figure 4.5: Mesh around the cylinder

First of all, a plot of the values of the stream function is shown. It is important to notice that the isolines of the stream function are, in fact, streamlines of the flow around the cylinder. Another important thing to notice is that the value of the stream function depends on a reference value, that is why these results are not compared with an analytical solution.

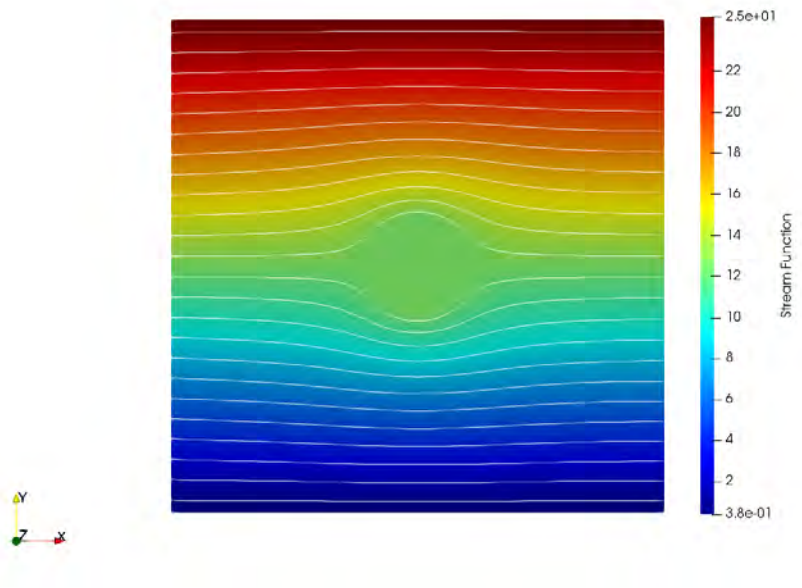

Figure 4.6: Stream Function values and Streamlines

As it can be seen, the flow is totally symmetric about the horizontal and vertical axes through the center of the cylinder. As a consequence, velocity and pressure distribution are also symmetric about both axes, which leads to the d'Alembert's paradox, as it is seen in the figures below.

In the next page, figure 4.7 is a representation of the values of the x and y components of the velocity around the cylinder. Figure 4.8 shows the modulus of the velocity around the cylinder and the comparison with the analytical solution.

It can be seen that there are two stagnation points on $\theta = 0$ and $\theta = 2\pi$ (the reference point and direction of θ can be seen in the figure below). The model is capable of capturing the velocity around the cylinder quite accurately, except on the zones around $\theta = \pi/2$ and $\theta = 3\pi/2$. On the top and on the bottom of the cylinder, there are important variations in the velocity modulus, and, as a consequence, the biggest error happens in these regions.

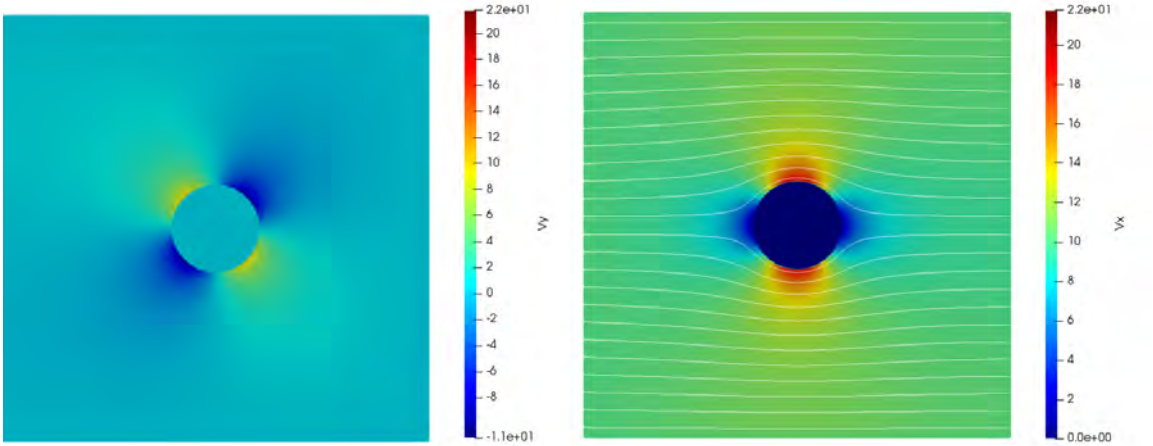

Figure 4.7: V_x (right) and V_y (left) in m/s

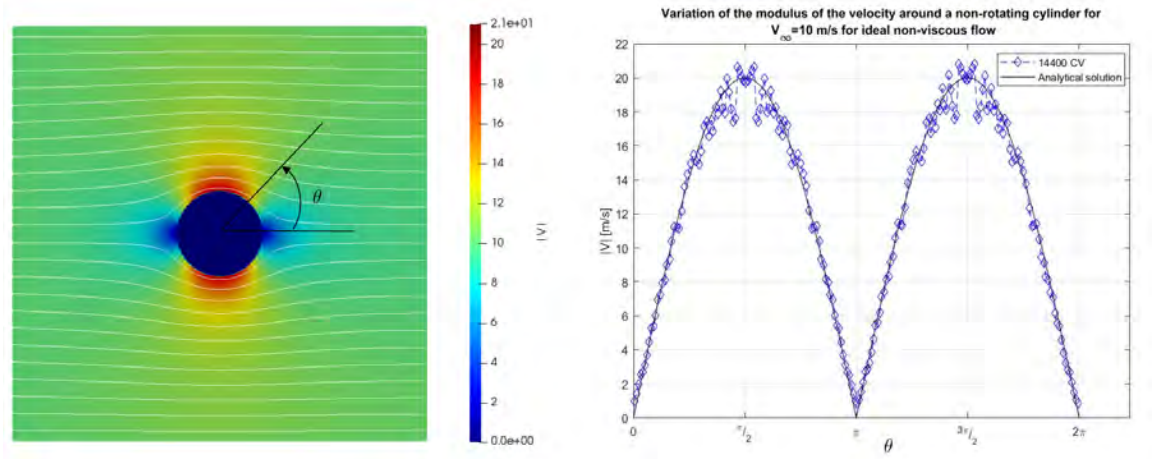

Figure 4.8: Velocity modulus around the cylinder and comparison with analytical solution

Nevertheless, the absolute error can be decreased by using a more refined mesh, using higher order approximations for the derivatives (remember that a second order scheme has been used), or using a more refined method than the blocking-off for the interfaces between solid and fluid control volumes.

The pressure coefficient can be calculated using the Bernoulli equation (conservation of energy), and eventually, it can be expressed in terms of the

square of the ratio of velocity and the free stream velocity:

$$Cp = 1 - \left(\frac{V}{V_\infty}\right)^2 \tag{4.4.1}$$

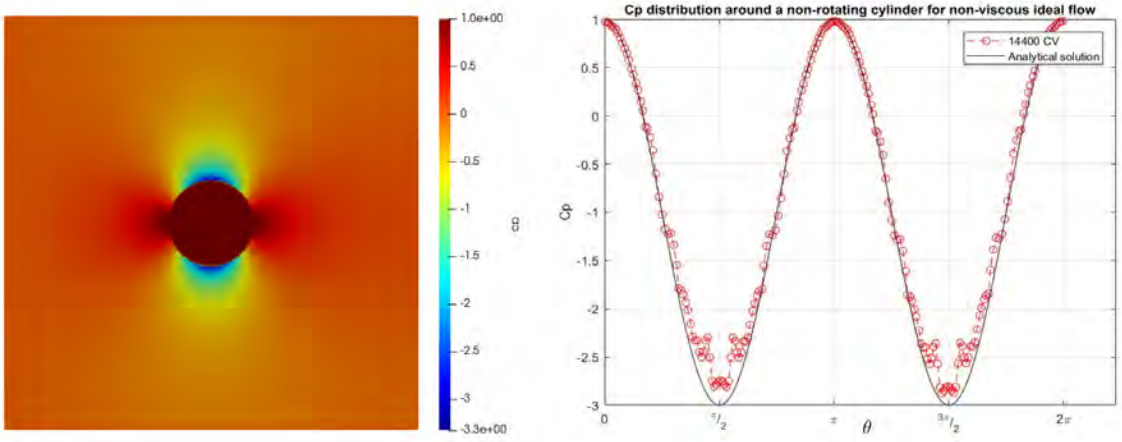

Figure 4.9: Cp around the cylinder and comparison with analytical solution

As shown in Figure 4.9, the same errors appear near the top and the bottom of the cylinder. However, around the rest of this geometry the results are quite accurate. An important thing to notice is that the pressure distribution over the top and bottom are balanced, which means that the cylinder does not generate a lifting force. Similarly, the pressure at the front is exactly balanced by the pressure at the back of the cylinder, which means that there is no net drag force (d'Alembert's paradox, as mentioned before).

4.5 Rotating cylinder results

In this section, potential flow around a rotating cylinder is studied. The velocity and coefficient of pressure are plotted for different rotating velocities.

As shown in figure 4.10, the streamlines are not symmetric about the x axis anymore. Air is sped up on the top of the cylinder, creating a depression zone on its top, and thus, a net vertical lifting force appears (Magnus

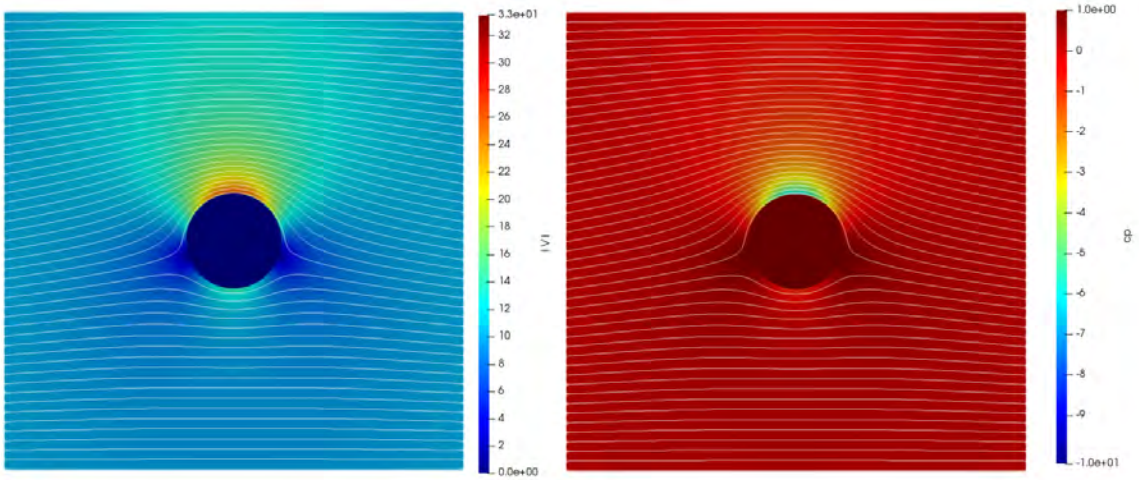

Figure 4.10: |V| and Cp for a rotating cylinder generating a circulation of $\Gamma = 40m^2/s$

effect). The lift per unit span can be calculated using the Kutta-Joukowski theorem ($L' = \rho_\infty V_\infty \Gamma$) However, the flow is still symmetric about the y axis, which means that there is no net drag force.

Another important thing to notice is that the coefficient of pressure on top of the cylinder has decreased considerably in comparison with the one for a non-rotating cylinder at the same point, reaching a minimum value of $Cp = -6$. However, the coefficient of pressure on the bottom of the cylinder has increased, from -3 to approximately -1.

Finally, it is important to stand out that the stagnation points have moved to the bottom half of the cylinder, as it is predicted by the potential theory.

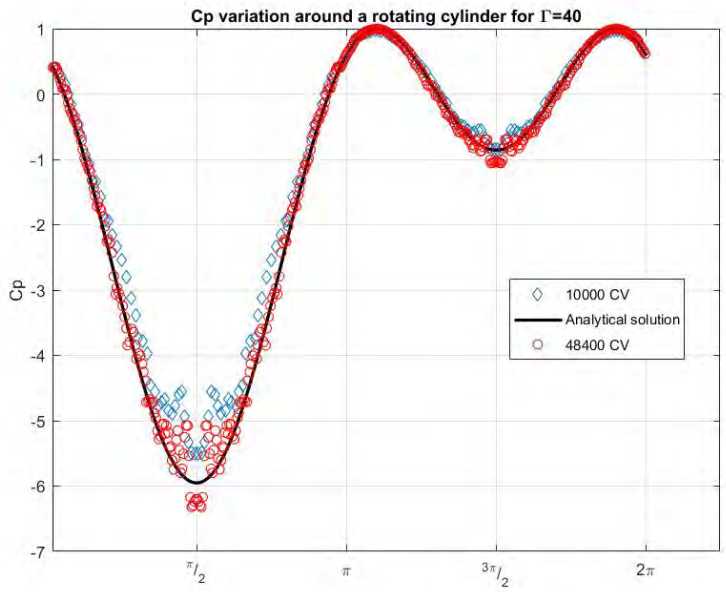

Figure 4.11: Cp for a rotating cylinder generating a circulation of $\Gamma = 40m^2/s$ and comparison with analytical solution

Figure 4.11 is the Cp computed for a rotating cylinder generating a circulation of $\Gamma = 40m^2/s$ for two different meshes, and its comparison with the analytical solution. It is noticeable that, as the mesh is refined, the maximum error decreases. Again, as it is seen with the non-rotating cylinder results, the maximum error happens on the top and bottom of the geometry, where results are bad for coarser meshes. However, the results in the rest of the cylinder are really accurate.

As the rotational speed of the cylinder increases, a certain value of circulation is reached for which the two stagnation points merge into one at the bottom of the cylinder and end up separating from its surface. This critical circulation value is $\Gamma = 4\pi V_\infty R$, and for this specific problem with $V_\infty = 10\ m/s$, this value is $\Gamma = 125,66\ m^2/s$.

As it is depicted in figure 4.12, for a higher circulation of $\Gamma = 170\ m^2/s$ the stagnation point has separated completely from the surface of the cylinder. The pressure coefficient on its top is more negative, which means that

the net lift force generated by the spinning cylinder is larger.

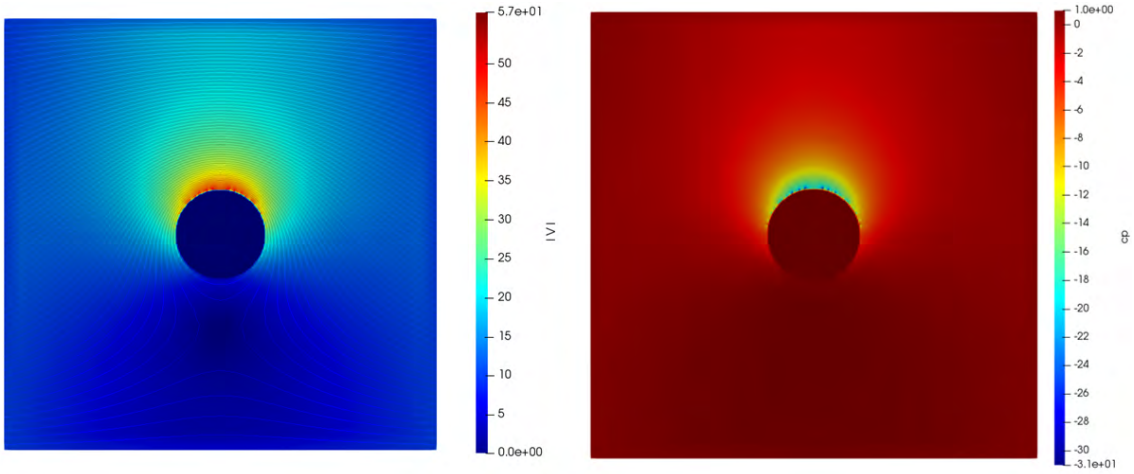

Figure 4.12: |V| and Cp for a cylinder generating a circulation of $\Gamma = 170 m^2/s$

4.6 Mesh discretization study

As both problems studied are solved in steady state conditions, there is no time discretization that should be studied. A a consequence, the spatial discretization is the main factor that should be analysed regarding the discretization of the problem.

As it has been said before, a non-uniform mesh has been used, so the spatial discretization that is considered to do the mesh study is the one around the cylinder. The study is done with the rotating cylinder generating a circulation of $\Gamma = 40\ m^2/s$. Figure 4.13 shows that as the mesh is refined, the maximum absolute error decreases significantly. This maximum error happens, as it has already been seen, at the top and at the bottom of the cylinder. Using higher order schemes would mean more accurate results for the same mesh. However, the results got are accurate enough to prove the proper functioning of the code.

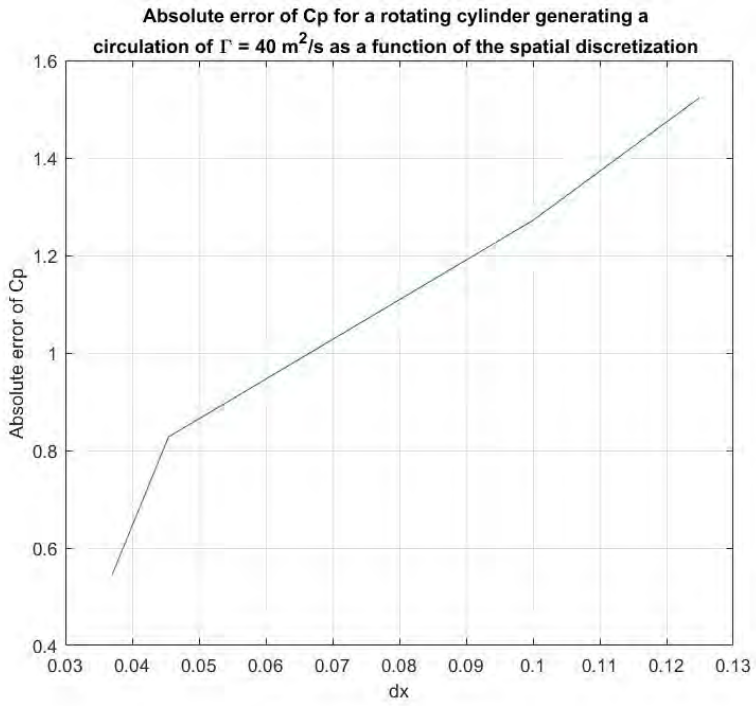

Figure 4.13: Absolute error of Cp for a rotating cylinder generating a circulation of $\Gamma = 40 m^2/s$ with respect to cell size around the cylinder

4.7 Conclusions

In general, reasonably good agreement has been observed between the simulated results and the ones predicted by the potential theory. However, important errors appear on the top and bottom parts of the cylinder for both velocity and coefficient of pressure. The error can be decreased by using a finer mesh, which increases considerably computation time. Another option could be to use higher order approximations for the derivatives or to use a more sophisticated method than the blocking-off to treat the interfaces between solid and fluid control volumes. The bisection method used to find the value of the stream function around the rotating cylinder proved to be an efficient method, as it converged relatively fast, with the drawback of an important increase in computation time.

Chapter 5

Convection-diffusion equation

5.1 Introduction

Until now, it has been presented a generic unsteady diffusion equation. However, Navier-Stokes equations are a particular case of a convection-diffusion equation where the transport of a physical quantity (energy, temperature...) is not only due to concentration gradients, but also due to the fluid flow. In this chapter, a generic convection-diffusion equation is studied, given the flow field as an input. The objective is to study different schemes to discretize the convective term.

5.2 Mathematical formulation

The generic form of the convection-diffusion transport equation can be written as:

$$\frac{\partial(\rho\phi)}{\partial t} + \nabla \cdot (\rho \mathbf{v} \phi) = \nabla \cdot (\Gamma_\phi \nabla \phi) + S_\phi \tag{5.2.1}$$

Where ϕ is a generic variable like velocity, temperature, entropy... The first term of the left-hand side is the unsteady term, the second term of the left-hand side is the convective term, the first term of the right-hand side is the diffusion term and the last term of the right-hand side is the source term.

Expanding the first partial derivative of (5.2.1) and applying the mass conservation equation, the above equation can be written as:

$$\rho\frac{\partial\phi}{\partial t} + \rho\mathbf{v}\cdot\nabla\phi = \nabla\cdot(\Gamma_\phi\nabla\phi) + S_\phi \tag{5.2.2}$$

It is important to notice that to get equation (5.2.2) it has not been assumed constant density, which means that the above equation is still absolutely valid for compressible flow.

Therefore, the Navier-Stokes equations for a perfect gas can be expressed as:

Equation	$\boldsymbol{\phi}$	Γ_ϕ	$\mathbf{S}_\phi$
Mass	1	0	0
Momentum	$\mathbf{v}$	μ	$\nabla\cdot(\boldsymbol{\tau}-\mu\nabla\mathbf{v}) - \nabla P + \rho\mathbf{g}$
Energy	T	$\frac{\lambda}{C_v}$	$\frac{1}{C_v}(-\nabla\cdot\mathbf{q}^r - p\nabla\cdot\mathbf{v} + \boldsymbol{\tau}:\nabla\mathbf{v}$

Table 5.1: Convective term, diffusion term and source term of the Navier-Stokes equations. Extracted from [4]

Conservation of mass equation discretization

The continuity equation in differential form can be written as:

$$\frac{\partial\rho}{\partial t} + \nabla\cdot(\rho\mathbf{v}) = 0 \tag{5.2.3}$$

Integrating over time and volume implicitly:

$$\int_{t_n}^{t^{n+1}}\int_{V_p}\frac{\partial\rho}{\partial t}dVdt + \int_{t_n}^{t^{n+1}}\int_{V_p}\nabla\cdot(\rho\mathbf{v})dVdt = 0 \tag{5.2.4}$$

And considering a second order approximation for the first volume integral, the continuity equation gets discretized as follows:

$$(\rho_P^{n+1} - \rho_P^n)Vp + (\dot{m_e}^{n+1} - \dot{m_w}^{n+1} + \dot{m_n}^{n+1} - \dot{m_s}^{n+1})\Delta t = 0 \tag{5.2.5}$$

Unsteady term discretization

Integrating implicitly over time and volume the unsteady term:

$$\int_{t_n}^{t^{n+1}} \int_{V_p} \frac{\partial(\rho\phi)}{\partial t} dV dt \approx Vp \int_{t_n}^{t^{n+1}} \frac{\partial(\rho_p \phi_p)}{\partial t} dt = V_p(\rho_p^{n+1}\phi_p^{n+1} - \rho_p^n \phi_p^n) \quad (5.2.6)$$

Where it has been considered a second order approach for the density and variable of interest (ϕ) to approximate the volume integral.

Convective term discretization

Integrating implicitly over time and volume the convective term:

$$\int_{t_n}^{t^{n+1}} \int_{V_p} \nabla \cdot (\rho \mathbf{v} \phi) dV dt \quad (5.2.7)$$

Applying the divergence theorem to the equation above:

$$\int_{t_n}^{t^{n+1}} \int_{S_f} \rho \mathbf{v} \phi \cdot \mathbf{n} dS dt \approx (\dot{m_e}^{n+1}\phi_e^{n+1} - \dot{m_w}^{n+1}\phi^{n+1} + \dot{m_n}^{n+1}\phi_n^{n+1} - \dot{m_s}^{n+1}\phi_s^{n+1})\Delta t \quad (5.2.8)$$

Where an implicit approach has been used for the time integral once again, and the property of interest (ϕ) has been considered constant along the surface.

Diffusion term discretization

Integrating implicitly over time and volume, the diffusion term:

$$\int_{t_n}^{t^{n+1}} \int_{V_p} \nabla \cdot (\Gamma_\phi \nabla \phi) dV dt \tag{5.2.9}$$

Applying the divergence theorem to the equation above:

$$\int_{t_n}^{t^{n+1}} \int_{S_f} (\Gamma_\phi \nabla \phi) \cdot \mathbf{n} dS dt \approx \left(\Gamma_e \frac{\phi_E^{n+1} - \phi_P^{n+1}}{d_{PE}} S_e \right. \\ \left. -\Gamma_w \frac{\phi_P^{n+1} - \phi_W^{n+1}}{d_{PW}} S_w + \Gamma_n \frac{\phi_N^{n+1} - \phi_P^{n+1}}{d_{PN}} S_n - \Gamma_s \frac{\phi_P^{n+1} - \phi_S^{n+1}}{d_{PS}} S_s \right) \Delta t \tag{5.2.10}$$

Where a second order approach has been used to approximate the gradient of the variable ϕ and the diffusive coefficient (Γ) has been considered constant on each surface.

Source term discretization

Finally, the source term is discretized integrating over time and volume:

$$\int_{t_n}^{t^{n+1}} \int_{V_p} S_\phi dV dt \approx \bar{S_\phi}_P V_p \Delta t = (S_c^{\phi n+1} + S_P^{\phi n+1} \phi_P^{n+1}) V_p \Delta_t \tag{5.2.11}$$

Where the source term has been linearized.

General convection-diffusion equation discretization

Combining the discretizations made above, the general equation can be obtained. For convenience, the superscript n corresponding to the previous time step is substituted by the superscript 0, while the superscript n+1 is dropped away.

$$\frac{\rho_P \phi_P - \rho_P^0 \phi_P^0}{\Delta t} V_P + (\dot{m}_e \phi_e - \dot{m}_w \phi_w + \dot{m}_n \phi_n - \dot{m}_s \phi_s) = \\ D_e(\phi_E - \phi_P) - D_w(\phi_P - \phi_W) + D_n(\phi_N - \phi_P) - D_s(\phi_P - \phi_S) \\ +(S_c^\phi + S_P^\phi \phi_P) V_P \tag{5.2.12}$$

Where, $D_e = \Gamma_e S_e / d_{PE}$, $D_w = \Gamma_w S_w / d_{PW}$, etc.

Subtracting $\phi_P \cdot Equation(5.2.5)$ to each side of Equation (5.2.12), the general convection-diffusion equation can be written as:

$$\begin{aligned} \rho_P^0 \frac{\phi_P - \phi_P^0}{\Delta t} V_P + \dot{m}_e(\phi_e - \phi_P) - \dot{m}_w(\phi_w - \phi_P) + \dot{m}_n(\phi_n - \phi_P) \\ -\dot{m}_s(\phi_s - \phi_P) = D_e(\phi_E - \phi_P) - D_w(\phi_P - \phi_W) + D_n(\phi_N - \phi_P) \\ -D_s(\phi_P - \phi_S) + (S_c^\phi + S_P^\phi \phi_P) V_P \end{aligned} \tag{5.2.13}$$

Equation (5.2.13) is second order accurate in the diffusion and source term. The order of accuracy of the overall scheme depends on the scheme used to approximate the convective term.

Evaluation of the convective term (I)

- **Upwind-difference scheme (UDS)**: The upwind scheme approximates the convected value of property (ϕ) at the face as the one of the upwind cell.

Figure 5.1: Upwind difference scheme

Where the letters 'U' and 'D' in red represent the upstream and downstream nodes respectively. This is a first order scheme, really stable. However, numerical diffusion is an important problem with this approximation.

$$\phi_e - \phi_P = f_e(\phi_E - \phi_P) \qquad \begin{cases} f_e = 0 & if \quad \dot{m}_e > 0 \\ f_e = 1 & if \quad \dot{m}_e < 0 \end{cases} \tag{5.2.14}$$

- **Central difference scheme (CDS)**: This is a second order scheme that assumes a linear variation of the property ϕ. For the east face of a control volume, notation would be as follows:

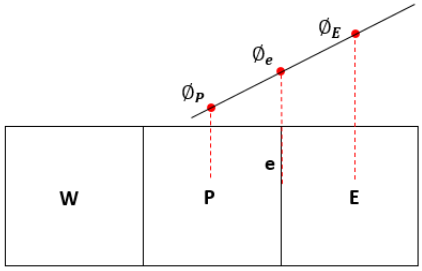

Figure 5.2: Central difference scheme

$$\phi_e - \phi_P = f_e(\phi_E - \phi_P) \qquad f_e = d_{Pe}/d_{PE} \tag{5.2.15}$$

- **Exponential Difference Scheme (EDS)**: The exponential difference scheme is a first order scheme that evaluates the property ϕ considering the analytical solution of the 2D steady convection-diffusion equation without source term:

$$\phi_e - \phi_P = f_e(\phi_E - \phi_P) \qquad f_e = \frac{e^{P_e d_{Pe}/d_{PE}} - 1}{e^{P_e} - 1}, \tag{5.2.16}$$

Where, $Pe = \frac{\rho_e V_{xe} d_{PE}}{\Gamma_e}$.

Normalized variables for higher-order schemes

The schemes presented until now only use adjacent nodes to calculate the value of the convected property at the cell face. However, there are other

schemes such as QUICK, SUDS or SMART, that use a higher cell molecule. That is why it is recommended to use normalised variables to apply these schemes.

First of all, according to the mass flow direction, three nodes should be considered: from a reference point at the cell face, the D node refers to the downstream node, the C node refers to the first upstream node and the U node refers to the second upstream node:

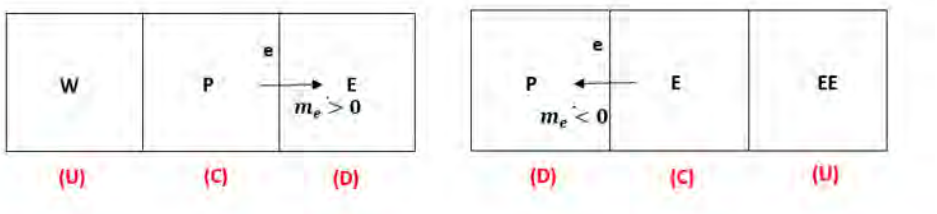

Figure 5.3: D, C and U nodes to normalise variables

Once these nodes have been identified, the normalised coordinates and normalised property ϕ can be calculated according to:

$$\hat{x} = \frac{x - x_U}{x_D - x_U} \qquad \hat{\phi} = \frac{\phi - \phi_U}{\phi_D - \phi_U} \tag{5.2.17}$$

Finally, the value of the convected property at the cell face can be calculated as follows:

$$\phi_f = \phi_U + (\phi_D - \phi_U)\hat{\phi}_f \tag{5.2.18}$$

Where the subscript f stands for the concrete face.

Evaluation of the convective term II: Higher order schemes

With the normalised variable, other schemes can be applied:

- **Second order upwind linear extrapolation (SUDS)**: This is a second order scheme that uses a linear extrapolation using two upstream points instead of only one, resulting in a second order scheme.

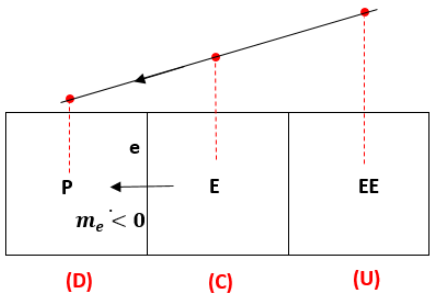

Figure 5.4: Second Order Upwind linear extrapolation Scheme

$$\hat{\phi_f} = \frac{\hat{x_f}}{\hat{x_C}}\hat{\phi_C} \tag{5.2.19}$$

- **Quadratic upwind interpolation for convective kinematics (QUICK)**: This is a second/third order scheme that fits a quadratic curve using two upstream nodes to evaluate the value of the convected property at the cell face:

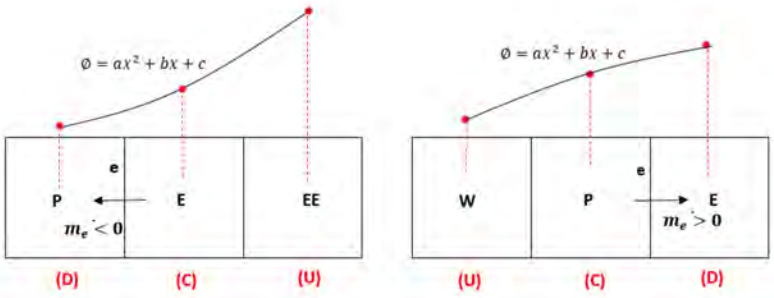

Figure 5.5: QUICK Scheme

$$\hat{\phi_f} = \hat{x_f} + \frac{\hat{x_f}(\hat{x_f} - 1)}{\hat{x_c}(\hat{x_c} - 1)}(\hat{\phi_c} - \hat{x_c}) \tag{5.2.20}$$

- **Sharp and Monotonic Algorithm for Realistic Transport (SMART)**: The CDS, SUDS and QUICK schemes presented above may present

numerical instabilities in implicit calculations. SMART satisfies the conditions for stability and accuracy formulated in [15], which leads to a bounded convective scheme:

$$\begin{cases} if \quad 0 < \hat{\phi_C} < \frac{\hat{x_C}}{3} & \hat{\phi_f} = -\frac{\hat{x_f}(1-3\hat{x_c}+2\hat{x_f})}{\hat{x_c}(\hat{x_c}-1)}\hat{\phi_c} \\ if \quad \frac{\hat{x_c}}{3} < \hat{\phi_C} < \frac{\hat{x_C}}{\hat{x_f}}(1+\hat{x_f}-\hat{x_c}) & \hat{\phi_f} = \frac{\hat{x_f}(\hat{x_f}-\hat{x_C})}{1-\hat{x_C}} + \frac{\hat{x_f}(\hat{x_f}-1)}{\hat{x_C}(\hat{x_C}-1)}\hat{\phi_C} \\ if \quad \frac{\hat{x_C}}{\hat{x_f}}(1+\hat{x_f}-\hat{x_C}) < \hat{\phi_c} < 1 & \hat{\phi_f} = 1 \\ Otherwise & \hat{\phi_f} = \hat{\phi_C} \end{cases} \tag{5.2.21}$$

Deferred correction approach

When a higher-order schemes is used, the size of the computational molecule can have an important effect in storage and effort to solve the equations. Generally speaking, it is interesting to use only the nearest neighbours of the main node in the left-hand side of the equation to solve the problem, as it usually leads to a tridiagonal matrix, which is easy to solve. However, with the schemes presented above this is not possible. [16]

To solve this problem, the deferred correction approach is used. The basic idea is to keep the higher order terms in the right-hand side of the equation, calculated explicitly, and use a lower order approximation (UDS, for example), which is added implicitly and subtracted explicitly:

$$\phi_f^{HRS} - \phi_P = (\phi_f^{UDS} - \phi_P) + (\phi_f^{HRS*} - \phi_f^{UDS*}) \tag{5.2.22}$$

Where the superscript '*' indicates that the value is calculated at the previous iteration, and the values without superscript indicate the current calculated values. One convergence is reached, $\phi_f^{UDS*} \approx \phi_f^{UDS}$, which means that $\phi_f^{HRS} - \phi_P \approx \phi_f^{HRS*} - \phi_P$. It is important to notice that this method gives good results only when convergence is achieved, i.e steady state is reached. This approach would give bad results if the final results obtained were at a concrete time step previous to the steady state.

Discretization equation and coefficients (Higher order schemes and deferred correction approach)

Using a higher order scheme and, using the deferred correction approach, the discretization equation and coefficients are:

$$a_P\phi_P = a_E\phi_E + a_W\phi_W + a_N\phi_N + a_S\phi_S + b_P; \tag{5.2.23}$$

Where:

$$a_E = D_e - \frac{\dot{m}_e - |\dot{m}_e|}{2}; \qquad a_W = D_w + \frac{\dot{m}_w + |\dot{m}_w|}{2};$$

$$a_N = D_n - \frac{\dot{m}_n - |\dot{m}_n|}{2}\ ; \qquad a_S = D_s + \frac{\dot{m}_s + |\dot{m}_s|}{2}\ ;$$

$$b_p = \frac{\rho_P^0 V_p}{\Delta t}\phi_P^0 + S_c^\phi V_p - \dot{m}_e(\phi_e^{HRS*} - \phi_e^{UDS*}) + \dot{m}_w(\phi_w^{HRS*} - \phi_w^{UDS*}) - \dot{m}_n(\phi_n^{HRS*} - \phi_n^{UDS*}) + \dot{m}_s(\phi_s^{HRS*} - \phi_s^{UDS*})$$

$$a_P = a_E + a_W + a_N + a_S + \frac{\rho_P^0 V_p}{\Delta t} - S_p^\phi V_p$$

The final algorithm is presented in the following page:

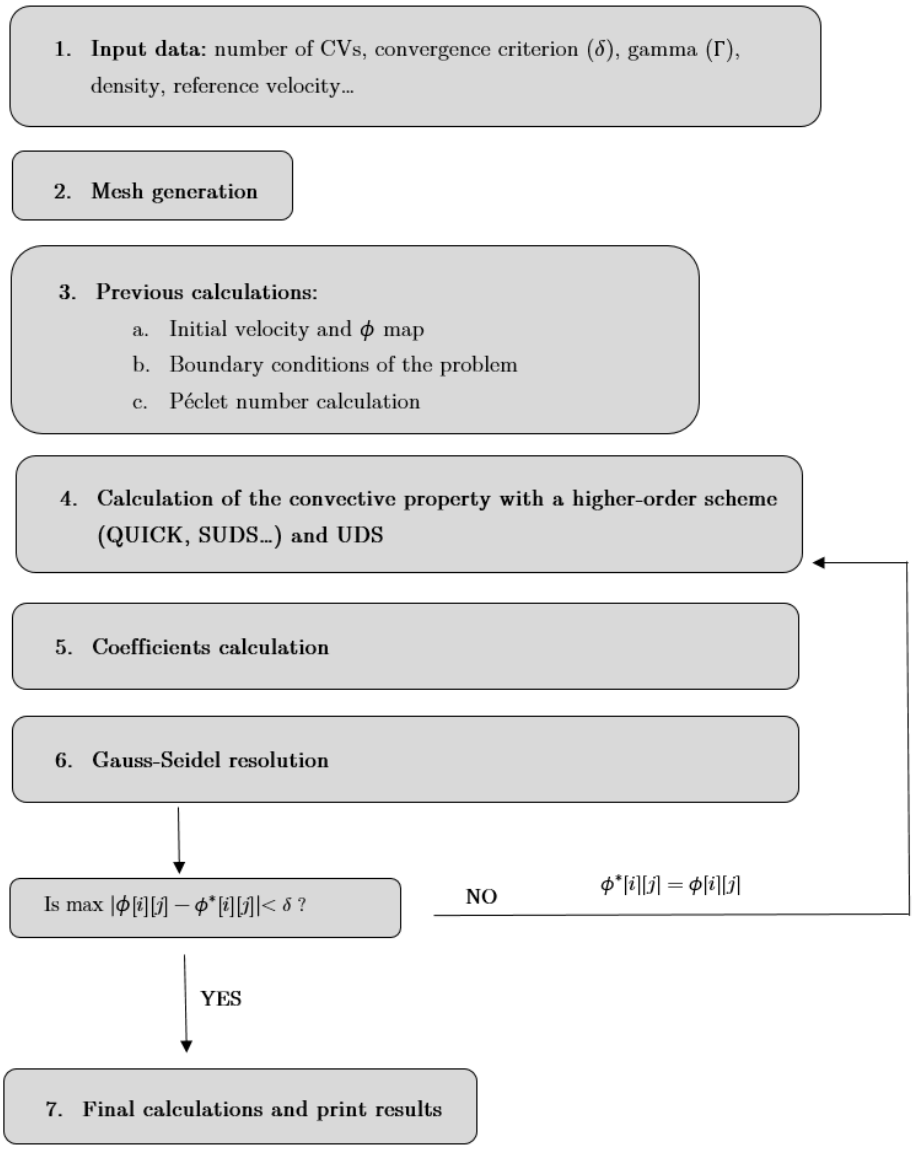

Figure 5.6: Algorithm for the convection-diffusion problem

5.3 Unidimensional flow with an unidimensional variation of the variable solved in the same direction of the flow

For this particular problem, an analytical solution for the steady state exists. It is an exponential function for a concrete value of the velocity field. The problem to study is sketched below:

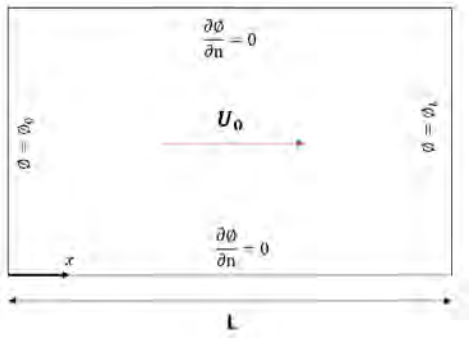

Figure 5.7: Unidimensional flow with an unidimensional variation of the variable solved in the same direction of the flow

For a given velocity field like:

$$u(x, y) = U_0$$
$$v(x, y) = 0$$

The exact solution has the following form:

$$\frac{\phi - \phi_0}{\phi_L - \phi_0} = \frac{exp(Px/L) - 1}{exp(P) - 1} \tag{5.3.1}$$

Where P is the Péclet number: $P = \rho u L/\Gamma$

First of all, the problem is solved with a coarse mesh of only $5x5$ control volumes and different Péclet numbers using the UDS, SUDS, QUICK and CDS schemes.

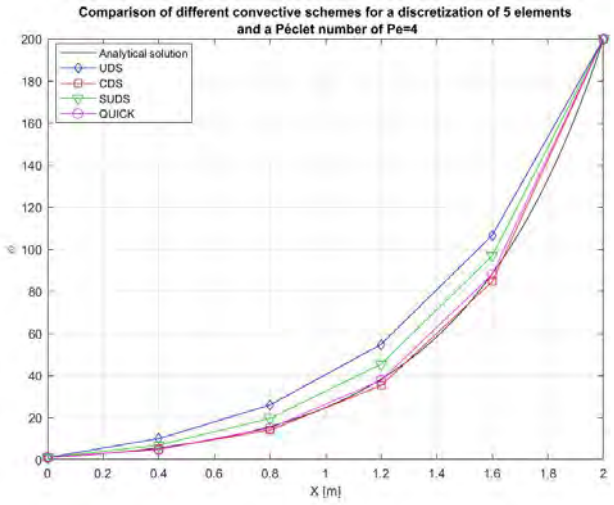

Figure 5.8: Unidimensional flow with an unidimensional variation of the variable solved in the same direction of the flow with 5x5 mesh and $Pe = 4$

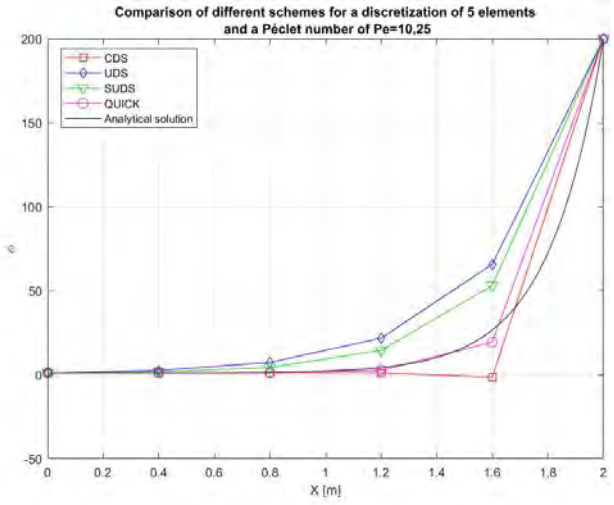

Figure 5.9: Unidimensional flow with an unidimensional variation of the variable solved in the same direction of the flow with 5x5 mesh and $Pe = 10,25$

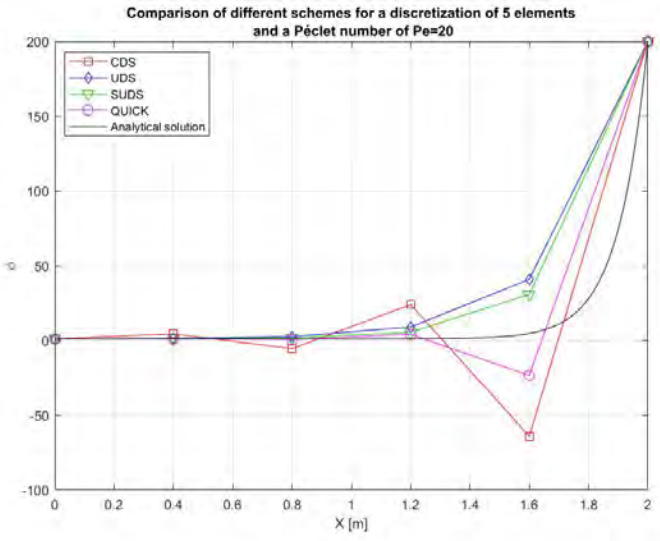

Figure 5.10: Unidimensional flow with an unidimensional variation of the variable solved in the same direction of the flow with 5x5 mesh and $Pe = 20$

As it is depicted in figure 5.8, all 4 schemes give reasonable good results given the low resolution of the mesh used. QUICK and CDS schemes are the ones that have more accurate results, as they are second order schemes. SUDS scheme, which is also a second order scheme, gives slightly worse results than the other two schemes mentioned, and the UDS is the worst of all four in terms of accuracy.

However, as the Péclet number increases up to $Pe = 10, 25$, for the same mesh used, all 4 schemes start presenting bigger absolute errors. The most important thing to notice in figure 5.9 is that at $x = 1, 6$, the CDS gives a value of $\phi = -1.519$. This is an evidence of an unbounded scheme, which means that if the variable ϕ is a physically positive quantity, this undershoot or overshoot that may appear leads to physically impossible results.

Finally, for a Péclet number of $Pe = 20$, both the QUICK and CDS experience overshoots and undershoots, giving negative values at a certain point, which again leads to physically unrealisable results. The UDS stays bounded in all the condition above, however, the absolute error is important for this first order scheme.

Next, a study of the Péclet number in the solution is done.

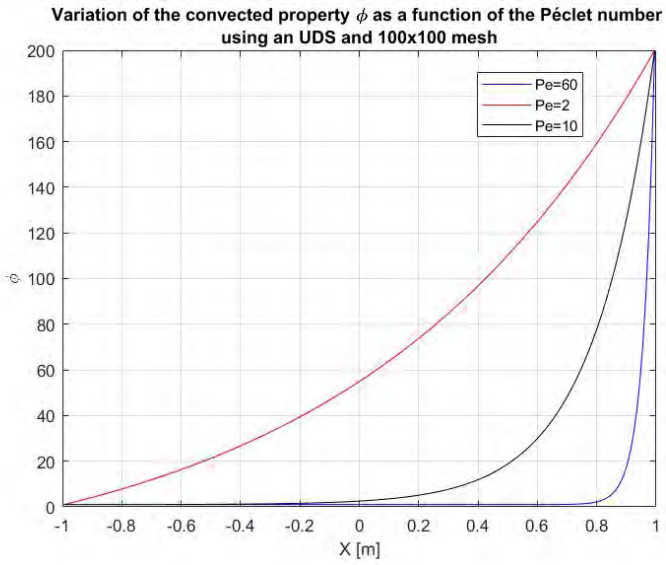

Figure 5.11: Unidimensional flow with an unidimensional variation of the variable solved in the same direction of the flow with 100x100 mesh and different Péclet numbers

As it is shown in figure 5.11, for low Péclet numbers, diffusive transport is important. Thus, the property of interest ϕ tends to spread uniformly inside the domain. However, as the Péclet number increases, convective transport is much more dominating, which means that the property ϕ tends to concentrate in the direction of the flow.

Finally, in order to make sure that the schemes are correctly implemented. A log-log plot of the cell size vs the absolute error is graphed in order to check the order of the overall scheme. Figure 5.12 shows the rate of convergence of the overall scheme for different convective schemes used. Clearly, using an UDS to obtain the value of ϕ at the cell faces, gives place to a first order scheme, even though the diffusion term is approximated using a second order approach. SUDS and CDS are second order schemes as seen below, as well as the QUICK scheme using a uniform mesh. Another important thing to notice is that from the same mesh size, the QUICK scheme is the one that gives the smaller error, followed by the CDS, the SUDS and

finally the UDS.

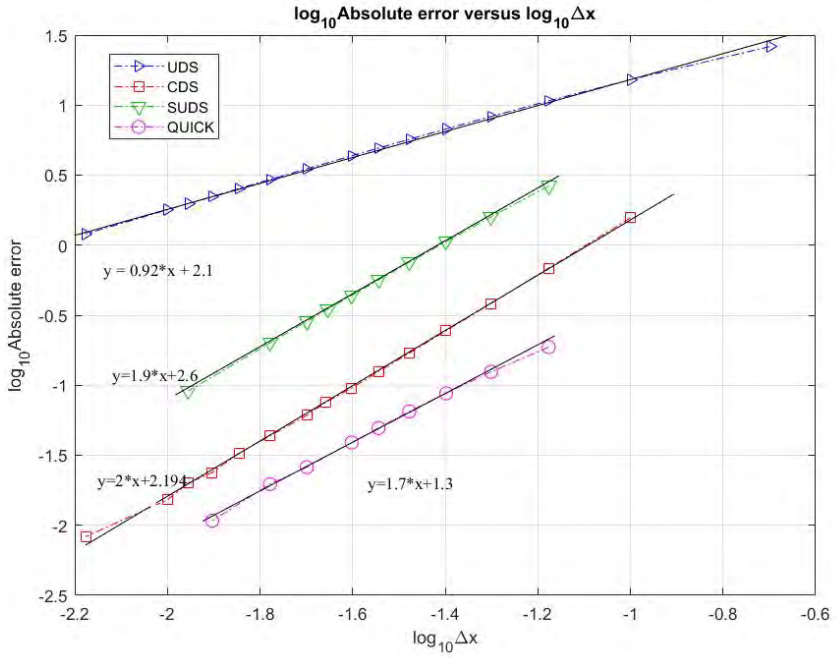

Figure 5.12: $log_{10}(\Delta_x)$ vs $log_{10}(Absolute\ error)$ for different convective schemes

5.4 Unidimensional flow with an unidimensional variation of the variable solved in the perpendicular direction of the flow

This problem is similar to the one presented in the section above. However, the only difference is the velocity field, which is expressed as it follows:

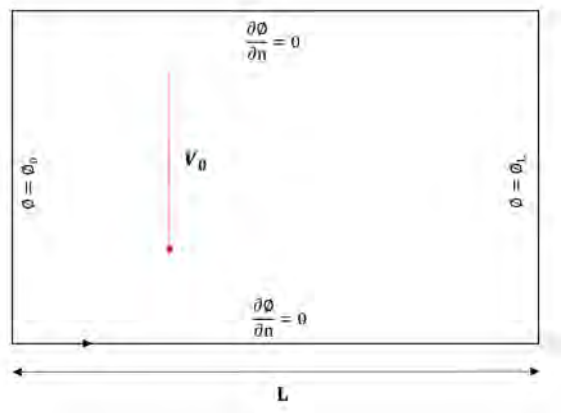

Figure 5.13: Unidimensional flow with an unidimensional variation of the variable solved in the perpendicular direction of the flow

$$u(x, y) = 0$$
$$v(x, y) = -V_0$$

The exact solution has the following form:

$$\phi = \phi_0 + \frac{\phi_L - \phi_0}{L} x \tag{5.4.1}$$

It is important to notice that neither does the exact solution depend on the flow field, nor it does on the Péclet number. Thus, the solution is only a straight line joining the values of the convected property at the left and right boundaries of the domain:

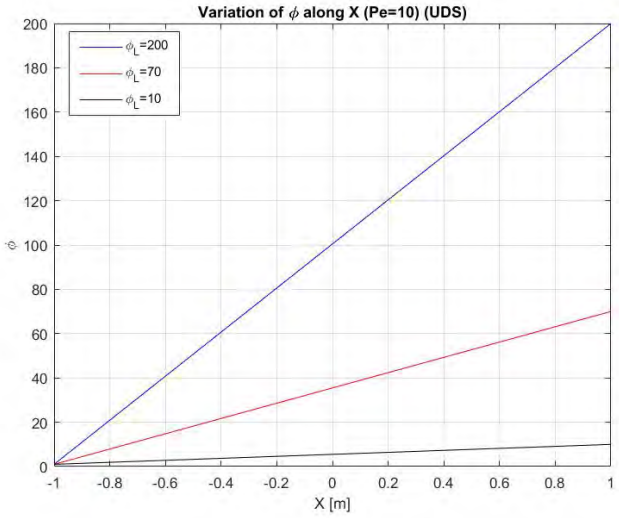

Figure 5.14: Unidimensional flow with an unidimensional variation of the variable solved in the perpendicular direction of the flow for ϕ_L=10, 70 & 200 and 100x100 mesh (UDS)

5.5 Diagonal Flow

For this third problem, the flow is in the main diagonal and an analytical solution exists for an infinite Péclet number.

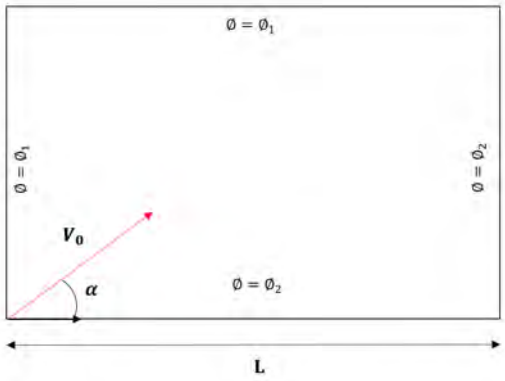

Figure 5.15: Diagonal flow

For a given velocity field:

$$u(x, y) = V_0 \cdot cos(\alpha)$$
$$v(x, y) = V_0 \cdot sin(\alpha)$$

If the Péclet number is $Pe = \infty$:

$$\phi = \phi_1 \quad above\ the\ diagonal \tag{5.5.1}$$
$$\phi = \phi_2 \quad below\ the\ diagonal$$

The solutions are graphed for different Péclet numbers:

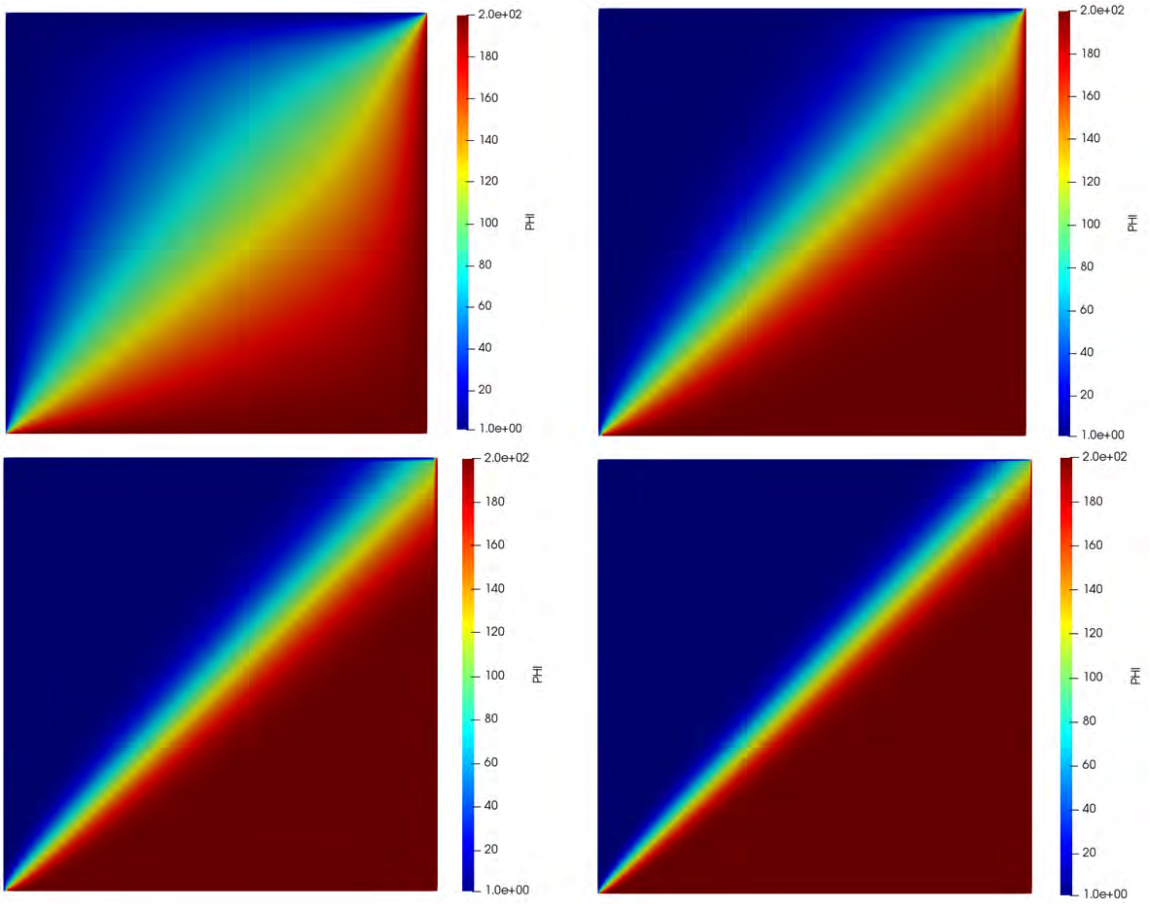

Figure 5.16: Diagonal flow for Pe=10 (top left), Pe=100 (top right), Pe=10000 (bottom left), Pe=1e30 (bottom right)

As it is shown in figure 5.16, for low Péclet numbers, transport by diffussion is quite important and thus, there is a smooth transition of the property ϕ between the top and left boundaries and the bottom and right boundaries of the volume. As the Péclet number increases and tends to infinity, there is less transport by diffusion and, due to the velocity flow, the results tend to the analytical solution.

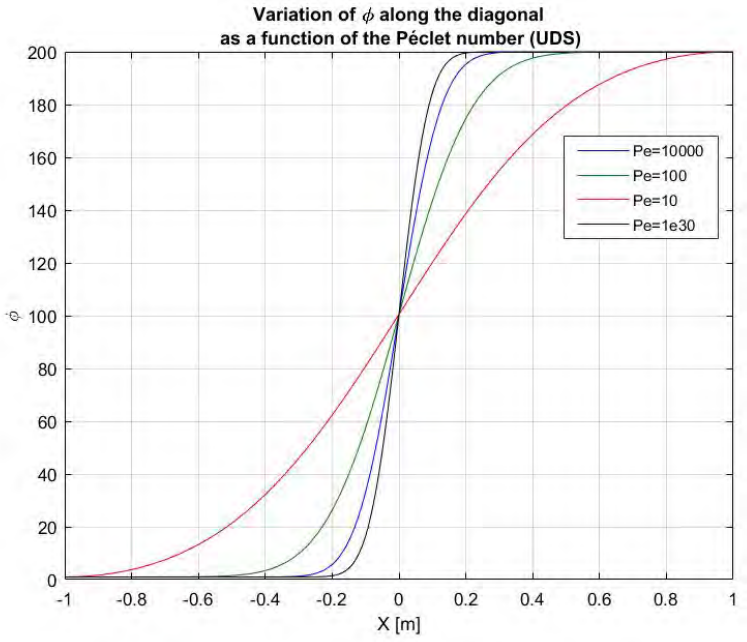

Figure 5.17: Diagonal flow results for different Péclet numbers with UDS and 100x100 mesh

However, it can be seen that for $Pe = 1e30$, there is still some transport of the property ϕ in the perpendicular direction of the flow (i.e diffusion). This is due to numerical diffusion: which means that the numerical schemes used to evaluate the variable ϕ at the interfaces between volumes are not exact and give a false diffusion, even though there should not be any. Higher order schemes, such as QUICK or CDS, give better performance and exhibit less numerical diffusion in the results than lower order schemes such as UDS, as it can be depicted in the graphs below:

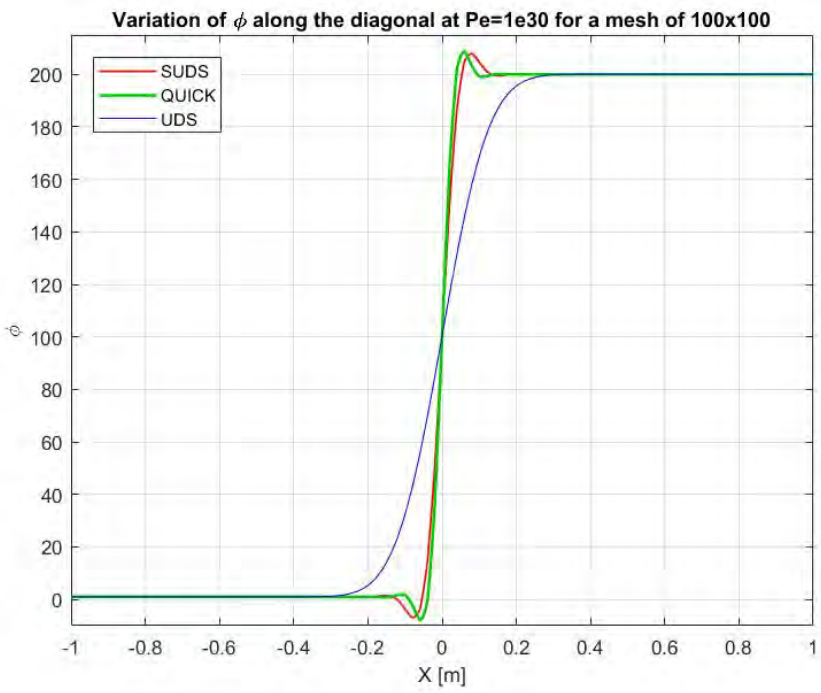

Figure 5.18: Diagonal flow results for a 100x100 mesh and Pe=1e30 using UDS, SUDS and QUICK

QUICK and SUDS convective schemes experience a lot less false diffusion compared to the UDS. However, as they are both unbounded schemes they experience important overshoots and undershoots before and after the diagonal. QUICK scheme is slightly less numerically diffusive than the SUDS, but it has slightly more important overshoots and undershoots. This is an important phenomenon and should be considered when interpreting results.

Another important thing to take into account is the size of the mesh. For coarser meshes, the false diffusion is also important, which means that using a higher order scheme might still give poor results if the mesh is not fine enough.

The graph below shows the results for a Péclet number of 1e30 and different mesh sizes. It is clear that as the mesh gets refined, there is less false diffusion on the results:

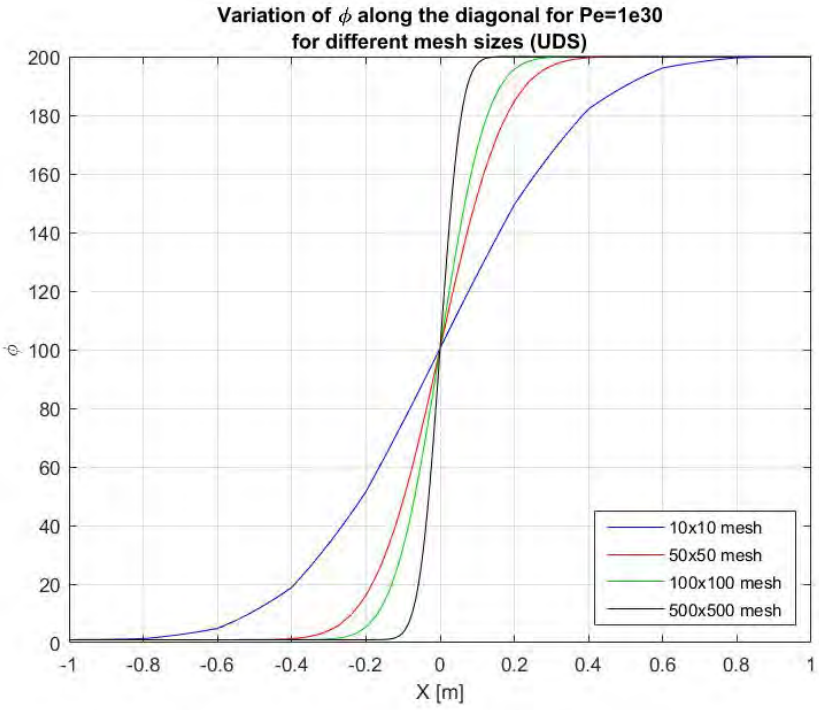

Figure 5.19: Diagonal flow results for Pe=1e30 (UDS) for different mesh sizes

5.6 Solenoidal Flow

The final benchmark problem to study in this section is the solenoidal flow, also known as the Smith-Hutton problem. The problem is described below:

In a rectangular domain with a velocity field:

$$u(x, y) = 2y(1 - x^2)$$
$$v(x, y) = -2x(1 - y^2)$$

With the following boundary conditions:

$$\phi = 1 + tanh[10(2x + 1)] \qquad -1 \leqslant x \leqslant 0 \quad y = 0$$

$$\phi = 1 - tanh[10] \quad x = -1 \quad 0 \leqslant y \leqslant 1$$
$$\phi = 1 - tanh[10] \quad -1 \leqslant x \leqslant 1 \quad y = 1$$
$$\phi = 1 - tanh[10] \quad x = 1 \quad 0 \leqslant y \leqslant 1$$
$$\frac{\partial \phi}{\partial y} = 0 \quad 0 \leqslant x \leqslant 1 \quad y = 0$$

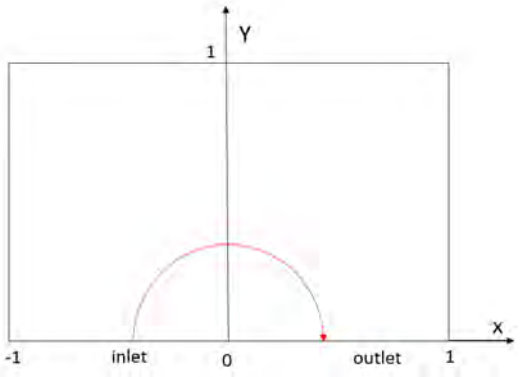

Figure 5.20: Solenoidal flow (Smith-Hutton problem)

Numerical results at the outlet for different values of ρ/Γ are shown in the following table:

Position x	$\boldsymbol{\rho/\Gamma = 10}$	$\boldsymbol{\rho/\Gamma = 10^3}$	$\boldsymbol{\rho/\Gamma = 10^6}$
0.0	1.989	2.000	2.000
0.1	1.402	1.9990	2.000
0.2	1.146	1.9997	2.000
0.3	0.946	1.9850	1.999
0.4	0.775	1.8410	1.964
0.5	0.621	0.9510	1.000
0.6	0.480	0.1540	0.036
0.7	0.349	0.0010	0.001
0.8	0.227	0.0000	0.000
0.9	0.111	0.0000	0.000
1.0	0.000	0.0000	0.000

Table 5.2: Benchmark results for the Smith-Hutton problem. Extracted from [4]

The results are graphed and compared with the benchmark solution in the following graph:

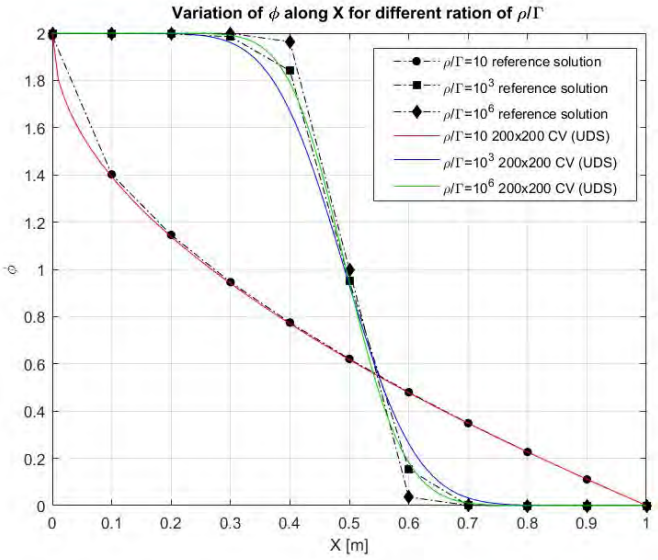

Figure 5.21: Diagonal flow (Smith-Hutton results for 200x200 mesh and UDS)

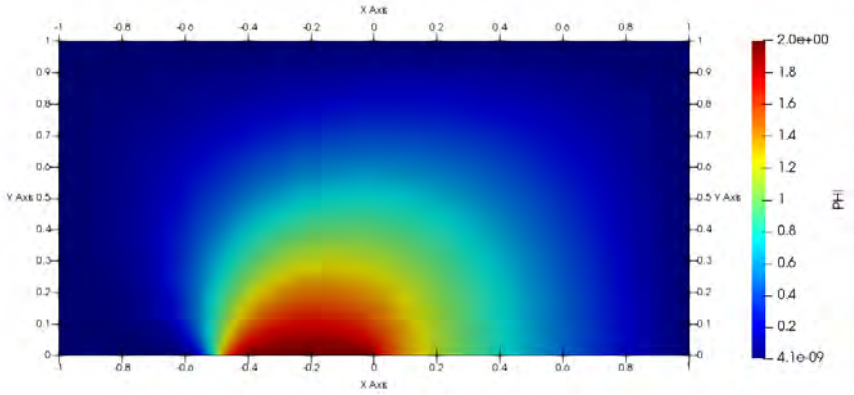

Figure 5.22: Solenoidal flow (Smith-Hutton results for $\rho/\Gamma = 10$)

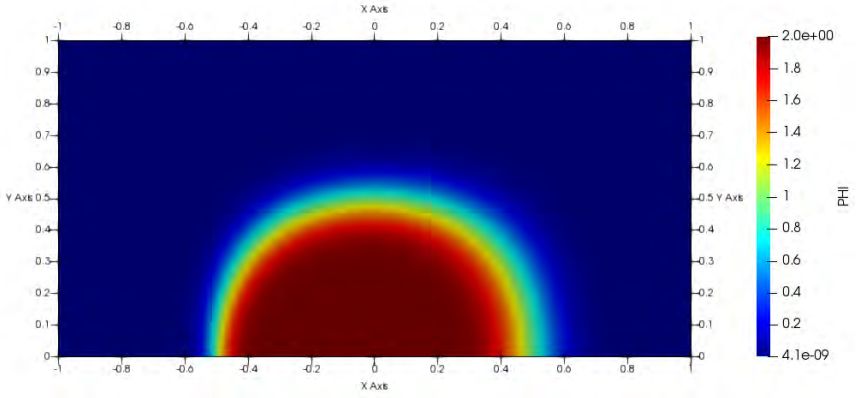

Figure 5.23: Solenoidal flow (Smith-Hutton results forfor $\rho/\Gamma = 10^3$)

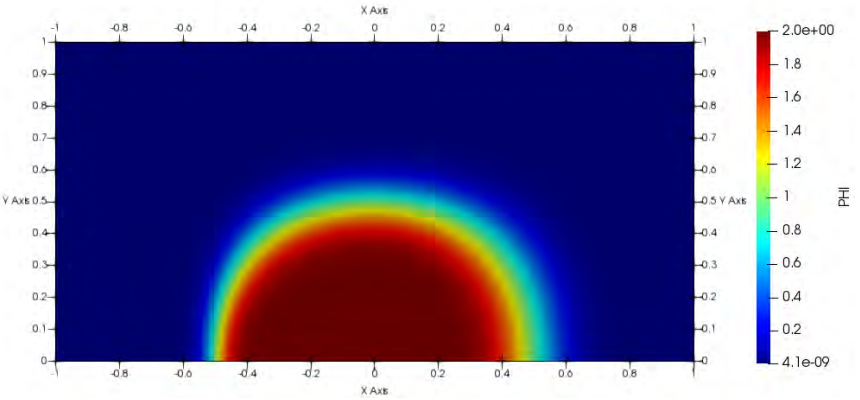

Figure 5.24: Solenoidal flow (Smith-Hutton results for for $\rho/\Gamma = 10^6$)

5.7 Conclusions

In this chapter, excellent agreement has been observed between the simulated and benchmark results. Different convective schemes have been studied and its advantages and drawbacks have been observed. The UDS scheme proved to be really stable and bounded in all the conditions tested. However, being a first order scheme, the accuracy of its results is worse than the one with higher order schemes. Moreover, numerical diffusion is important with this scheme and needs to be considered when interpreting results. On the

other hand, QUICK and CDS proved to be better in terms of accuracy (being QUICK slightly better than CDS) than the UDS. However, both schemes are unbounded and with certain Péclet numbers they can experience important overshoots and undershoots. On the other hand, they present a lot less numerical diffusion. The SUDS scheme lies between the UDS and the other two schemes in terms of accuracy and numerical diffusion.

Chapter 6

Incompressible Navier-Stokes equations: Fractional step method approach

6.1 Introduction

This chapter is dedicated to the solution of the 2D incompressible Navier-Stokes equations. The Fractional step method is used to solve them, making emphasis in the mathematical formulation and the algorithm used for their solution. Finally, the results are verified with the Lid-driven cavity problem.

6.2 Mathematical background: The Helmholtz-Hodge theorem

The basis of the approach applied in this thesis to solve the incompressible Navier-Stokes equations is the Helmholtz-Hodge theorem:

Theorem: *Given a vector field* $\boldsymbol{\omega}$ *defined in a bounded domain* $\Omega \subseteq R^n$ *for* $n = 2, 3$*, with a smooth boundary* $\partial\Omega$*, the vector field can be uniquely decomposed in the following form:*

$$\boldsymbol{\omega} = \mathbf{u} + \nabla\varphi \tag{6.2.1}$$

Where:

ϕ is a scalar field over Ω and $\mathbf{u}$ is a vector field of Ω that satisfies:

- $\nabla \cdot \mathbf{u} = 0$
- $\mathbf{u} \cdot \mathbf{n} = 0$ over $\partial\Omega$

Proof:

The divergence of the product of the vector field and the scalar field can be decomposed as:

$$\nabla \cdot (\mathbf{u}\varphi) = (\nabla \cdot \mathbf{u})\varphi + \mathbf{u} \cdot (\nabla\varphi)$$

Considering that the vector field is divergence-free:

$$\nabla \cdot (\mathbf{u}\varphi) = \mathbf{u} \cdot (\nabla\varphi)$$

Calculating the scalar product between $\mathbf{u}$ and $\nabla\varphi$ in the region Ω, and applying the divergence theorem:

$$\int_\Omega \nabla\varphi \cdot \mathbf{u}\ \mathbf{d\Omega} = \int_\Omega \nabla \cdot (\varphi\mathbf{u})\ \mathbf{d\Omega} = \int_{\partial\Omega} (\varphi\mathbf{u}) \cdot \mathbf{n} dS = 0$$

Which is equal to 0 because the fluxes through the boundary of the domain are 0, as stated previously. As a consequence of this statement, the orthogonality between the vector field $\mathbf{u}$ and $\nabla\varphi$ is proved.

To prove the unicity of the decomposition, two different decompositions are assumed:

$$\boldsymbol{\omega} = \mathbf{u_1} + \nabla\varphi_1 = \mathbf{u_2} + \nabla\varphi_2$$

Rearranging terms:

$$\mathbf{u_1} - \mathbf{u_2} + \nabla(\varphi_1 - \varphi_2) = 0 \tag{6.2.2}$$

The scalar product of the previous expression and $(\mathbf{u_1} - \mathbf{u_2})$, can be expressed as:

$$\int_\Omega \left[||\mathbf{u_1} - \mathbf{u_2}||^2 + (\mathbf{u_1} - \mathbf{u_2}) \cdot \nabla(\varphi_1 - \varphi_2)\right] \mathbf{d\Omega} = 0$$

Applying (6.2.2) to the previous expression:

$$\int_\Omega ||\mathbf{u_1} - \mathbf{u_2}||^2 \mathbf{d\Omega} = 0$$

From which it is clear that:

$$\mathbf{u_1} = \mathbf{u_2}$$
$$\nabla\varphi_1 = \nabla\varphi_2 \rightarrow \varphi_1 = \varphi_2 + const.$$

Which proves that the decomposition is unique. The unique decomposition of the vector field is shown in the figure below:

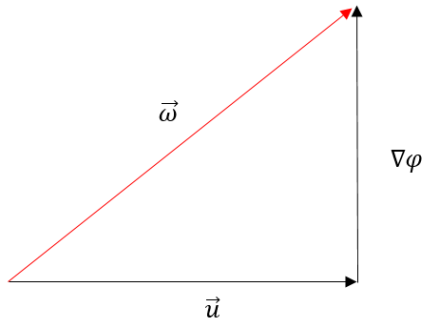

Figure 6.1: Helmholtz-Hodge theorem

6.3 Mathematical formulation

As it has already been said, the Fractional Step method is used to solve the incompressible Navier-Stokes equations, using the Helmholtz-Hodge theorem explained previously.

The Navier-Stokes equations (mass and momentum) for incompressible and constant viscosity, and applying Newton's viscosity law, can be written as:

$$\nabla \cdot \mathbf{v} = \mathbf{0} \tag{6.3.1}$$

$$\rho \frac{\partial \mathbf{v}}{\partial t} + (\rho \mathbf{v} \cdot \nabla)\mathbf{v} = -\nabla p + \mu \Delta \mathbf{v} \tag{6.3.2}$$

Equation (6.3.2) can also be expressed as:

$$\rho \frac{\partial \mathbf{v}}{\partial t} = \mathbf{R}(\mathbf{v}) - \nabla p \tag{6.3.3}$$

Where:

$$\mathbf{R}(\mathbf{v}) = -(\rho \mathbf{v} \cdot \nabla)\mathbf{v} + \mu \Delta \mathbf{v} \tag{6.3.4}$$

Where $\mathbf{R}(\mathbf{v})$ stands for the convective and diffusive terms.

Integrating implicitly over time the continuity equation:

$$\nabla \cdot \mathbf{v}^{n+1} = \mathbf{0} \tag{6.3.5}$$

The time derivative term of the momentum equation is discretized using a second order central difference scheme:

$$\left.\frac{\partial \mathbf{v}}{\partial t}\right|^{n+1/2} \approx \frac{\mathbf{v}^{n+1} - \mathbf{v}^{n}}{\Delta t} + O(\Delta t^2) \tag{6.3.6}$$

While for the $\mathbf{R}(\mathbf{v})$, term a Second-order Adams-Bashforth scheme is used:

$$\mathbf{R}^{n+1/2}(\mathbf{v}) \approx 3/2\mathbf{R}(\mathbf{v^n}) - 1/2\mathbf{R}(\mathbf{v^{n-1}}) + O(\Delta t^2, \Delta x^m) \tag{6.3.7}$$

And finally, the pressure gradient term is calculated using a first-order backward Euler scheme.

Due to the Helmholtz-Hodge theorem demonstrated above, there is a unique decomposition that can be expressed as:

$$\mathbf{v}^p = \mathbf{v}^{n+1} + \frac{\Delta t}{\rho}\nabla p^{n+1} \tag{6.3.8}$$

Which can be used to rewrite the momentum equation to the projection momentum equation:

$$\rho\frac{\mathbf{v}^p - \mathbf{v}^n}{\Delta t} = 3/2\mathbf{R}(\mathbf{v^n}) - 1/2\mathbf{R}(\mathbf{v^{n-1}}) \tag{6.3.9}$$

Applying the divergence operator to each side of equation (6.3.8):

$$\nabla \cdot \mathbf{v}^{n+1} = \nabla \cdot \mathbf{v}^p - \nabla \cdot (\frac{\Delta t}{\rho}\nabla p^{n+1}) \tag{6.3.10}$$

And due to the continuity equation, a Poisson equation for the pressure can be derived:

$$\Delta p^{n+1} = \frac{\rho}{\Delta t}\nabla \cdot \mathbf{v}^p \tag{6.3.11}$$

And finally, the velocity at instant n+1 can be calculated using the original decomposition (6.3.8).

6.4 The checkerboard problem

Considering equation (6.3.8) for 1D spatial discretization, applying finite differences at node P, the velocity at the time step n+1 can be computed as follows:

$$u^{n+1} = u^p - \frac{\Delta t}{\rho}\left(\frac{P_E^{n+1} - P_W^{n+1}}{2\Delta x}\right) \tag{6.4.1}$$

From the expression above, it is seen that the velocity at the node is calculated from the pressure of the adjacent nodes, which means that converged velocity fields can be obtained with an nonphysical pressure map:

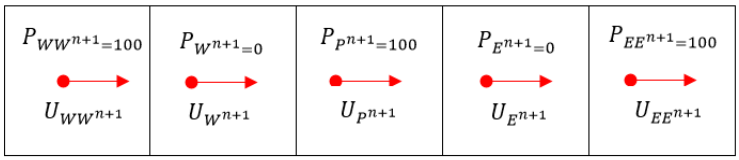

Figure 6.2: Checkerboard problem

It is clear that the pressure map of the figure above is nonphysical. However, since the velocity is calculated using the pressure from adjacent nodes, a velocity field will be obtained that will verify $\nabla P = 0$, which is far from real.

6.5 Staggered meshes approach

To solve this problem, the concept of staggered mesh is used. A main mesh is used to calculate the pressure at its nodes. A staggered mesh in the x direction is also computed, whose nodes are placed at the vertical cell faces of the main mesh. Finally, another staggered mesh in the y direction is used, placing its nodes at the horizontal cell faces of the main mesh.

Figure 6.3 shows how both meshes are distributed from the main mesh. It can be seen that with this approach, velocities both in x and y direction

are calculated with the pressure values of the main node, and thus, the checkerboard problem is solved. Horizontal velocities are calculated using the staggered mesh in the x direction, while vertical velocities are computed with the staggered mesh in the y direction.

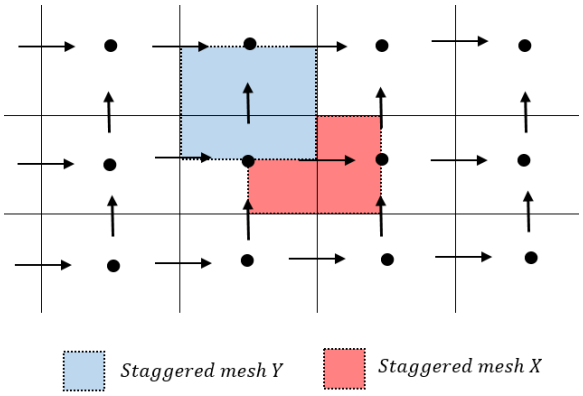

Figure 6.3: Staggered meshes approach to solve the checkerboard problem

It is clear that this method allows to avoid an important problem, however, the way in which the mass flows are computed at each face needs to be reconsidered in the following way.

For the staggered mesh in x direction:

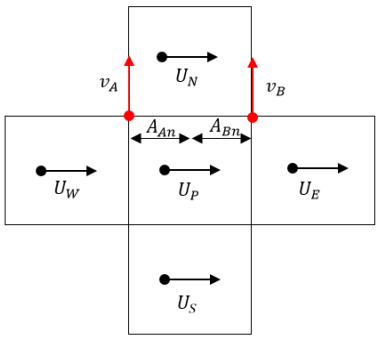

Figure 6.4: Mass flow for the mesh staggered in x direction

$$\dot{m}_e = (\rho u A)_e = \frac{(\rho u)_E + (\rho u)_P}{2} A_e \tag{6.5.1}$$

$$\dot{m}_n = (\rho v A)_n = (\rho v)_A A_{An} + (\rho v)_B A_{BN} \tag{6.5.2}$$

While for the staggered mesh in the y direction:

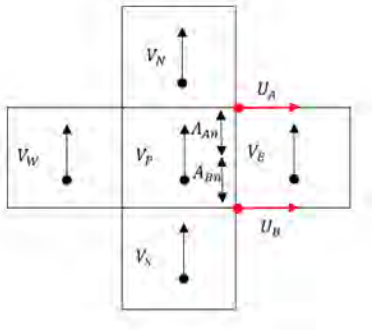

Figure 6.5: Mass flow for the mesh staggered in y direction

$$\dot{m}_e = (\rho u A)_e = (\rho u)_A A_{An} + (\rho u)_B A_{BN} \tag{6.5.3}$$

$$\dot{m}_n = (\rho v A)_n = \frac{(\rho v)_N + (\rho v)_P}{2} A_n \tag{6.5.4}$$

6.6 Equations discretization

The final step, before presenting the algorithm to solve the problem, is to discretize the equations. Integrating equation (6.3.4) over the control volume in the staggered x mesh:

$$\int_{\Omega_x} R(u) d\Omega_x = -\int_{\Omega_x} (\rho \mathbf{v} \cdot \nabla) u d\Omega_x + \int_{\Omega_x} \mu \Delta u d\Omega_x \tag{6.6.1}$$

And applying the divergence theorem:

$$\int_{\Omega_x} R(u) d\Omega_x = -\int_{\partial\Omega_x} (\rho \mathbf{v}) u \cdot \mathbf{n} dS + \int_{\partial\Omega_x} \mu \nabla u \cdot \mathbf{n} dS \tag{6.6.2}$$

Using a second order approximation for the gradient of the velocity, the x component of equation (6.3.4) gets discretized in the following way:

$$R(u)\Omega_{xP} \approx -[(\dot{m}_e u_e - \dot{m}_w u_w + \dot{m}_n u_n - \dot{m}_s u_s] + [\mu_e \frac{u_E - u_P}{d_{EP}} A_e - \mu_w \frac{u_P - u_W}{d_{WP}} A_w + \mu_n \frac{u_N - u_P}{d_{NP}} A_n - \mu_s \frac{u_P - u_S}{d_{SP}} A_s] \tag{6.6.3}$$

Where the values u_e, u_w, u_n, u_s can be computed using any convective scheme presented in the previous chapter (QUICK, SMART, CDS,...).

And the same can be done for the vertical component of the velocity on the mesh staggered in the y direcion:

$$R(v)\Omega_{yP} \approx -[(\dot{m}_e v_e - \dot{m}_w v_w + \dot{m}_n v_n - \dot{m}_s v_s] + [\mu_e \frac{v_E - v_P}{d_{EP}} A_e - \mu_w \frac{v_P - v_W}{d_{WP}} A_w + \mu_n \frac{v_N - v_P}{d_{NP}} A_n - \mu_s \frac{v_P - v_S}{d_{SP}} A_s] \tag{6.6.4}$$

Where the values v_e, v_w, v_n, v_s can be computed using any convective scheme presented in the previous chapter (QUICK, SMART, CDS,...).

Equation (6.3.11) can also be discretized applying the divergence theorem. The final discretized equations takes this form:

$$\frac{P_E^{n+1} - P_P^{n+1}}{d_{EP}} A_e - \frac{P_P^{n+1} - P_W^{n+1}}{d_{WP}} A_w + \frac{P_N^{n+1} - P_P^{n+1}}{d_{NP}} A_n - \frac{P_P^{n+1} - P_S^{n+1}}{d_{SP}} A_s = \frac{1}{\Delta t}[(\rho u^P)_e A_e - (\rho u^P)_w A_w + (\rho v^P)_n A_n - (\rho v^P)_s A_s] \tag{6.6.5}$$

Finally, equation (6.3.8) can be discretized for both x and y component as:

$$u_P^{n+1} = u_P^P - \frac{\Delta t}{\rho} \frac{p_B^{n+1} - p_A^{n+1}}{d_{BA}} \tag{6.6.6}$$

$$v_P^{n+1} = v_P^P - \frac{\Delta t}{\rho} \frac{p_B^{n+1} - p_A^{n+1}}{d_{BA}} \tag{6.6.7}$$

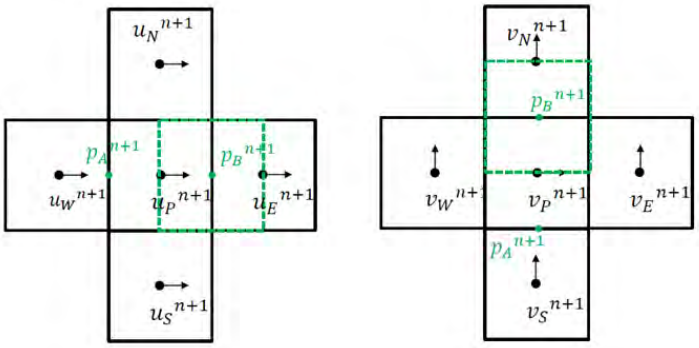

Figure 6.6: Velocity calculation (u (left) and v (right)) from pressure field [2]

One last thing to take into account is the right time-step used for the discretized equations.The Courant-Friedrichs-Lewy condition [17] is a condition for numerical stability that states that during a certain time-step, the information should only travel to adjacent nodes.

$$\Delta t_c = min\left(0.35 \frac{\Delta x}{|v|}\right) \tag{6.6.8}$$

$$\Delta t_d = min\left(0.20 \frac{\rho \Delta x^2}{\mu}\right) \tag{6.6.9}$$

$$\Delta t = min\left(\Delta t_c, \Delta t_d\right) \tag{6.6.10}$$

Where the convective and diffusive transport are both considered to ensure stability.

6.7 Boundary conditions

Finally, before presenting the final algorithm, the boundary conditions are considered:

- **Wall boundary condition**

  Since a boundary layer is created at the wall, the gradient of the pressure in the normal direction of the wall is 0.

$$\frac{\partial p}{\partial n} = 0 \tag{6.7.1}$$

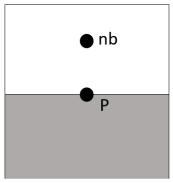

Figure 6.7: Pressure boundary condition at the wall

- **Prescribed velocity**

  From equation (6.3.8), if v_P^{n+1} is known, the relationship $v^P = v_P^{n+1}$ can be set and thus: $\frac{\partial p}{\partial n} = 0$

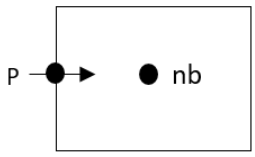

Figure 6.8: Prescribed velocity boundary condition

Finally, the general algorithm to solve the incompressible Navier-Stokes equation using the Fractional Step method is presented in the following page:

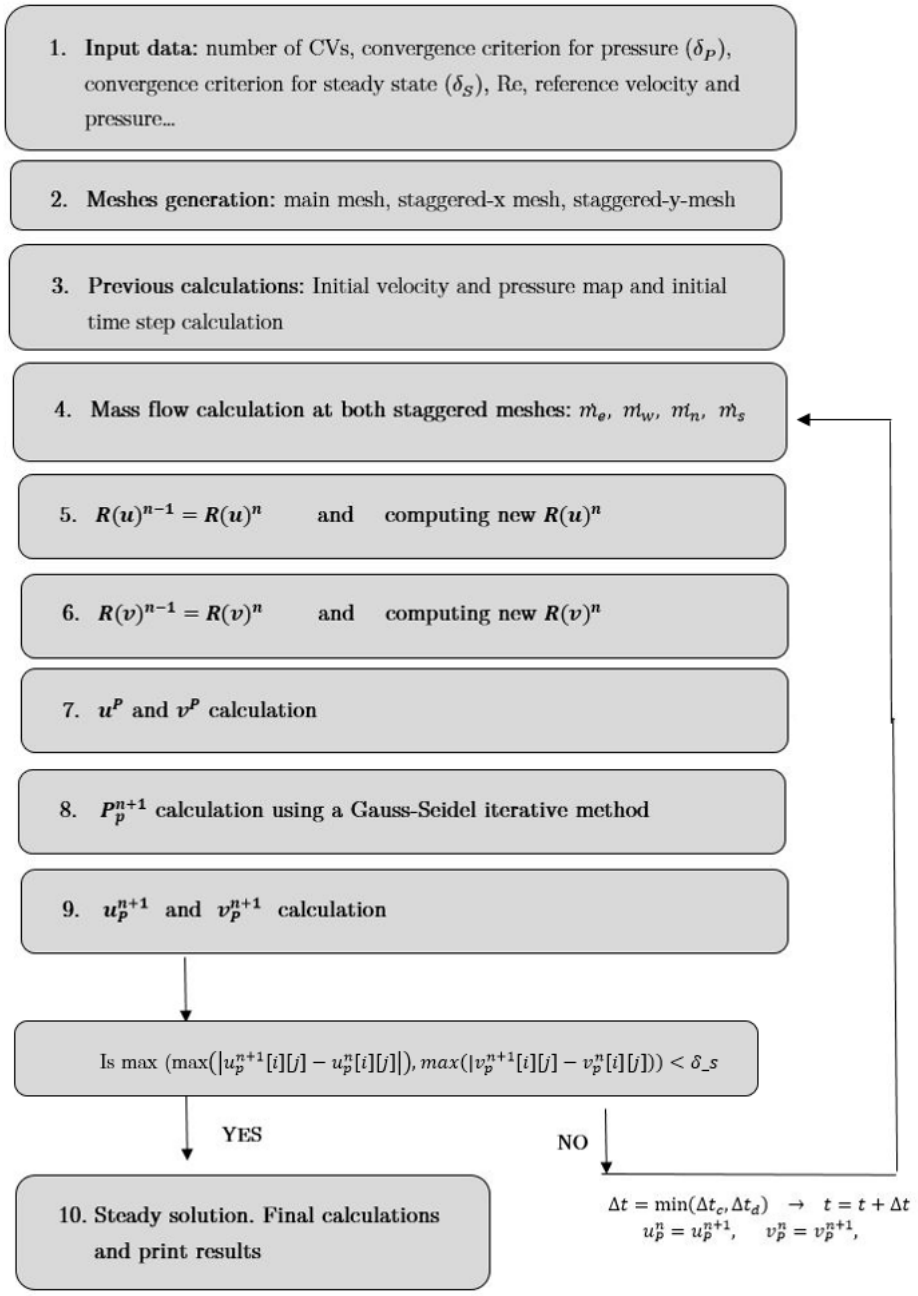

Figure 6.9: Algorithm for the incompressible Navier-Stokes equations using the Fractional Step method

6.8 Lid-driven cavity problem

The lid-driven cavity prblem is a well-known benchmark problem for viscous incompressible flow. The problem consists of a square cavity with fixed walls with no-slip condition on the left, right and bottom sides and a lid that moves with a known tangential velocity on the top part of the box.

The problem and its boundary conditions are represented in the following figure:

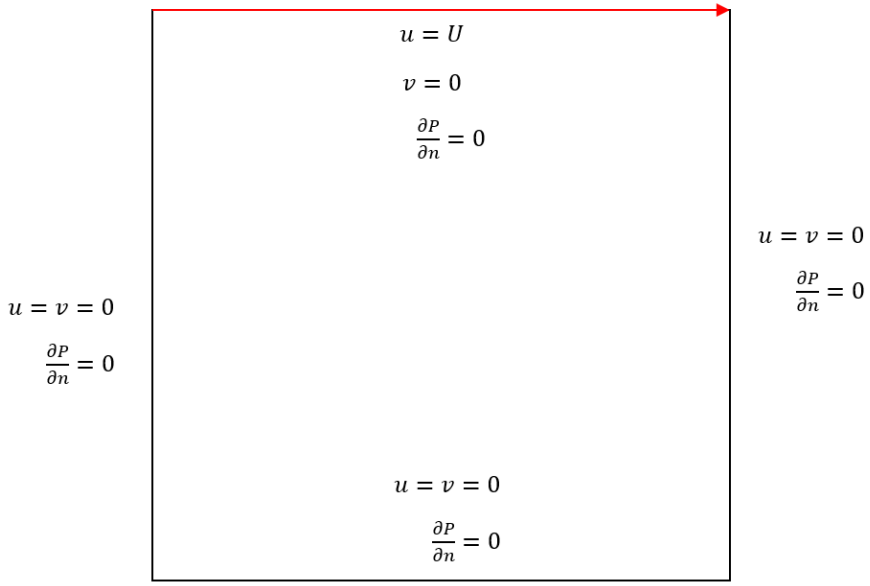

Figure 6.10: Lid-driven cavity problem

The behaviour of the results depends on the Reynolds number, which is defined as $Re = \frac{\rho UL}{\mu}$, where U is the tangential velocity of the top lid and L is the width of the cavity.

Benchmark results are represented in the following table for the horizontal and vertical velocity components in both center lines of the cavity, and compared with the results obtined using Upwind and SMART convective schemes.

y	$Re = 100$	$Re = 400$	$Re = 1000$	$Re = 3200$	$Re = 5000$
1,0000	1,00000	1,00000	1,00000	1,00000	1,00000
0,9766	0,84123	0,75837	0,65928	0,53236	0,48223
0,9688	0,78871	0,68439	0,57492	0,48296	0,46120
0,9609	0,73722	0,61756	0,51117	0,46547	0,45992
0,9531	0,68717	0,55892	0,46604	0,46101	0,46036
0,8516	0,23151	0,29093	0,33304	0,34682	0,33556
0,7344	0,00332	0,16256	0,18719	0,19791	0,20087
0,6172	-0,13641	0,02135	0,05702	0,07156	0,08183
0,5000	-0,20581	-0,11477	-0,06080	-0,04272	-0,03039
0,4531	-0,21090	-0,17119	-0,10648	-0,86636	-0,07404
0,2813	-0,15662	-0,32726	-0,27805	-0,24427	-0,22855
0,1719	-0,10150	-0,24299	-0,38289	-0,34323	-0,33050
0,1016	-0,06434	-0,14612	-0,29730	-0,41933	-0,40435
0,0703	-0,04775	-0,10338	-0,22220	-0,37827	-0,43643
0,0625	-0,04192	-0,09266	-0,20196	-0,35344	-0,42901
0,0547	-0,03717	-0,08186	-0,18109	-0,32407	-0,41165
0,0000	0,00000	0,0000	0,00000	0,00000	0,00000

Table 6.1: Lid-driven cavity benchmark results. u in the vertical center line. Extracted from [2]

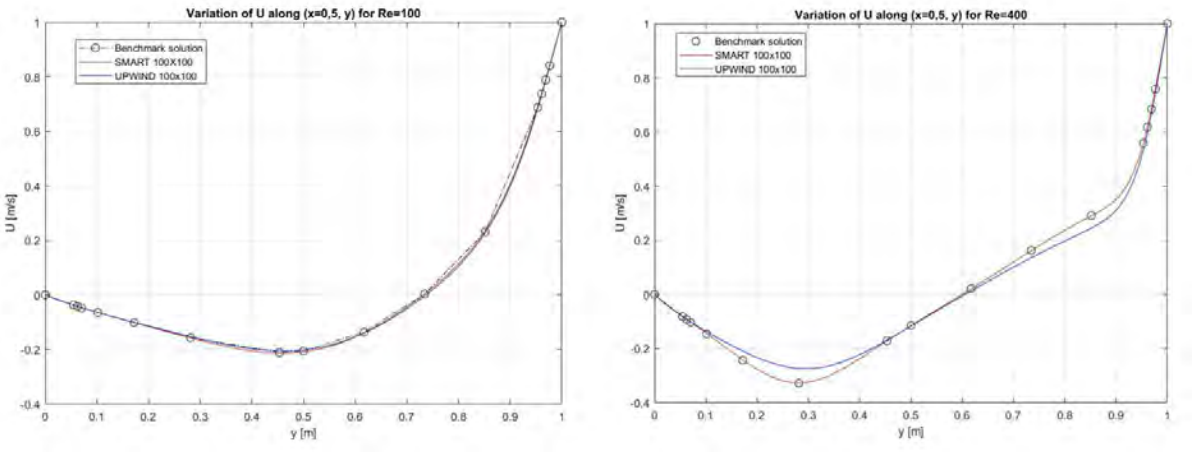

Figure 6.11: Lid-driven cavity horizontal velocity in the vertical centerline of the cavity for $Re = 100$ (left) and $Re = 400$ (right), compared with benchmark solutions.

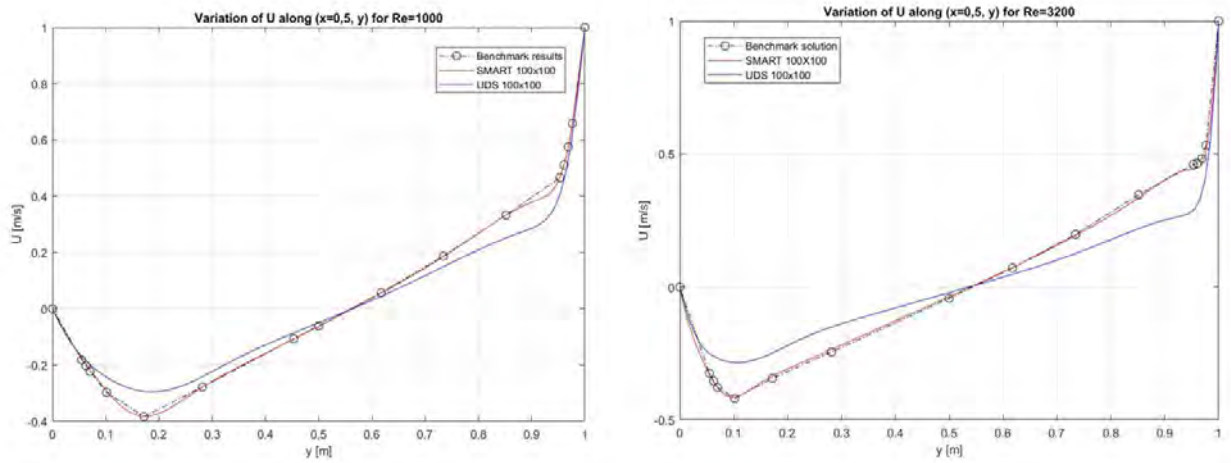

Figure 6.12: Lid-driven cavity horizontal velocity in the vertical centerline of the cavity for $Re = 1000$ (left) and $Re = 3200$ (right), compared with benchmark solutions

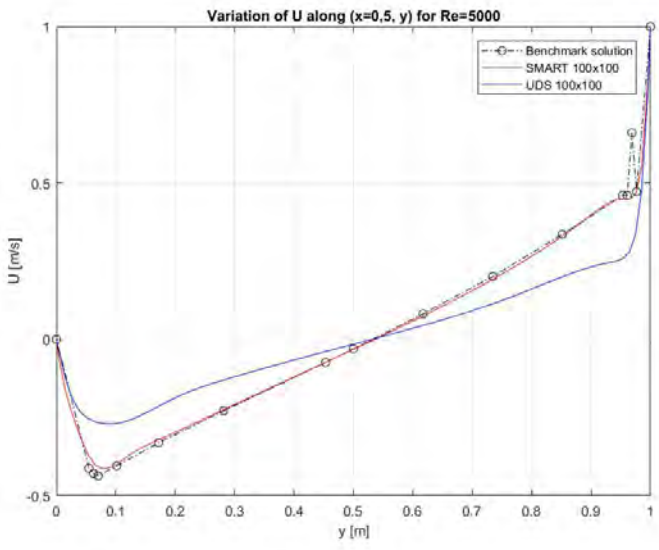

Figure 6.13: Lid-driven cavity horizontal velocity in the vertical centerline of the cavity for $Re = 5000$, compared with benchmark solution

x	$Re = 100$	$Re = 400$	$Re = 1000$	$Re = 3200$	$Re = 5000$
1,0000	0,00000	0,00000	0,00000	0,00000	0,00000
0,9688	-0,05906	-0,12146	-0,21388	-0,39017	-0,49774
0,9609	-0,07391	-0,15663	-0,27669	-0,47425	-0,55069
0,9531	-0,08864	-0,19254	-0,33714	-0,52357	-0,55408
0,9453	-0,10313	-0,22847	-0,39188	-0,54053	-0,52876
0,9063	-0,16914	-0,23827	-0,51550	-0,44307	-0,41442
0,8594	-0,22445	-0,44993	-0,42665	-0,37401	-0,36214
0,8047	-0,24533	-0,38598	-0,31966	-0,31184	-0,30018
0,5000	0,05454	0,05186	0,02526	0,00999	0,00945
0,2344	0,17527	0,30174	0,32235	0,28188	0,27280
0,2266	0,17507	0,30203	0,33075	0,29030	0,28066
0,1563	0,16077	0,28124	0,37095	0,37119	0,35368
0,0938	0,12317	0,22965	0,32627	0,42768	0,42951
0,0781	0,10890	0,20920	0,30353	0,41906	0,43648
0,0703	0,10091	0,19713	0,29012	0,40917	0,43329
0,0625	0,09233	0,18360	0,27485	0,39560	0,42447
0,000	0,00000	0,0000	0,00000	0,00000	0,00000

Table 6.2: Lid-driven cavity benchmark results. v in the horizontal center line. Extracted from [2]

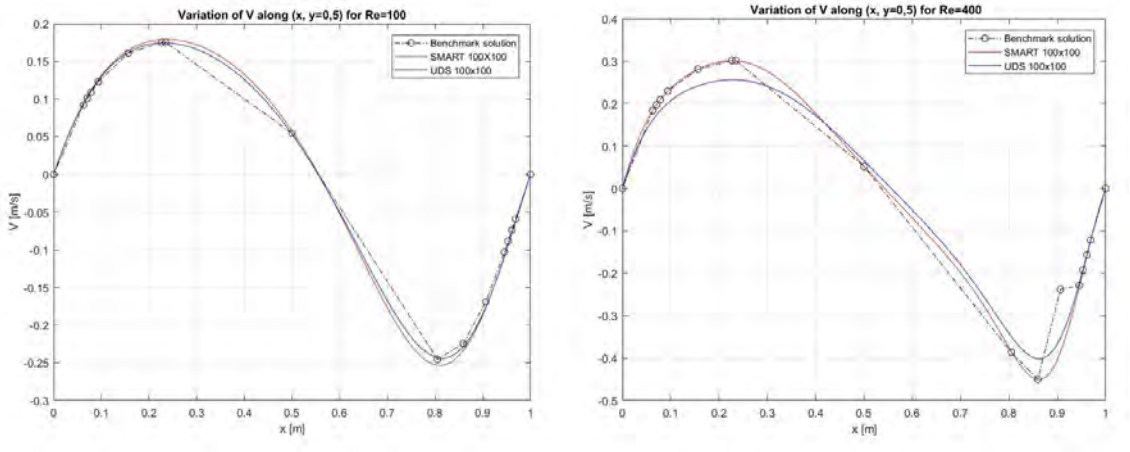

Figure 6.14: Lid-driven cavity vertical velocity in the horizontal centerline of the cavity for $Re = 100$ (left) and $Re = 400$ (right), compared with benchmark solutions.

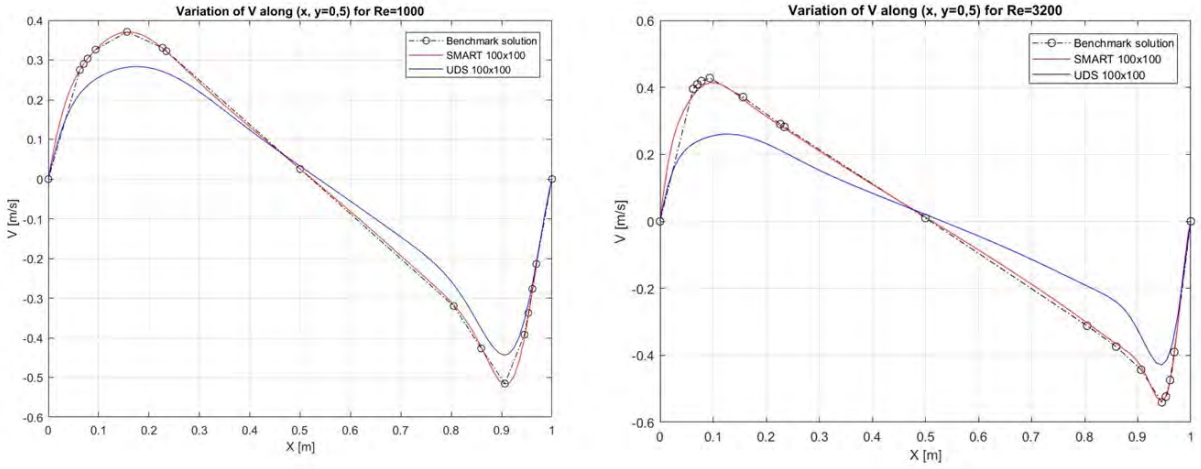

Figure 6.15: Lid-driven cavity vertical velocity in the horizontal centerline of the cavity for $Re = 1000$ (left) and $Re = 3200$ (right), compared with benchmark solutions

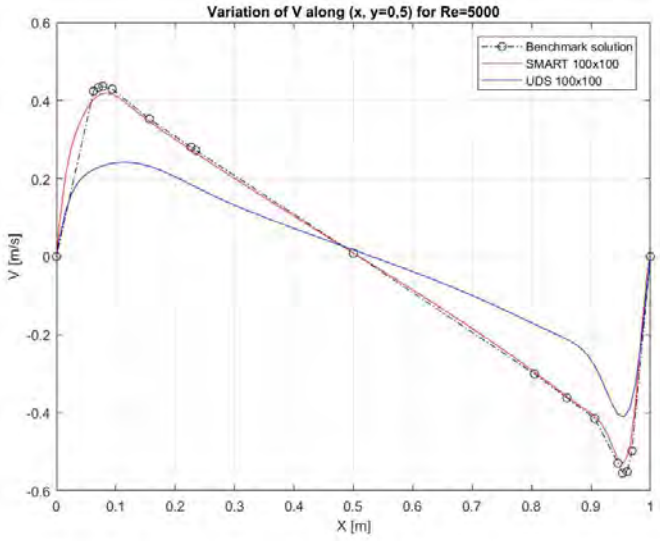

Figure 6.16: Lid-driven cavity vertical velocity in the horizontal centerline of the cavity for $Re = 5000$ compared with benchmark solution

From the figures above, it is clear that the results using the SMART convective scheme are very accurate for all the Reynolds numbers tested. However, UDS works only fine for a Reynolds number lower than 100 and then starts to exhibit really large errors. Nevertheless, both schemes increase their respective errors as the Reynolds number increases, as it gets closer to turbulent flow. With the UDS convective scheme, the error is: 25,61 times the error with SMART at $Re = 400$, 31,64 times the error with SMART at $Re = 1000$, 9,41 times the error with SMART at $Re = 3200$ and 4,69 times the error with SMART at $Re = 5000$. Figure 6.17 shows the absolute error as a function of the Reynolds number.

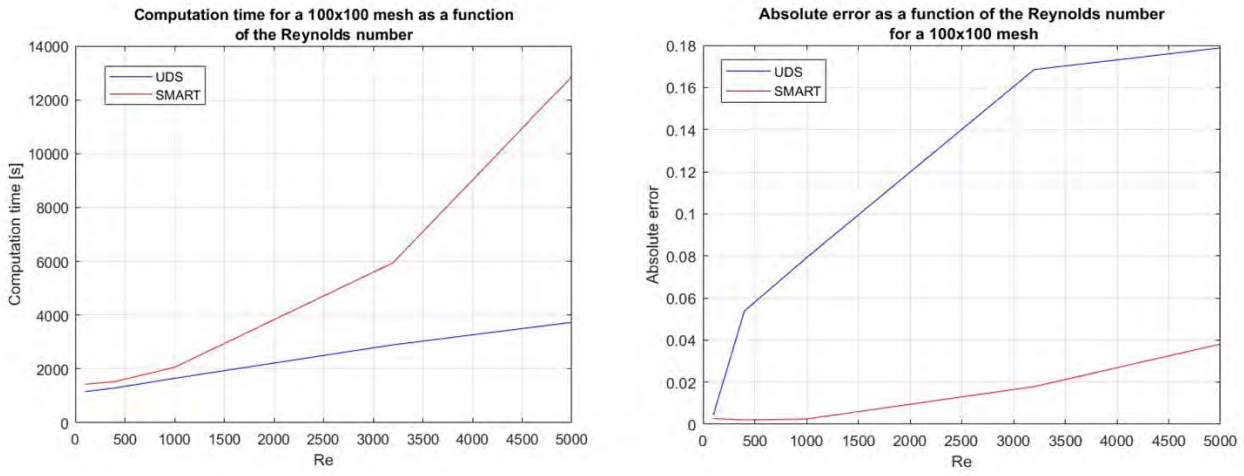

Figure 6.17: Absolute error and computation time as a function of the Reynolds number for the UDS and SMART convective schemes

On the other hand, figure 6.17 also shows the computation time as a function of the Reynolds number for the same schemes. While the computation time with the UDS increases nearly linearly, the computation time with the SMART scheme increases a lot faster (nearly exponentially). The computation time with the SMART scheme is: 3,44 times the computation time with the UDS scheme at $Re = 5000$, 2,052 time the computation time with UDS at $Re = 3200$, 1,247 times the computation time with UDS at $Re = 1000$, 1,1839 times the computation time with UDS at $Re = 400$, and 1,2389 times the computation time with UDS at $Re = 100$.

The colormaps and isolines of the velocity modulus at each Reynolds

numbers are now presented:

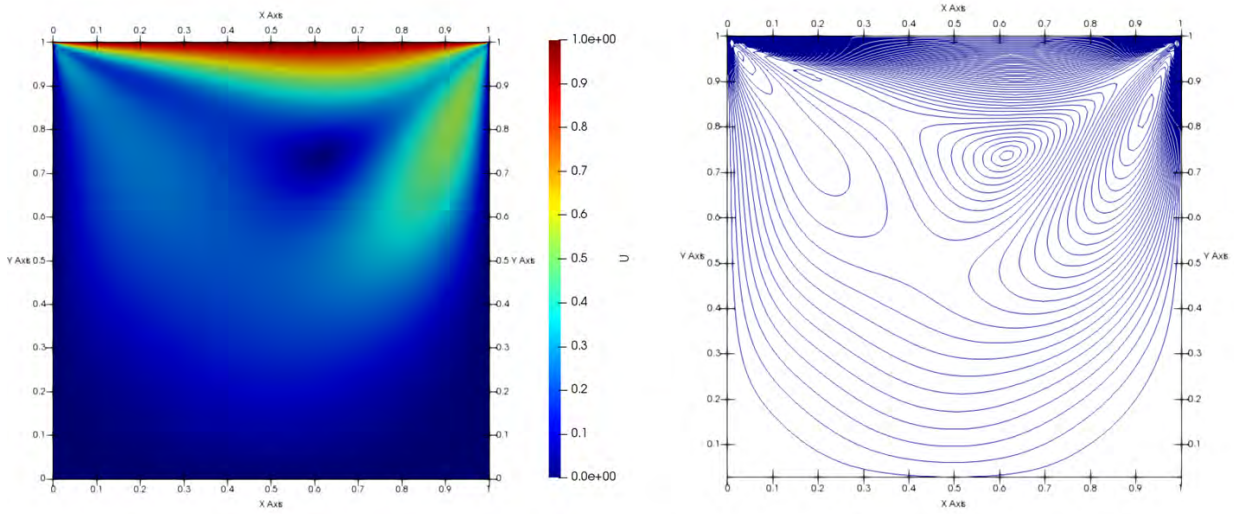

Figure 6.18: Lid-driven cavity velocity modulus and isolines of the velocity for $Re = 100$

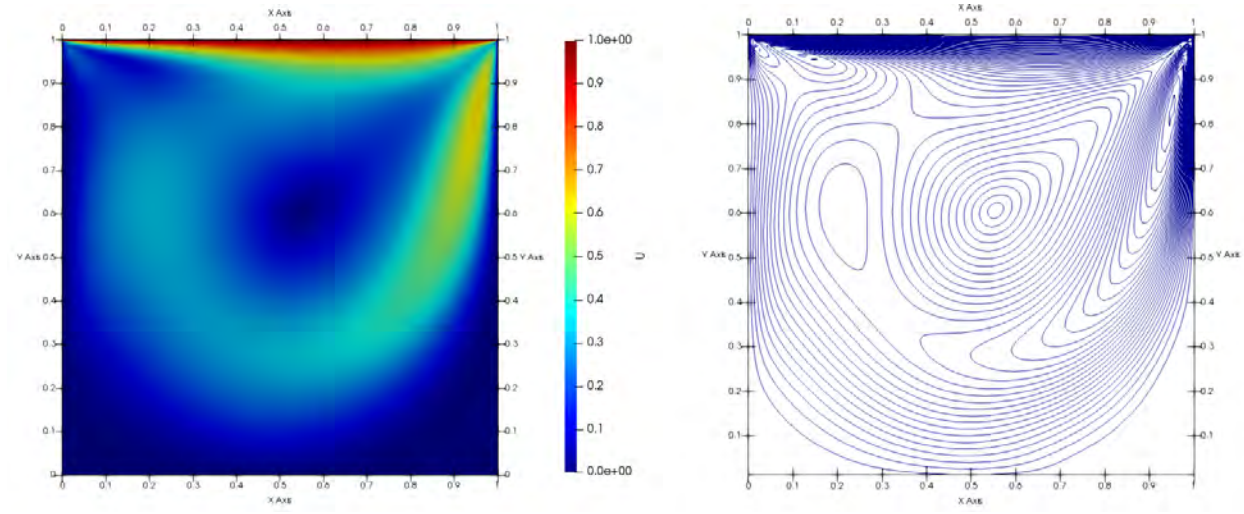

Figure 6.19: Lid-driven cavity velocity modulus and isolines of the velocity for $Re = 400$

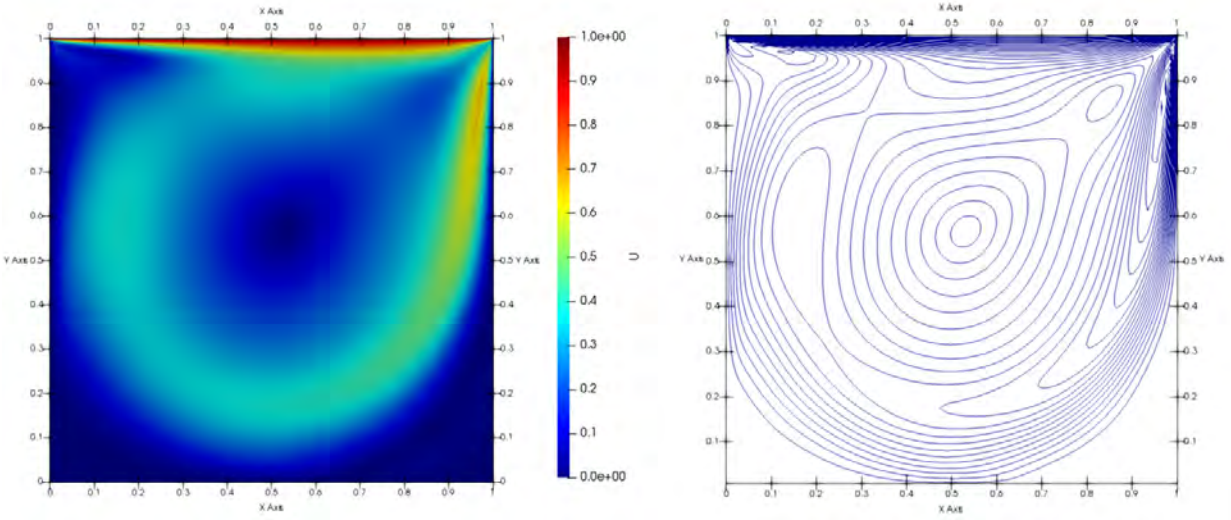

Figure 6.20: Lid-driven cavity velocity modulus and isolines of the velocity for $Re = 1000$

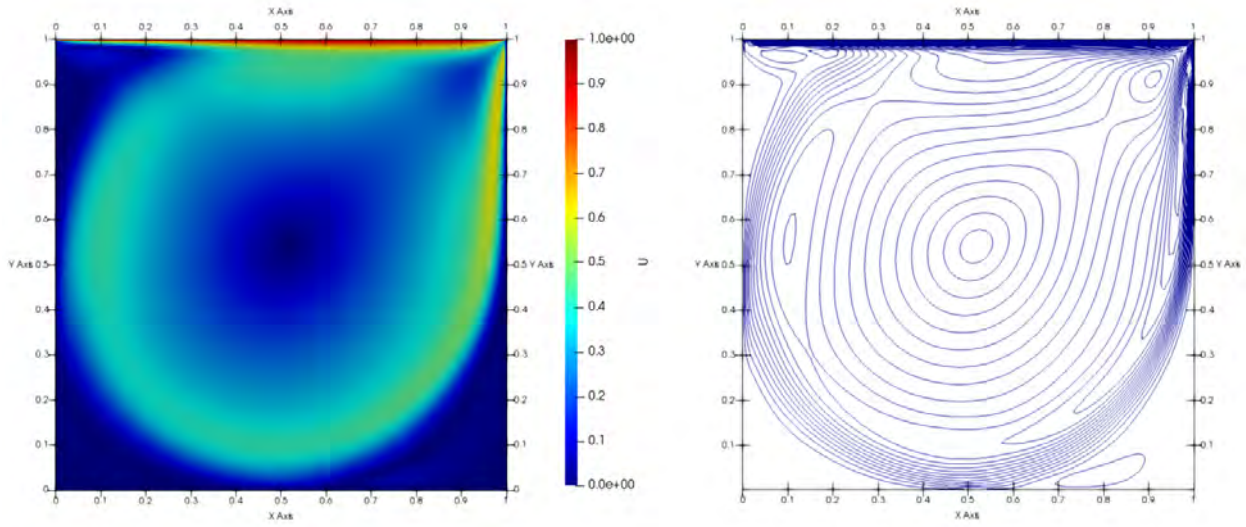

Figure 6.21: Lid-driven cavity velocity modulus and isolines of the velocity for $Re = 3200$

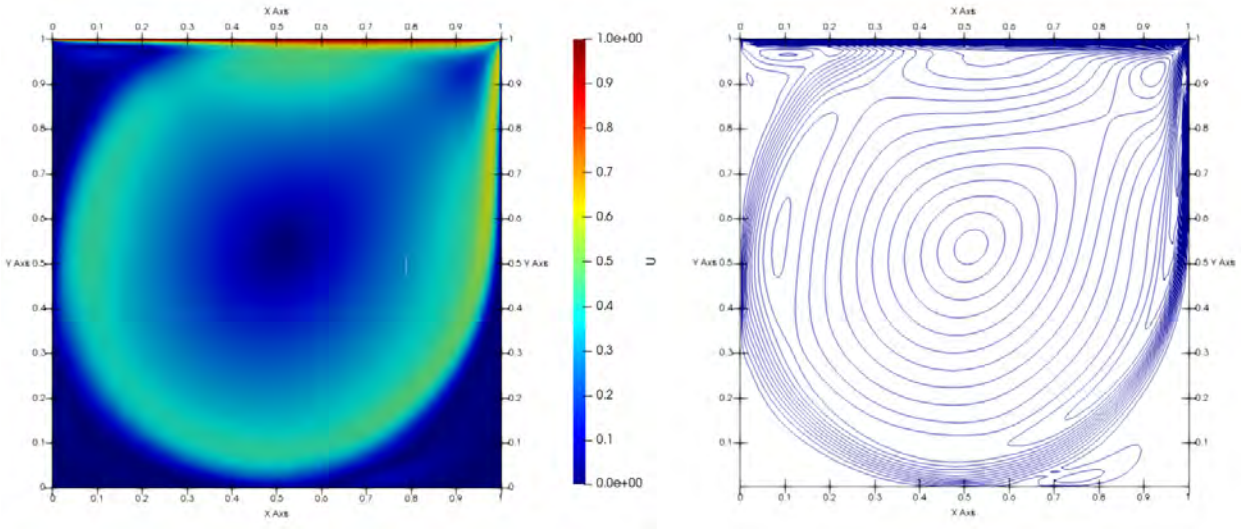

Figure 6.22: Lid-driven cavity velocity modulus and isolines of the velocity for $Re = 5000$

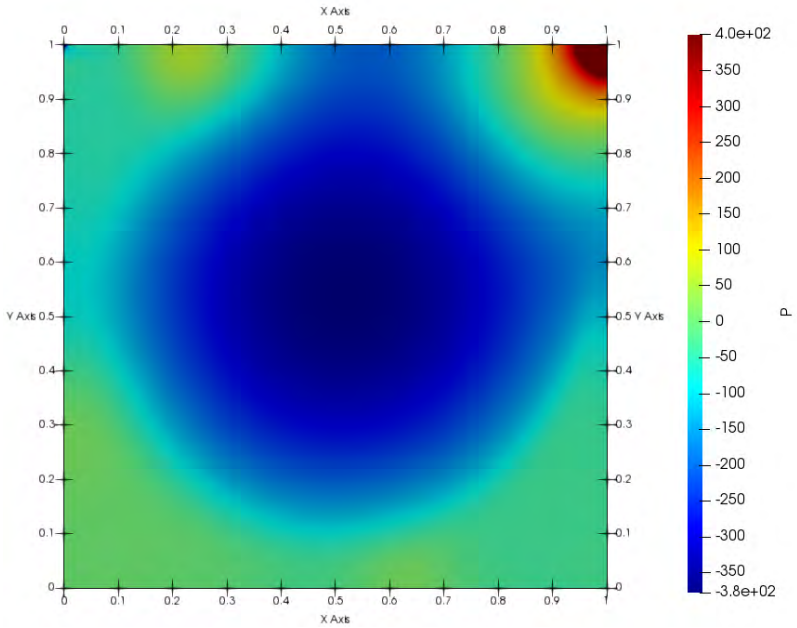

Figure 6.23: Pressure distribution at $Re = 3200$

As it can be easily depicted in the figures above, there are important velocity gradients on the top moving lid that induce the rotation of the fluid inside the cavity. A big vortex characterised by a low pressure core is created in the middle of the cavity that moves slightly towards the centre and increases in size as the Reynolds number increase. Also, another small vortex is formed in the top left corner of the cavity. Moreover, on the top right corner of the cavity a stagnation point for the x-component of the velocity leads to an important pressure build-up in this region, as it is shown in the pressure plots.

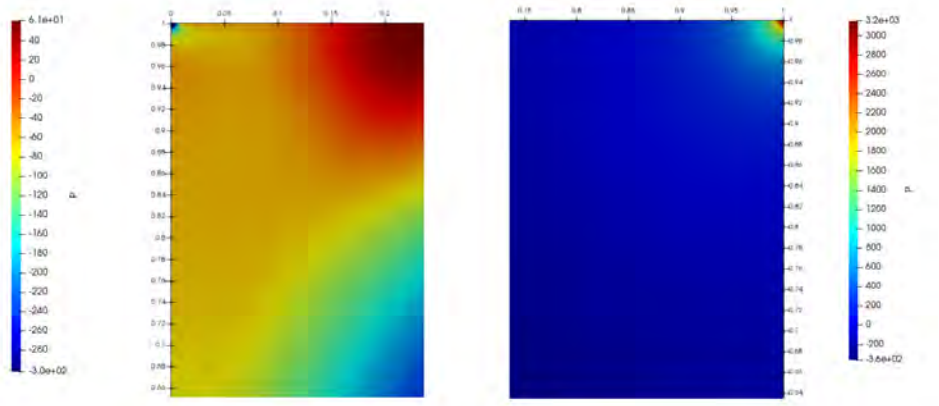

Figure 6.24: Small vortex generated on the top left corner (left) and pressure build-up on the top right corner (right)

6.9 Flow between flat plates: Poiseuille Flow

The following benchmark problem to study is the flow between flat plates driven by a pressure difference (Poiseuille flow) [18]. In this problem, the pressure gradient between the outlet and inlet of the channel drives the flow, while the viscous forces balance the pressure forces, making the fluid flow at constant velocity. However, due to these viscous forces, there is a pressure loss through the channel.

This problem is commonly used to verify CFD codes as an analytical solution of the problem exists. Considering two flat plates separated by a distance H with the reference frame placed in the middle of the channel, with the x direction on its symmetry axis:

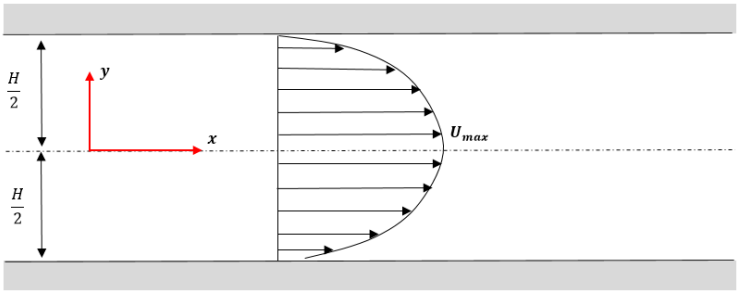

Figure 6.25: Poiseuille flow between flat plates

Considering the conservation of momentum in the x direction for 2D flow, steady state conditions and constant density:

$$\rho\left[u\frac{\partial u}{\partial x}+v\frac{\partial u}{\partial y}\right]=-\frac{\partial P}{\partial x}+\mu\left(\frac{\partial^2 u}{\partial x^2}+\frac{\partial^2 u}{\partial y^2}\right) \tag{6.9.1}$$

And the conservation of mass:

$$\frac{\partial u}{\partial x}+\frac{\partial v}{\partial y}=0 \tag{6.9.2}$$

For fully developed flow:

$$\frac{\partial u}{\partial x}=0\rightarrow\frac{\partial v}{\partial y}=0 \tag{6.9.3}$$

Which leads to:

$$\frac{\partial P}{\partial x}=\mu\left(\frac{\partial^2 u}{\partial y^2}\right) \tag{6.9.4}$$

Applying the necessary boundary conditions ($U|_{y=-H/2}=0,\ U|_{y=H/2}=0$)

$$u(y)=\frac{1}{2\mu}\frac{\partial P}{\partial x}\left[y^2-\left(\frac{H}{2}\right)^2\right] \tag{6.9.5}$$

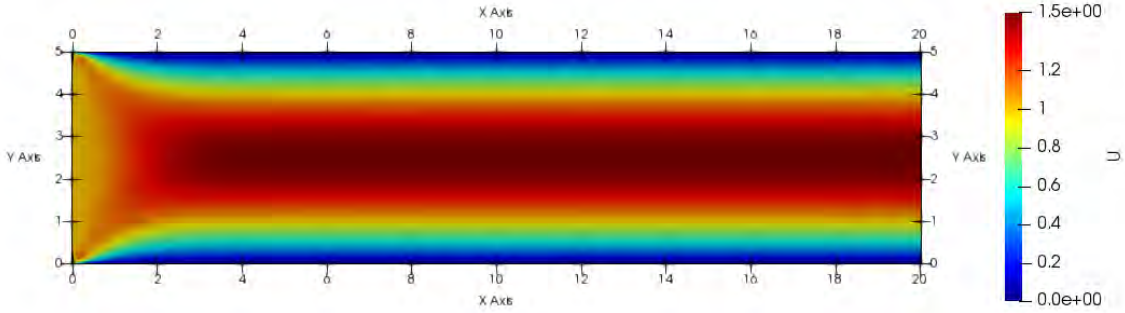

Figure 6.26: Velocity across the channel

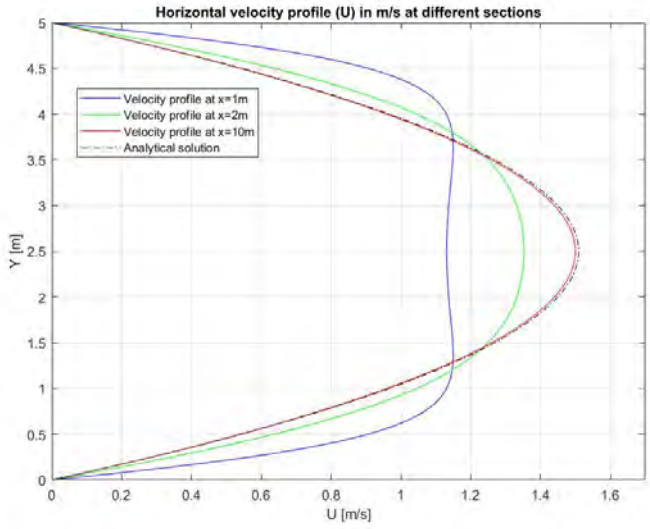

Figure 6.27: Velocity profile at different sections of the channel

The figures above show that as the flow enters inside the channel, two boundary layers are formed and start to grow up in size. As a result, the velocity increases at the centre of the section in order to keep the flow rate constant. At a certain distance from the entrance section (about $x = 3,5m$) the flow becomes fully developed and the parabolic velocity profile does not change.

The analytical solution shown in figure 6.27 was calculated using the pressure drop shown in figure 6.28. It is seen that pressure varies until the point were the flow becomes fully developed. From this point, pressure decreases linearly across the pipe until matching the external pressure at the outlet (which was set at 10 Pa).

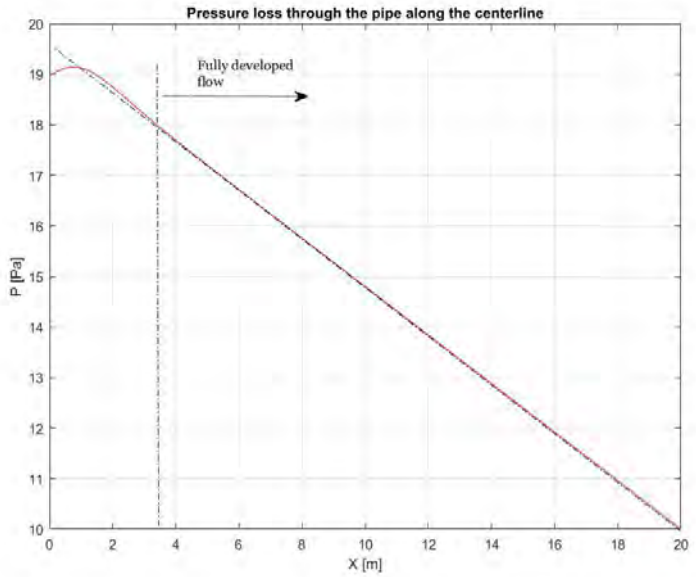

Figure 6.28: Pressure loss across the channel

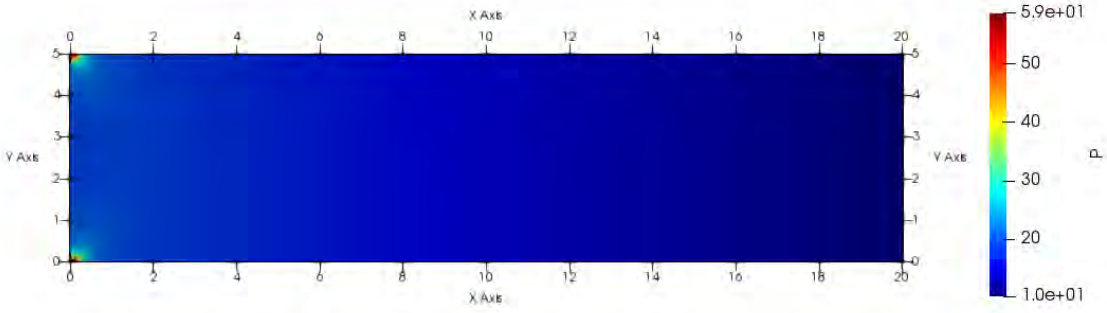

Figure 6.29: Pressure distribution across the channel

Due to the important increase in viscous forces at the inlet of the section, in contact with the plates, two pressure build up zones appear.The pressure distribution at the inlet of the section is plotted in the figure below:

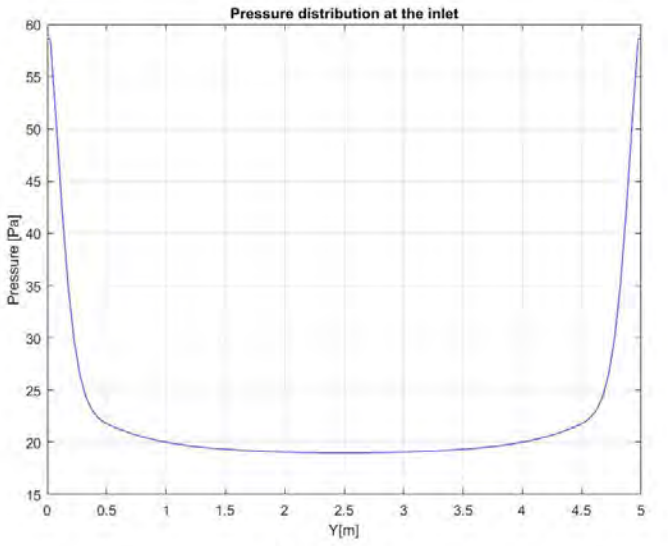

Figure 6.30: Pressure distribution at the inlet of the channel

6.10 Laminar flow around a square cylinder

The following benchmark problem to deal with is the flow around a square cylinder. This is also a common problem to study, as there are several benchmark solutions that can be found.

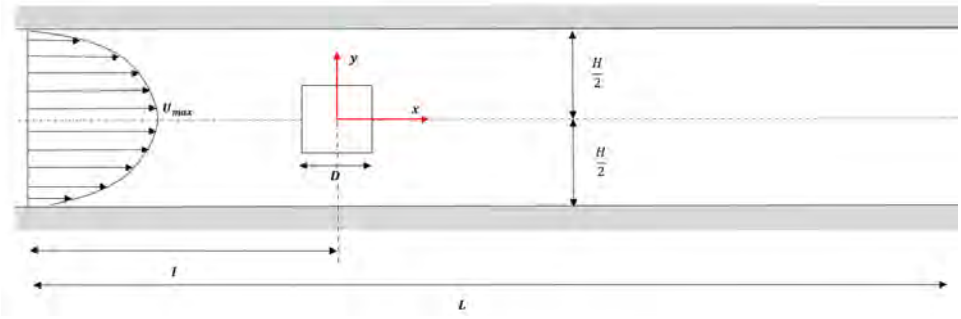

Figure 6.31: Flow around a square cylinder: geometry of the problem

A square cylinder is confined between two flat plates. The details of the geometry used are found in the following table:

D[m]	L [m]	l [m]	H [m]
1,0	30,0	10,0	8,0

Table 6.3: Geometry details of the problem: flow around a square cylinder

The ratio D/H is known as the blockage ratio. In order to capture correctly all the flow patterns around the square cylinder, the mesh was divided in three separated zones in order to get a more dense region around the cylinder and downstream.

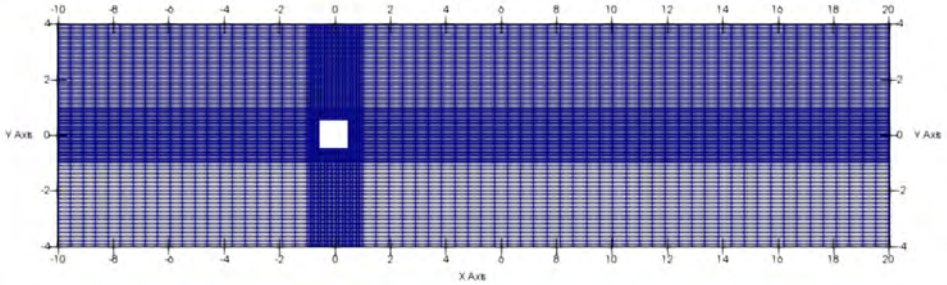

Figure 6.32: Mesh used for the square cylinder problem

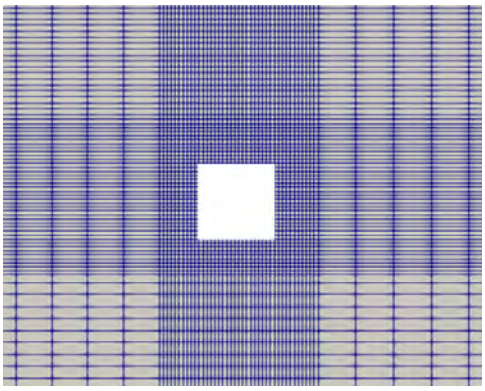

Figure 6.33: Close-up of the mesh around the square cylinder

To simulate fully developed laminar flow inside the channel, upstream of the cylinder, a parabolic velocity profile is used at the inlet, with a prescribed maximum velocity value. The pressure at the inlet can be computed

with different techniques: extrapolating with downstream pressure values or using a zero gradient approach. In this thesis both approaches were considered and, giving that results were nearly identical but computation time was lower using the second approach, a zero pressure gradient was used as a boundary condition at the inlet. At the outlet, a reference pressure was set (0 Pa), while a null gradient of the velocity was used. Finally, on the top and bottom walls, as boundary layers are formed, both components of the velocity are null and a null pressure gradient normal to the surface exists.

	U	**V**	**Pressure**
Inlet	$\frac{-4}{H^2}y^2 + 1$	0	$\frac{\partial P}{\partial n} = 0$
Outlet	$\frac{\partial U}{\partial n} = 0$	$\frac{\partial V}{\partial n} = 0$	0
Top	0	0	$\frac{\partial P}{\partial n} = 0$
Bottom	0	0	$\frac{\partial P}{\partial n} = 0$

Table 6.4: Boundary conditions

Table 6.4 summarizes the boundary conditions already stated, where U and V refer to the x and y components of the velocity (in m/s).

The same code used for the lid-driven cavity problem and for the flow between flat plates was used with the new boundary conditions. The results obtained are compared with results from [3], where the Finite Volume Method (FVM) and Lattice-Boltzmann automata (LBA) were used to compare results.

First of all, streamlines are shown in order to obtain a qualitative understanding of the physics of the problem. For low Reynolds numbers, viscous forces dominate over inertial forces. The flow passes over the cylinder and a steady state is reached without separation behind the cylinder. However, as the Reynolds number increases, viscous forces decrease in strength and flow separation at the trailing edge starts to occur. A recirculation zone is generated behind the cylinder with two symmetrical vortices placed at each side of the x axis. The length of the recirculation zone and thus, the size

of the vortices, increase as the Reynolds number increases. For Reynolds higher than $Re = 60$, approximately, the separated boundary layers on the top and bottom parts of the cylinder start to interact between them and the von Kárman vortex street is formed.

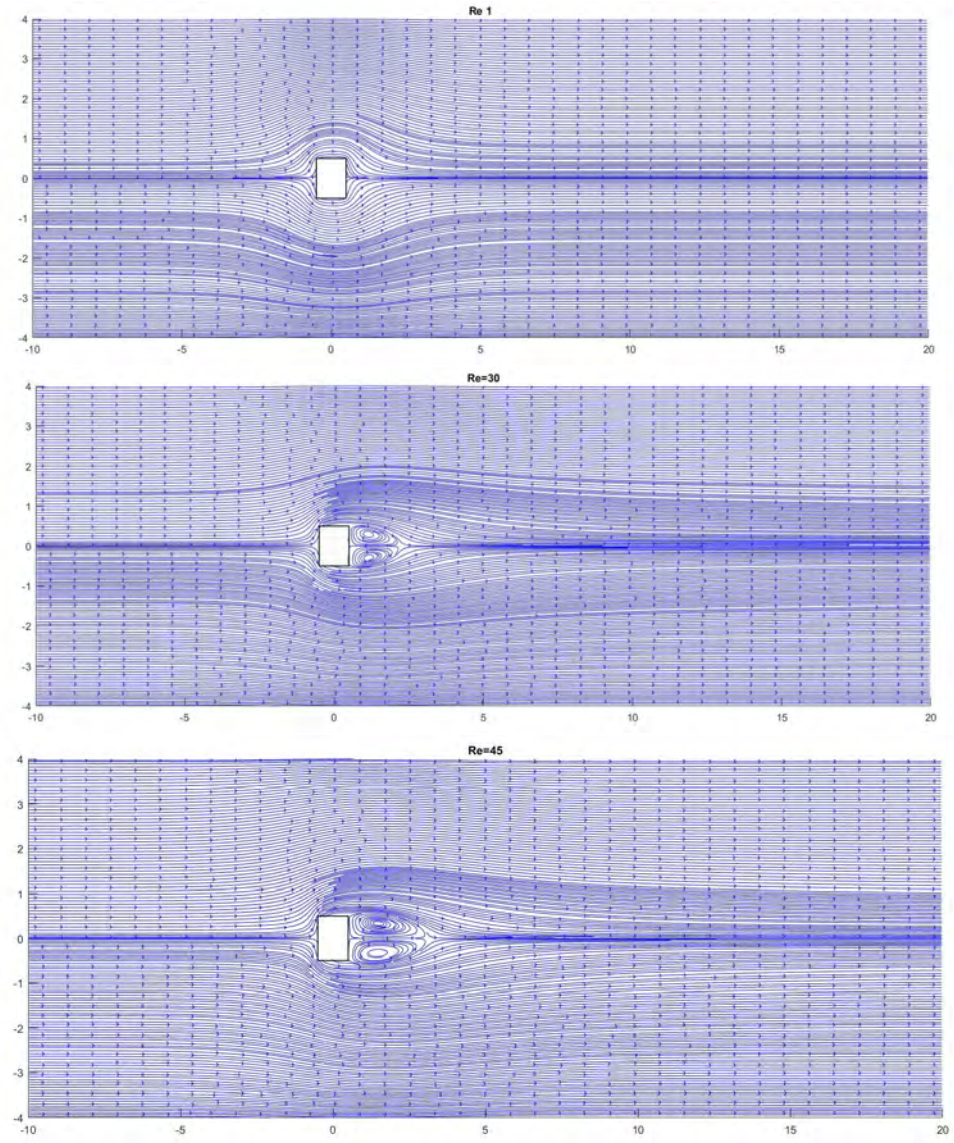

Figure 6.34: Streamlines around the square cylinder for $Re = 1,\ 30,$ and 45

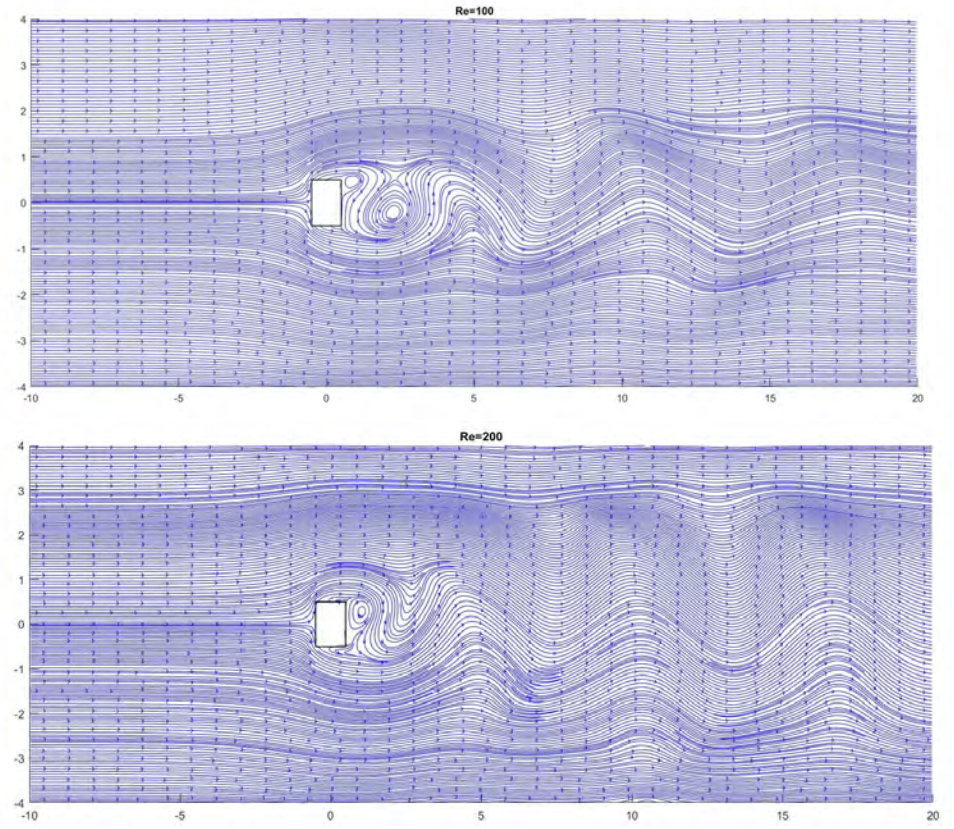

Figure 6.35: Streamlines around the square cylinder for $Re = 100$, and 200

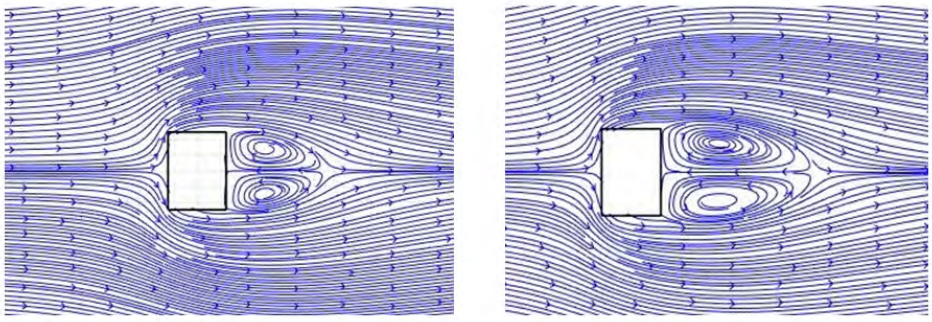

Figure 6.36: Close-up of the streamlines for $Re = 30$ (left) and $Re = 45$ (right)

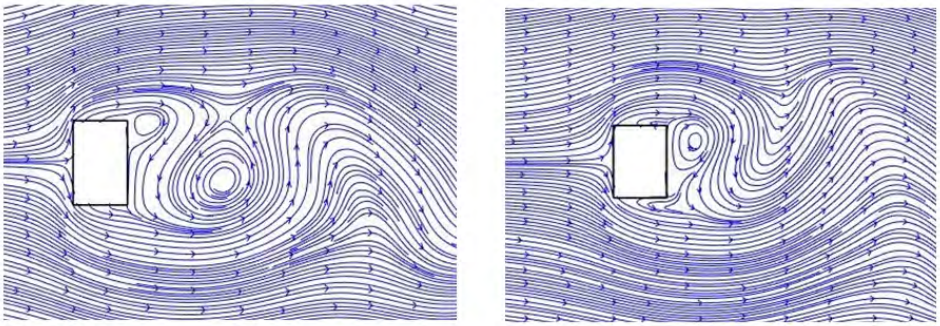

Figure 6.37: Close-up of the streamlines for $Re = 100$ (left) and $Re = 200$ (right)

The recirculation length (L_r) can be calculated as the distance that streamwise velocity component (U) becomes negative behind the cylinder.

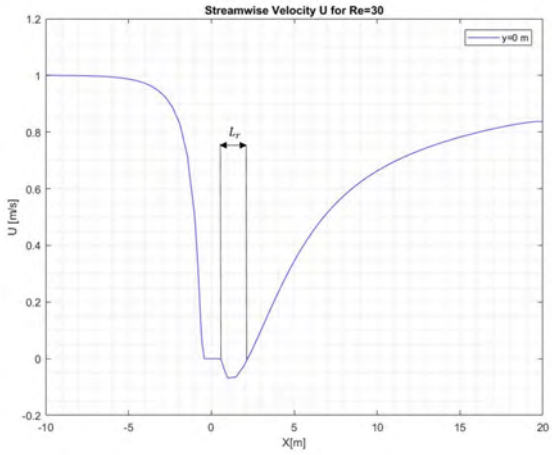

Figure 6.38: Recirculation length at $Re = 30$

The recirculation length is calculated as a function of the Reynolds number and compared with the linear fit presented in [3]. It is shown in figure 6.39 that results are pretty similar for lower Reynolds numbers but start to exhibit a small error of the order of a 5% from Re=30. This is not a really large error and could be decreased with a finer mesh. Nevertheless, it is clear that the size of the recirculation zone increases linearly as the Reynolds number increases.

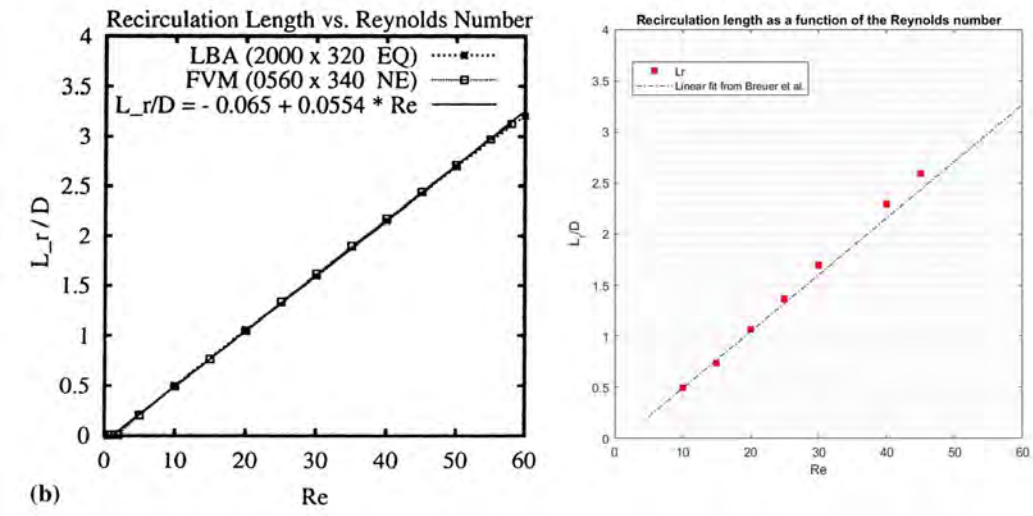

Figure 6.39: Recirculation length as a function of the Reynolds number and comparison with results from [3]

Next, the streamwise velocity U and cross-stream velocity V are graphed at different sections for different Reynolds numbers and compared with results presented in [3] for $Re = 100$.

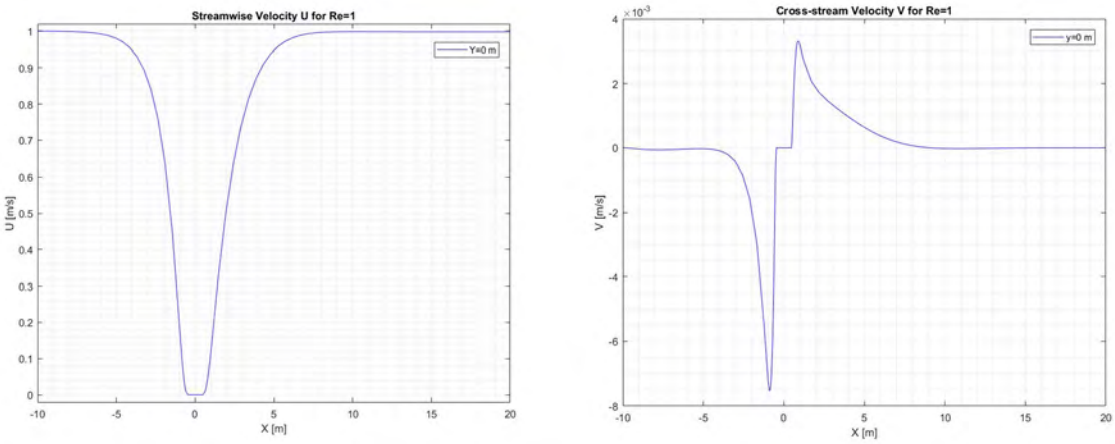

Figure 6.40: Streamwise (U) and cross-stream (V) velocities along the centerline (y=0) for $Re = 1$

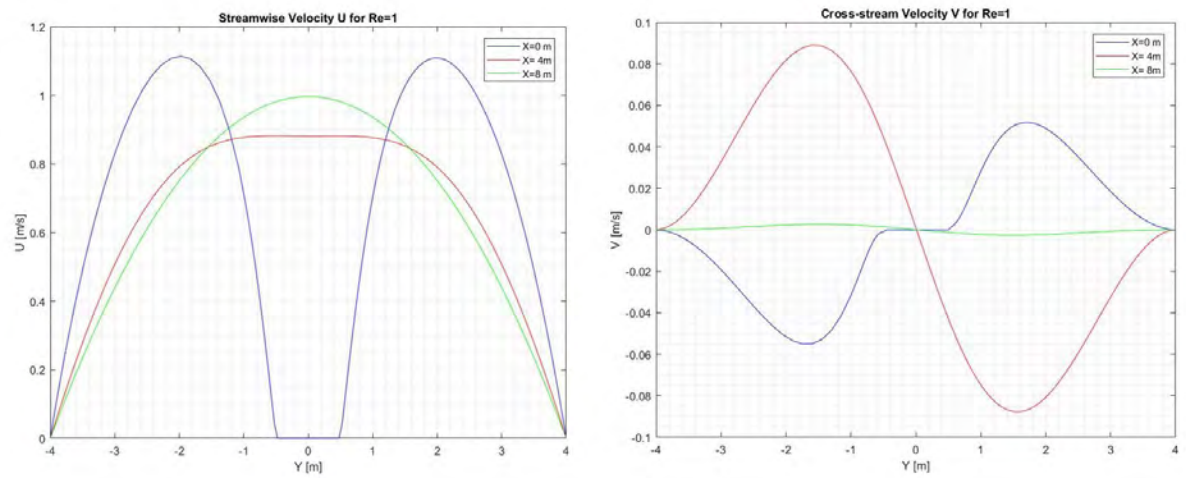

Figure 6.41: Streamwise (U) and cross-stream (V) velocities at different positions (centre of the cylinder ($x = 0$), near-wake ($x = 4$) and far-wake ($x = 8$) for $Re = 1$

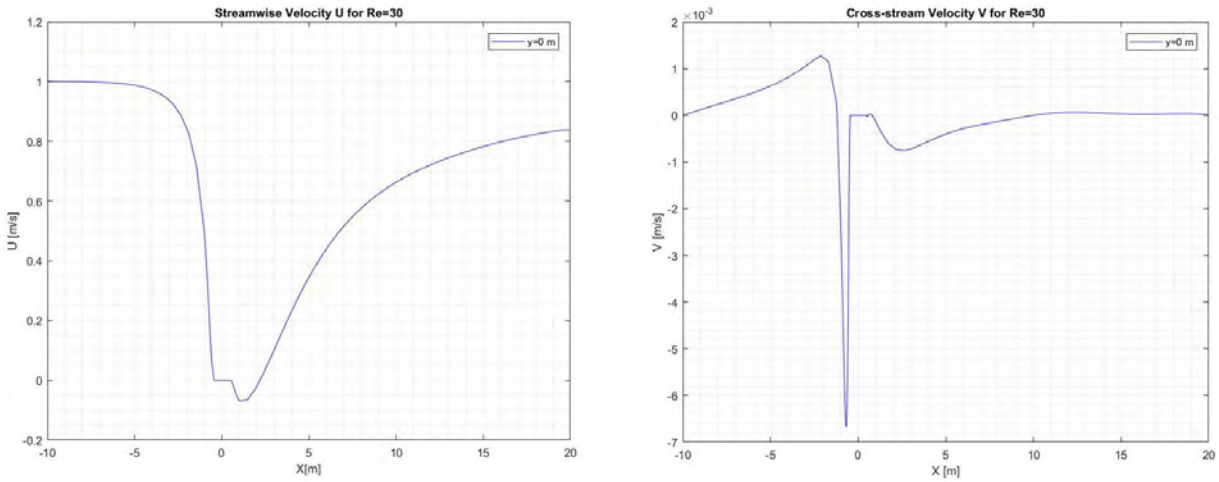

Figure 6.42: Streamwise (U) and cross-stream (V) velocities along the centerline (y=0) for $Re = 30$

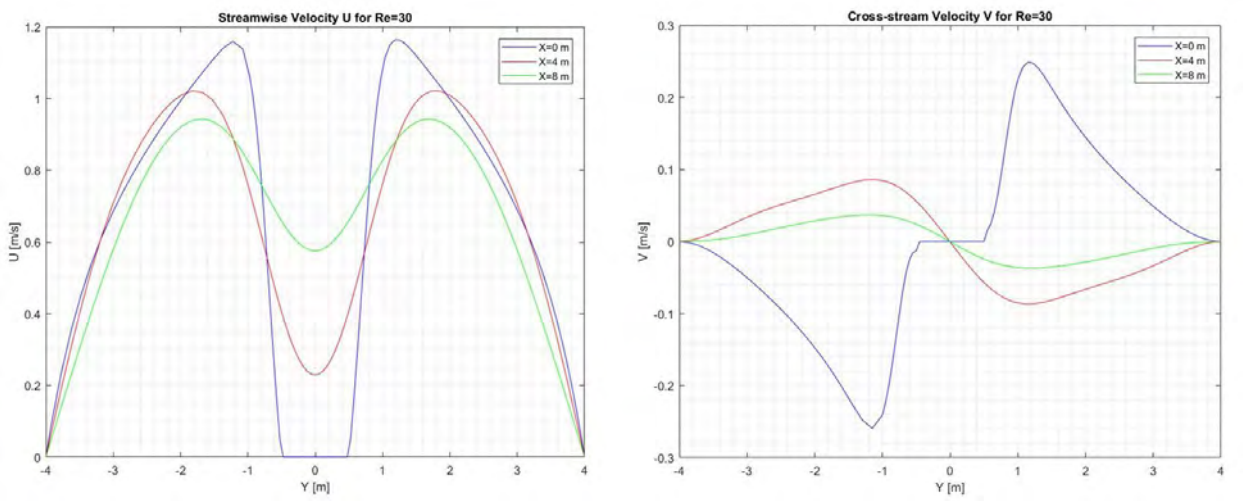

Figure 6.43: Streamwise (U) and cross-stream (V) velocities at different positions (centre of the cylinder ($x = 0$), near-wake ($x = 4$) and far-wake ($x = 8$) for $Re = 30$

As it can be depicted in the figures above, for ($Re = 1$), due to the short wake, the cross-stream velocity at $x = 8m$ is nearly 0, which means that the flow has nearly realigned with the x axis. With $Re = 30$ the oscillations in vertical velocity component are larger and persist further away due to the bigger recirculation zone.

The same happens with the horizontal velocity component. It can be seen that for $Re = 1$ at $x = 8m$ the flow is barely affected by the vortices at the trailing edge of the cylinder. However, at $Re = 30$ the flow is still affected.

At $Re = 100$, as the flow becomes unsteady, in order to compare the results with the ones presented in [3], the same moment to evaluate both velocity components is chosen. The simulation is stopped when the cross-stream velocity V at an axial position of $x = 10m$ behind the cylinder changes its sign from positive to negative.

The comparison is shown in the plots below:

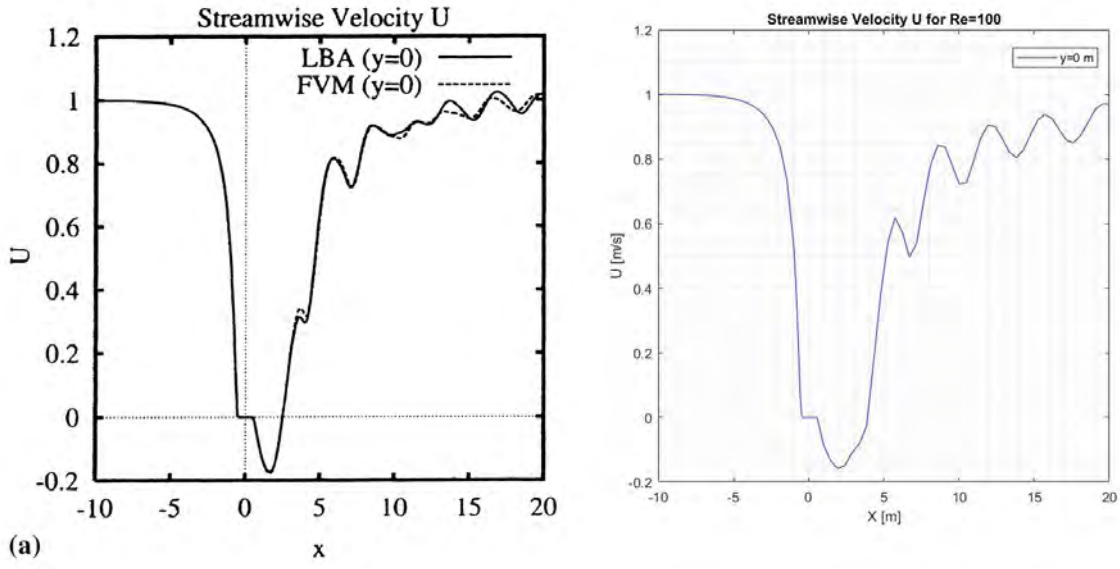

Figure 6.44: Streamwise (U) velocity along the centerline ($y = 0$) for $Re = 100$ and comparison with results from [3]

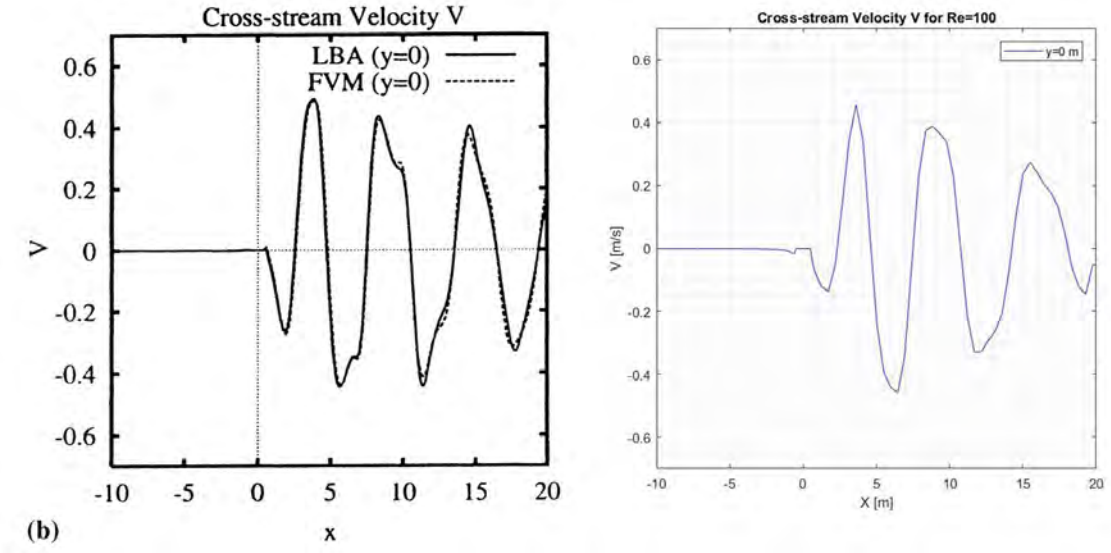

Figure 6.45: Cross-stream (V) velocity at along the centerline ($y = 0$) for $Re = 100$ and comparison with results from [3]

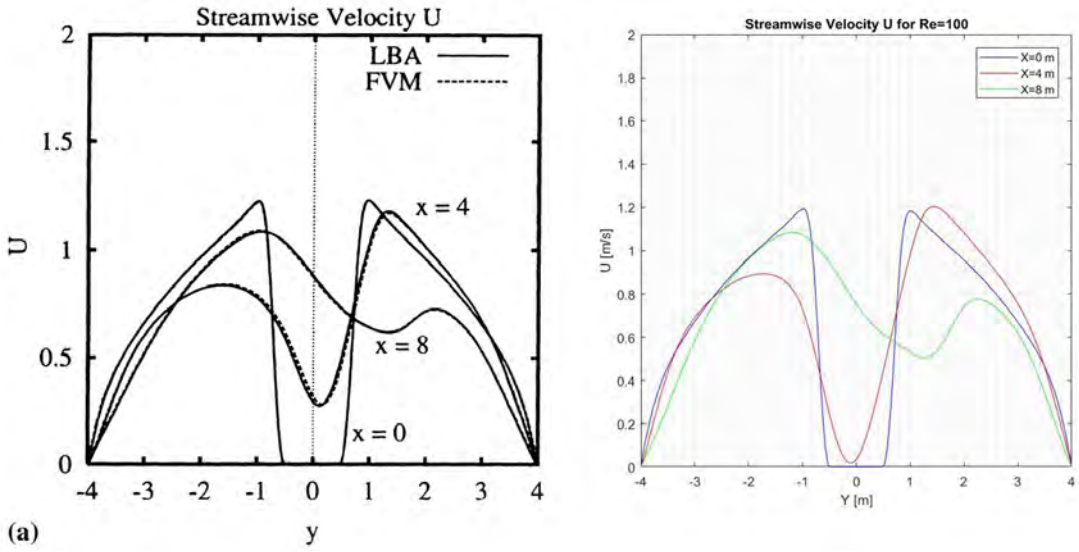

Figure 6.46: Streamwise (U) velocity at different positions (centre of the cylinder ($x = 0$), near-wake ($x = 4$) and far-wake ($x = 8$) for $Re = 100$ and comparison with results from [3]

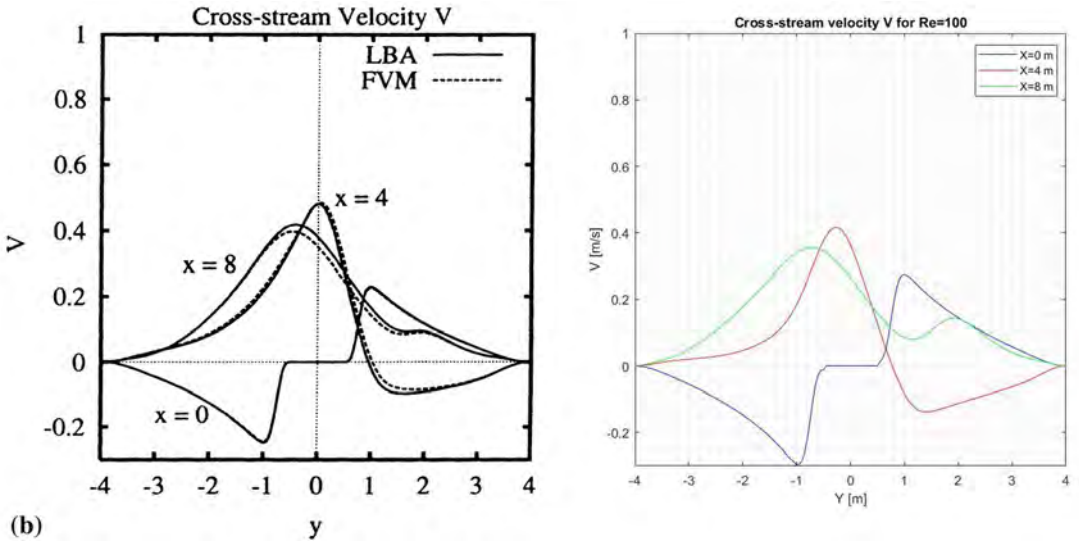

Figure 6.47: Cross-streamwise (V) velocity at different positions (centre of the cylinder ($x = 0$), near-wake ($x = 4$) and far-wake ($x = 8$) for $Re = 100$ and comparison with results from [3]

Once again, an extremely precise comparison of the results can not be made. Nevertheless, some general information can be obtained. Starting with the results of the streamwise velocity component along the horizontal centerline, it can be depicted that there is a large recirculation zone behind the cylinder, followed by an increase in horizontal velocity and finally led by important oscillations in the U velocity component due to the vortex street generated. For the vertical velocity component along the centerline, it can be depicted that it changes its sign from positive to negative due to the wake created. All the results presented are pretty similar to the ones from [3]. However, it is clear that there is a lack of resolution at the zones where important oscillations in velocity appear and thus, a more refined mesh would lead to better results.

On the other hand, while at $Re = 1$ and $Re = 30$ the streamwise (U) velocity tends to a parabolic profile as the distance from the trailing edge of the cylinder increases, for $Re = 100$ the big unsteady wake behind the cylinder persists a lot further and thus, the velocity profiles shown in figures 6.46 and 6.47 change shape depending on the section. It is important to notice that those are only the velocity profiles of an unsteady wake at a concrete time-step of the simulation, which means that they change as the wake develops.

Next, the different colormaps of the modulus of the velocity are shown:

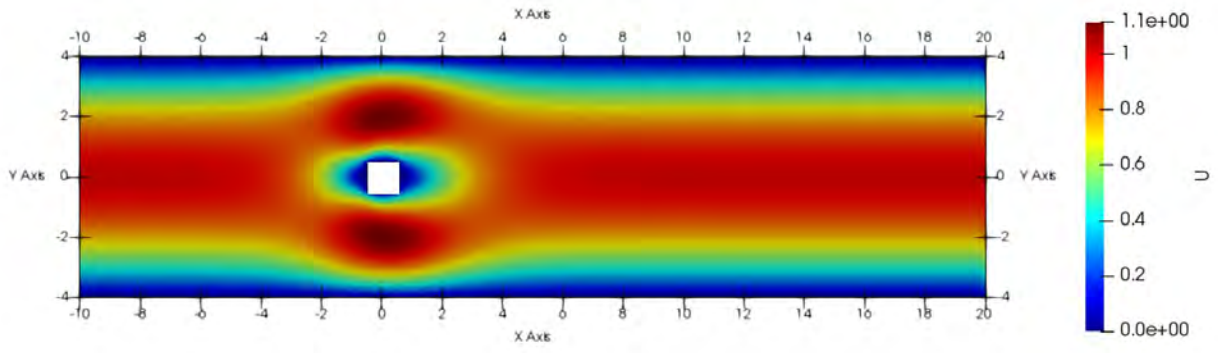

Figure 6.48: Velocity modulus at $Re = 1$

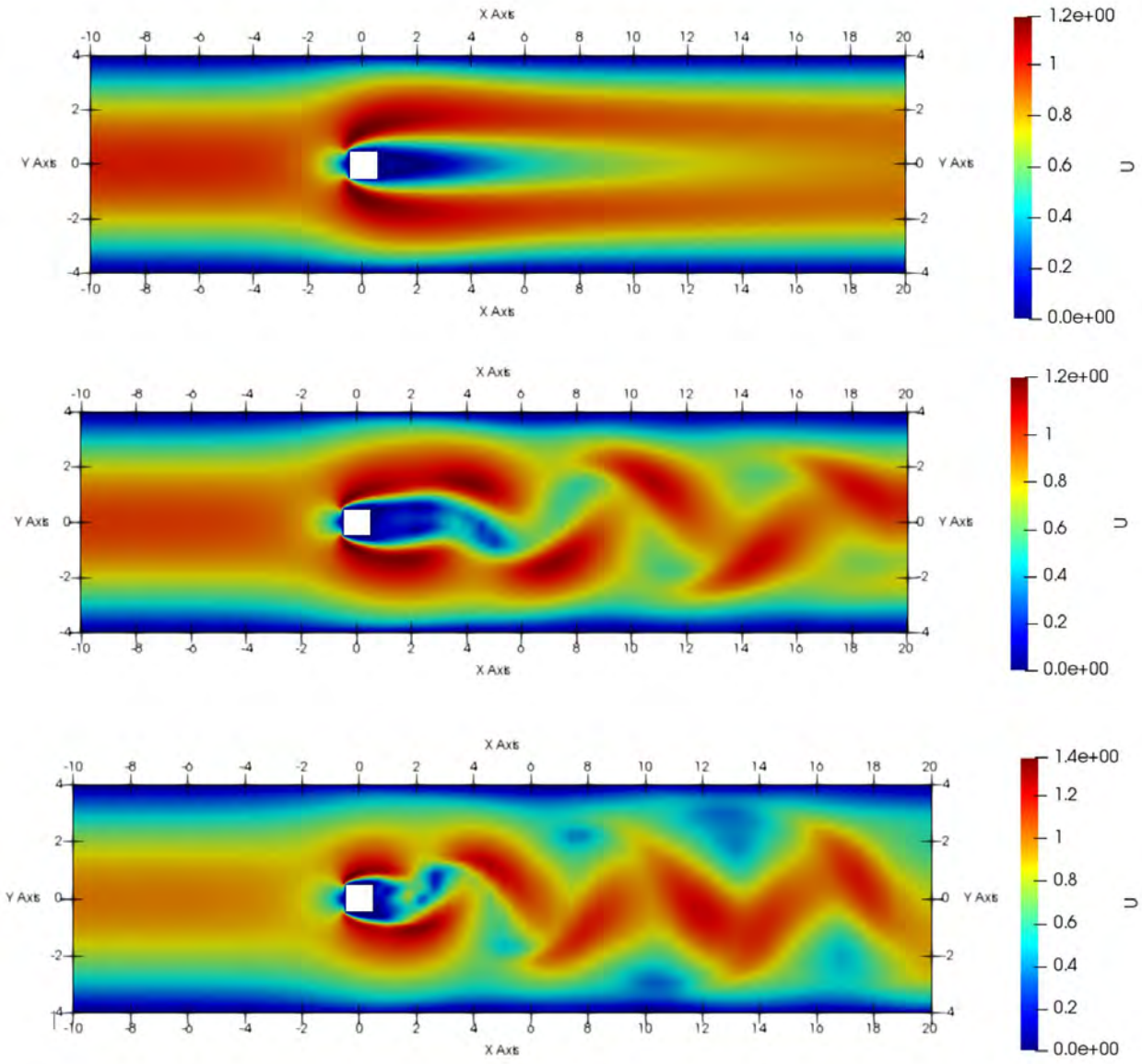

Figure 6.49: Velocity modulus at $Re = 30$, $Re = 100$ and $Re = 200$

The figures above show the already commented increase in recirculation length at the trailing edge. Moreover, it is also seen that at $Re = 100$ a vortex street has already formed and the frequency of the vortex shedding has increased at $Re = 200$.

In order to calculate drag and lift forces, the contribution of the pressure and viscous forces needs to be considered. Both forces can be calculated as follows:

$$d = \mu \left(\int_n \frac{\partial u}{\partial y} dx - \int_s \frac{\partial u}{\partial y} dx \right) + \int_w P_w dy - \int_e P e dy \tag{6.10.1}$$

$$l = \mu \left(\int_e \frac{\partial v}{\partial x} dy - \int_w \frac{\partial v}{\partial x} dy \right) + \int_s P_s dx - \int_n P n dx \tag{6.10.2}$$

As it has already been mentioned, for $Re \leqslant 60$ (approximately) a steady solution is achieved and thus, a steady value of the Cd can be obtained. The drag coefficient has been obtained using the maximum inlet velocity and the square cylinder face length. The results are plotted in the following graph and compared with results from [3].

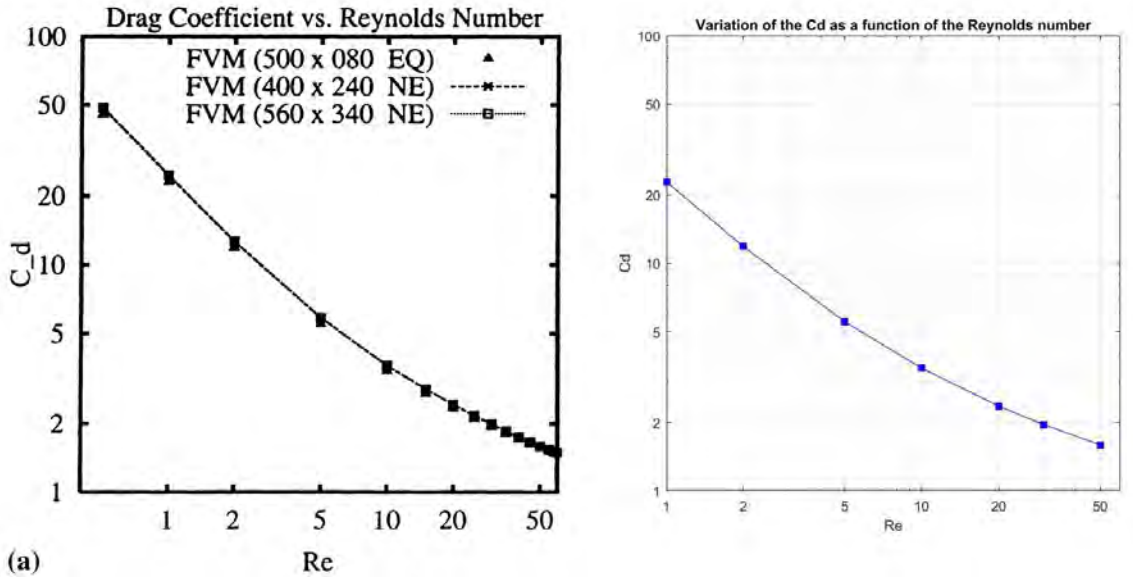

Figure 6.50: Cd as a function of the Reynolds number in steady conditions and comparison with results from [3]

It can be seen that results are pretty similar in both studies. As the Reynolds number increases, the drag coefficient decreases, the viscous forces

decrease in strength and the main drag component are the pressure forces.

For Reynolds numbers higher than 60, a steady value of the drag coefficient can not be obtained and thus, a time-averaged value needs to be computed with the following plots.

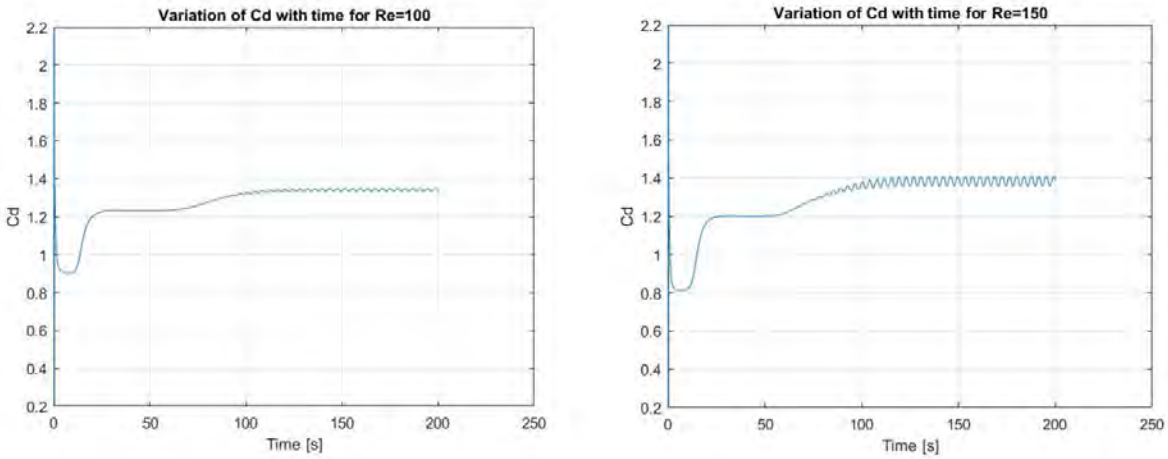

Figure 6.51: Variation of Cd with time for $Re = 100$ (left) and $Re = 150$ (right)

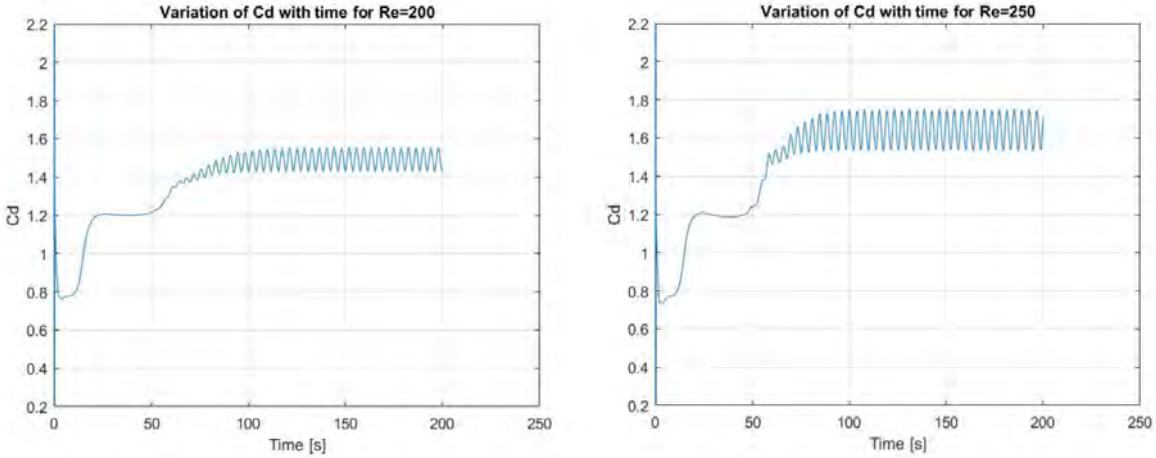

Figure 6.52: Variation of Cd with time for $Re = 200$ (left) and $Re = 250$ (right)

As it is shown in figure 6.53, for time-averaged drag coefficients lower than 100, the results are pretty similar to the ones extracted from [3]. However, for Reynolds numbers larger than 100, the error is considerable. The cause of this might be due to the use of too coarse grids, as in this figure it can be depicted that the results with a 140x140 mesh are considerably better than the ones with a 100x100 mesh.

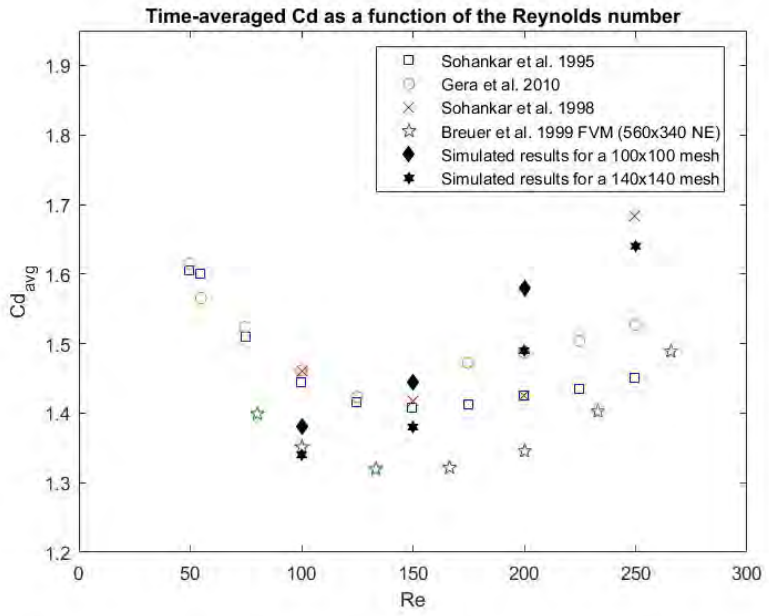

Figure 6.53: Time-averaged Cd as a function of the Reynolds number

Another possible explanation could be the transition from laminar flow to turbulent flow. The onset of 3D structures in the wake of a square cylinder is not clear in the literature. However, Franke (1991) estimates that the upper limit to consider laminar flow is around $Re = 300$, which is a close value to the ones studied in this thesis [3].

Figure 6.53 also shows results of other studies with different conditions. Sohankar et al. [19] studied the flow around a square cylinder at 5% blockage. However, the upper and lower boundaries were treated as friction-free walls. On the other hand, Gera et al. [20] simulated similar conditions with 5,5% blockage, while the upper and lower boundary conditions for the velocity were considered to be free fow conditions. These results can not be directly compared with the ones obtained in this thesis. However, it can be

depicted that the behaviour of the time-averaged drag coefficient is similar in all the studies, presenting a minimum value around $Re = 150$.

Finally, the Strouhal number is computed. The Strouhal number is a non-dimensional number to describe the mechanism of oscillating flow. It can be calculated as $S_t = \frac{fL}{U}$, where f is the frequency of the vortex shedding, L is a characteristic length of the problem (in this case the cylinder's face length) and U a characteristic velocity (for this particular problem it is the maximum velocity at the inlet). The values are computed as a function of the Reynolds number, making use of the variation of the lift coefficient with respect to time to get the vortex shedding frequency, and compared with the results of other studies.

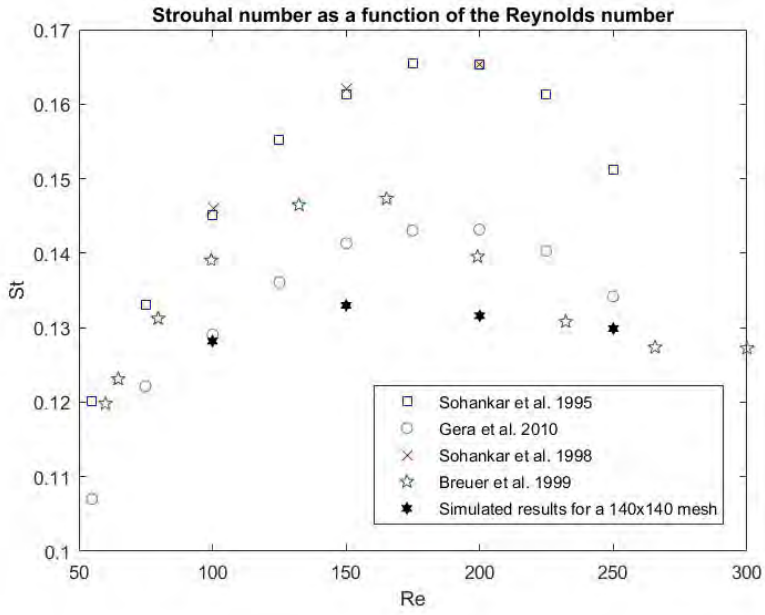

Figure 6.54: Variation of the Strouhal number with the Reynolds number

Once again, the order of magnitude of the results seems to be correct. However, there are important differences with the results from [3]. Nevertheless, the same tendency as the other studies is follwed: the Strouhal number increases until $Re = 160$ (approximately) and then starts decreasing from this point. The values of Sohankar et al. [19] and Gera et al. [20] are considerably different, even though both studies were conducted with

similar blockage ratios. The Strouhal numbers calculated by Sohankar et al. are higher than the ones from Breuer et al., even though is is well known that an increase in blockage ratio leads to an increase in the vortex shedding frequency (i.e. increase in the Strouhal number) [3].

6.11 Conclusions

In general, good agreement has been observed between the obtained results and the benchmark results. For the lid-driven cavity, SMART scheme proved to work fine for all the Reynolds numbers tested, while with UDS scheme important errors appear from Reynolds numbers higher than 100. Computation time is considerably higher with SMART convective scheme, specially as the Reynolds number increases. For the Poiseuille flow results, excellent agreement has been observed with the theoretical results. Finally, for the laminar flow around a square cylinder, really good agreement is seen with the results of Breuer et al. for Reynolds numbers lower than 100 but discrepancies appear for higher Reynolds. Nevertheless, the trend followed by the results is similar: a recirculation zone appears at the trailing edge, whose length increases linearly with the Reynolds number, and vortex shedding appears at around $Re = 60$. The values of the coefficient of drag decreases until $Re = 150$ approximately, and then increases again. Finally, the Strouhal number presents a maximum value at around $Re = 160$.

Chapter 7

Budget of the study

The following budget is an estimation of the cost that a similar project would have. However, this is just an approximation and some things need to be considered before presenting the final cost of the study:

- This is just a project of an undergraduate aerospace engineering student. This means that the salary that a engineer would be earning for the same job would probably be higher than the one of a non-graduated student. Taking this into account, the hourly price has been estimated to be about 8 €/hour. I has been considered that the salary would be higher than the minimum wage in Spain, but lower than the minimum salary of an Industrial engineer [21] [22].

- The other thing that needs to be considered is the price of the software used. All the codes have been developed with *Dev C++* and all the processed images have been done with *Paraview* which are free tools. However, the rest of the graphs were done using *Matlab*, whose educational license has a price of 8,33€/month. The project was written with *Overleaf* and the files were stored in *Google Drive*, which are free cloud-based services.

- The price of the hardware is something that needs to be considered as well. Considering that the price of the laptop was of 1900 € and it is lifetime is expected to be around 5 years, the cost of the hardware for a project of 4 months of duration is considered to be 126,7€.

- Finally, the price of the light used to power the computer, which has been used throughout the whole project, is considered as well. The

average cost of 1 $Kw \cdot h$ is $0,24$ €, considering all the taxes and fees added to the baseline price [23].

Software	Monthly cost	Total cost
Dev C++	0 €/month	0 €
Paraview	0 €/month	0 €
Overleaf	0 €/month	0 €
Google drive	0 €/month	0 €
Matlab	8,33 €/month	33,32 €
	TOTAL	33,32 €

Table 7.1: Software budget

Hardware	Monthly cost	Total cost
Computer	31,7 €/month	126,7 €
	TOTAL	126,7 €

Table 7.2: Hardware budget

Working hours	Price/hour	Total cost
600 hours	8 €/month	4800 €
	TOTAL	4800 €

Table 7.3: Salary

Cost	Price
Software cost	33,32 €
Hardware cost	126,7 €
Salary	4800 €
Electricity	169,92
TOTAL	5129,94 €

Table 7.4: Total budget

Chapter 8

Environmental impact

The environmental impact of this thesis is difficult to quantify. The main concern regarding the influence that the development of this thesis could have in the environment would be the electricity consumed to power the computer. Even with this in mind, it is still difficult to estimate the impact that the electricity has, as its origin is unknown: it could come from a renewable energy source (wind power, hydropower, solar energy...) in which case the environmental impact would be zero; or it could come from a non-renewable source of energy, (solid fuels used in thermal power stations, for example), in which case the impact would not be zero, but still minimal.

One last thing to consider could be the amount of paper used to take notes. Non-recycled paper has been used, which has an important environmental impact from its production to its distribution. Nevertheless, the impact of this is also difficult to estimate, even though it is not extremely large.

Chapter 9

Task planning

The Gantt chart presented in the following page is the initial schedule that was done before starting the project. This means that some activities were finished earlier, and some others later than what was planned.

The studies of the 2D heat conduction and potential flow around a rotating and non-rotating cylinders were completed in time. However, the study of the general convection-diffusion equation took a bit longer than expected due to the study of the order of accuracy and stability of different numerical schemes.

The verification of the lid-driven cavity code also took a bit longer than expected due to a small typing error in the code that took a few days to find.

The increase in time of the two studies already mentioned implied a short delay in the project, which meant that a deeper study of the vortex shedding phenomenon around the square cylinder was not possible. Nevertheless, the followed schedule is the one presented in the following page:

#	Traits	Title	Given Earliest Start	Given End	Predecessors
0		**SCHEDULE OF THE THESIS**	**11 Feb 2019**	**24 Jun 2019**	
1		**Previous study and search of information**	**11 Feb 2019**	**18 Feb 2019**	
2		Review of basic concepts of C++ coding	11 Feb 2019	14 Feb 2019	
3		Review of the general diffusion equation	15 Feb 2019	15 Feb 2019	
4		Search for information for the postprocess	16 Feb 2019	18 Feb 2019	
5		**Resolution of the general diffusion equation**	**19 Feb 2019**	**26 Feb 2019**	1
6		Resolution of the 2D heat conduction pr.	19 Feb 2019	24 Feb 2019	
7		Verification of the results with data from CTTC	25 Feb 2019	25 Feb 2019	6
8		Analysis of the results	25 Feb 2019	26 Feb 2019	7
9		**Potential flow**	**27 Feb 2019**	**17 Mar 2019**	5
10		Study of the potential flow	27 Feb 2019	27 Feb 2019	
11		Potential flow through channel	28 Feb 2019	1 Mar 2019	10
12		Flow around a non-rotating cylinder	2 Mar 2019	7 Mar 2019	11
13		Verification of the results	8 Mar 2019	10 Mar 2019	12
14		Resolution of the flow around a rotating cylinder	11 Mar 2019	13 Mar 2019	13
15		Verification of the results	14 Mar 2019	16 Mar 2019	14
16		Analysis of the results	17 Mar 2019	17 Mar 2019	15
17		**General Convection-diffusion equation**	**18 Mar 2019**	**15 Apr 2019**	9
18		Theoretical study of the conv.diff. equation	18 Mar 2019	21 Mar 2019	
19		Study of different convective schemes: QUICK, UDS, EDS, CDS...	18 Mar 2019	24 Mar 2019	
20		Elaboration of the script	25 Mar 2019	4 April 2019	18; 19
21		Code verification	5 April 2019	7 April 2019	20
22		Unidimensional flow analysis	7 April 2019	9 April 2019	21
23		Diagonal flow analysis	10 Apr 2019	12 Apr 2019	21
24		Smith-Hutton problem analysis	13 Apr 2019	15 Apr 2019	21
25		**Incompressible Navier-Stokes equations**	**23 Apr 2019**	**20/05/2019**	17
26		Study of the Fractional-Step method	23 Apr 2019	28 Apr 2019	
27		Theoretical study of the staggered meshes	23 Apr 2019	28 Apr 2019	
28		Study of refined mesh at the boundaries	28 Apr 2019	28 Apr 2019	
29		Elaboration of the script	29 Apr 2019	9 May 2019	26; 27; 28
30		Lid-driven cavity results verification	10/05/2019	12/05/2019	29
31		Study of the blocking-off method	13/05/2019	14/05/2019	30
32		Aerodynamic study of simple geometries	15/05/2019	20/05/2019	31
33		Writing of the thesis	11 Feb 2019	7 June 2019	1; 5; 9; 17; 25
34		Review of the final document	8 June 2019	9 June 2019	33
35		Preparation of the oral presentation	12 Jun 2019	23 Jun 2019	33; 34

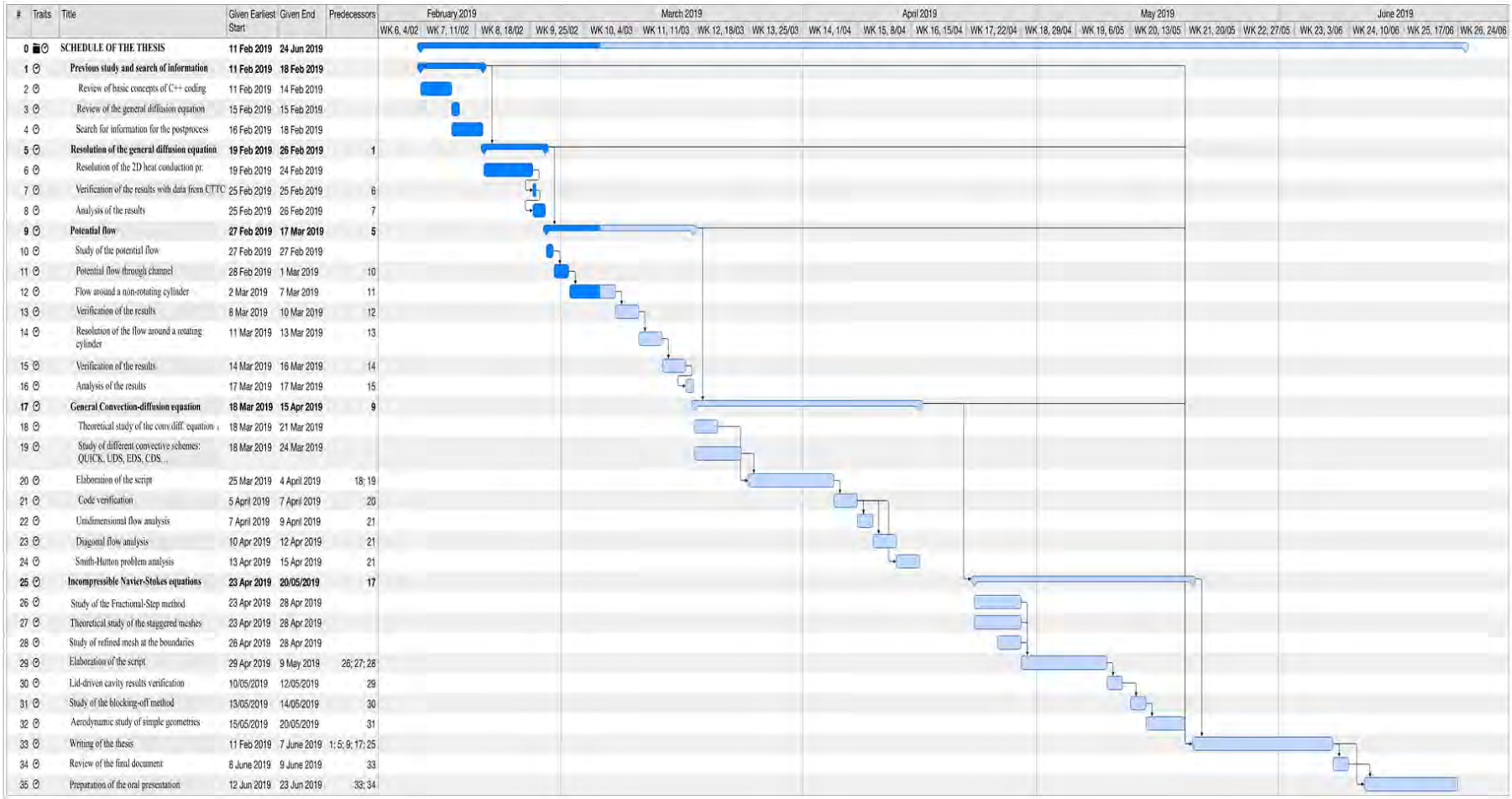

Figure 9.1: Gantt chart

Chapter 10

Conclusions and future work

The final objective of this thesis was the numerical resolution of the Navier-Stokes equations using the Fractional-Step method and the verification of the results with the Lid-driven cavity problem; before solving the particular case of the flow around a square cylinder. In general terms, the objectives established before the study have been accomplished.

The finite volume method, in conjunction with the Fractional Step method, has proved to be a really powerful technique to solve the incompressible form of the Navier-Stokes equations. It has become clear the importance of the good spatial and temporary discretization in order to get accurate results. Moreover, the importance of the order of accuracy of the discretized equations is evident, specially regarding the selection of a good scheme to treat the convective term, as it was seen with the results of the Lid-driven cavity problem, where a bad selection of the convective scheme led to important errors. The study of the order of accuracy of the overall approximation proved to be a powerful and easy way to check the good implementation of the numerical schemes and to find possible mistakes in the code, as it can be seen in the study of the general convection-diffusion equation.

Regarding the results obtained with the study of laminar flow around a square cylinder, a few conclusions can be gathered. First of all, and as stated in [3], there is a lack of accurate data in the literature for the confined laminar flow past a square cylinder. Due to this, results could only be compared with the ones from Breuer et al., and other studies were used to get a general idea of the trend of the results, but could not be used for a precise comparison owing to the different blockage ratios used. Moreover,

data of similar simulations in the literature are highly scattered, specially when the wake behind the cylinder becomes unsteady.

Nevertheless, for Reynolds values lower than 60 an excellent agreement is found between the results of this thesis and the ones presented in [3]. Between the Reynolds number range $60 \leqslant Re \leqslant 100$, important deviations are seen, and for Reynolds values larger than 100 the deviations are really important. As stated previously, this discrepancies in the results could be explained due to the need of a finer mesh, which leads to a really important increase in computation time, or due to the transition from laminar to turbulent flow.

The next steps to be done would be the improvement of the mesh used until the results obtained are independent of the cell size. If the improvement in the results is not enough, the turbulence phonemonon should be considered and studied in detail before using a suitable turbulence model, such as the Direct Numerical Simulation (DNS) or Large-Eddy Simulation (LES). Moreover, the implementation of unstructured meshes would also be important, even though this is not necessary for the simple geometry of a square cylinder. Finally, it would be really interesting to study other problems where the energy equation plays an important role in the final results, such as for problems where natural convection takes place.

Chapter 11

Bibliography

[1] CTTC - Universitat Politècnica de Catalunya, "A Two-dimensional transient conduction problem," pp. 1–3, 2014.

[2] ——, "Fractional Step Method Staggered Meshes," pp. 1–33, 2014.

[3] Z. D. Breuer, Bernsdor, "Accurate computations of the laminar flow past a square cylinder based on two different methods: Lattice-Boltzmann and finite-volume," *International Journal of Heat and Fluid Flow*, vol. 21, no. 2, pp. 186–196, 2000.

[4] CTTC - Universitat Politècnica de Catalunya, "Numerical resolution of the generic convection-diffusion equation," pp. 1–28.

[5] "Computational fluid dynamics— Wikipedia, the free encyclopedia," 2019. [Online]. Available: https://en.wikipedia.org/wiki/Computational_fluid_dynamics

[6] H. K. Versteeg and W. Malaskekera, "An Introduction to Computational Fluid Dynamics: The Finite Volume Method," p. 517, 1995.

[7] CTTC - Universitat Politècnica de Catalunya, "Computational engineering - Tackling turbulence with (super)computers."

[8] A. Jameson, "Computational Fluid Dynamics: Past, Present and Future," *Future Directions in CDF Research, National Institute for Aerospace*, p. 75, 2012.

[9] "Navier-Stokes Equations — Wikipedia, the free encyclopedia," 2019. [Online]. Available: https://en.wikipedia.org/wiki/Navier%E2%80%93Stokes_equations

[10] NASA, "Navier-Stokes Equations." [Online]. Available: https://www.grc.nasa.gov/www/k-12/airplane/nseqs.html

[11] "Gauss–seidel method — Wikipedia, the free encyclopedia," 2019. [Online]. Available: https://en.wikipedia.org/wiki/Gauss%E2%80%93Seidel_method

[12] "Tridiagonal matrix algorithm — Wikipedia, the free encyclopedia," 2019. [Online]. Available: https://en.wikipedia.org/wiki/Tridiagonal_matrix_algorithm

[13] "Properties of Numerical Methods," *Computational Engineering — Introduction to Numerical Methods*, pp. 1–19, 2006.

[14] J. Anderson, *Fundamentals of Aerodynamics*, ser. McGraw-Hill series in aeronautical and aerospace engineering. McGraw-Hill, 2011.

[15] P. H. Gaskell and A. K. C. Lau, "Curvature compensated convective transport: SMART, a new boundedness preserving scheme," vol. 8, no. February 1987, pp. 617–635, 1988.

[16] MIT, "Numerical Fluid Mechanics Spring 2015," pp. 1–24, 2015.

[17] Guilherme Caminha, "The cfl condition and how to choose your timestep size – Simscale," 2019. [Online]. Available: https://www.simscale.com/blog/2017/08/cfl-condition/

[18] "Hagen–Poiseuille equation — Wikipedia, the free encyclopedia," 2019. [Online]. Available: https://en.wikipedia.org/wiki/Hagen%E2%80%93Poiseuille_equation#Liquid_flow_through_a_pipe

[19] A. Sohankar, C. Norberg, and L. Davidson, "Numerical Simulation of Unsteady low Reynolds Number Flow around a square Two-Dimensional Cylinder," *Proc. 12 th Australian Fluid Mechanics Conference*, pp. 517–520, 1995.

[20] B. Gera, P. K. Sharma, and R. K. Singh, "CFD analysis of 2D unsteady flow around a square cylinder," *International Journal of Applied Engineering Research, Dindigul*, vol. 1, no. 3, pp. 602–610, 2010.

[21] "Tusalario.es." [Online]. Available: https://tusalario.es/salario/comparatusalario?job-id=2141010000000#/

[22] "Salario Mínimo Interprofesional," 2019. [Online]. Available: http://www.salariominimo.es/2019.html

[23] "Tarifaluzhora." [Online]. Available: https://tarifaluzhora.es/

[24] CTTC - Universitat Politècnica de Catalunya, "Verification strategies for the convection-diffusion equation," pp. 1–5, 2014.

[25] L. E. Schwer, "Is your mesh refined enough? Estimating Discretization Error using GCI," *7th LS-DYNA Anwenderforum*, vol. 1, no. 1, pp. 45–54, 2008.

[26] "Normalized variable and space formulation methodology for high-resolution schemes," *Numerical Heat Transfer, Part B: Fundamentals*, vol. 26, no. 1, pp. 79–96, 1994.

[27] CTTC - Universitat Politècnica de Catalunya, "Non viscous flow."

[28] Z. C. Y. Shams-ul-Islam, Raheela Manzoor, "Effect of Reynolds Number on Flow past a Square Cylinder in Presence of Upstream and Downstream Flat Plate at Small Gap Spacing," 2015.